

# POLITECNICO DI TORINO

Master of Science in Biomedical Engineering

Master's Thesis



“3D hydrogel printing techniques for the development of a collagen-based alveoli unit model”

Supervisors:

Prof. Gianluca Ciardelli

Dr. Chiara Tonda Turo

Candidate:

Lara Victoria Aiassa

Cotutelle:

Michela Licciardello

July 17<sup>th</sup>, 2020

*“Be the best version of yourself in everything you do.*

*What you plant today you will harvest later”*

– Life lesson from my parents –

To my family.

# Table of content

<b>1. Introduction.....</b>	<b>1</b>
1.1 The clinical problem .....	1
1.2 Overview of the Lung Tissue .....	3
1.2.1 Organization of the respiratory system.....	3
1.2.2 External respiration .....	3
1.2.3 Respiratory portion.....	3
1.2.3.1 Alveoli.....	3
1.2.3.2 Alveolar Lining Cells.....	4
1.2.3.3 Alveolar septum.....	4
1.2.3.4 Air-Blood Barrier .....	4
1.2.3.5 Capillary Endothelium.....	5
1.2.3.6 Other Cells and Structures in the Alveolar Wall .....	5
1.3 Tissue Engineering (TE) .....	6
1.4 Engineered tissue models of lung parenchyma .....	8
1.4.1 Introduction.....	8
1.4.2 Animal Model.....	8
1.4.2.1 Animal models to recapitulate human diseases .....	8
1.4.2.2 Limitations.....	9
1.4.3 Two-dimensional (2D) cell culture models .....	10
1.4.3.1 Tissue culture plastic (TCP) or glass substrates .....	10
1.4.3.2 Limitations of 2D cell culture models.....	10
1.4.4 From 2D to 3D systems .....	11
1.4.4.1 Transwell cell culture systems.....	11
1.4.4.2 Basement membrane cell culture .....	12
1.4.4.3 Sandwich cell culture .....	12
1.4.4.4 Limitations .....	12
1.4.5 Three-dimensional (3D) cell and tissue culture models .....	14
1.4.5.1 Hydrogel systems.....	14
1.4.5.2 Decellularized matrices.....	14
1.4.5.3 Precision cut human/animal lung tissue (PCLT) .....	15
1.4.5.4 Lung spheroids and organoids.....	15
1.4.5.5 Limitations.....	16
1.4.5.6 Lung-on-chip .....	16
1.4.5.7 Limitations .....	17

1.5	Three-dimensional matrix fabrication techniques: State of Art .....	19
1.5.1	First considerations: structural and materials properties.....	19
1.5.2	Fabrication techniques .....	20
1.5.2.1	Cell entrapment technique.....	20
1.5.2.2	Polymer processing techniques.....	21
1.5.2.3	Computer-assisted fabrication.....	23
1.5.2.4	Extrusion Bioprinting.....	25
1.6	Scientific Background .....	27
1.6.1	Hydrogels .....	27
1.6.1.1	Definition and properties .....	27
1.6.1.2	Cross-Linking Mechanisms of Hydrogels.....	27
1.6.2	Collagen.....	27
1.6.2.1	Definition and structure.....	27
1.6.2.2	Properties: fibrillogenesis.....	29
1.6.2.3	Collagen: Animal Sources and Biomedical Application .....	31
<b>2.</b>	<b>Aim of the work.....</b>	<b>50</b>
<b>3.</b>	<b>Materials and Methods.....</b>	<b>51</b>
3.1	Collagen solution.....	51
3.1.1	Components.....	51
3.1.2	Collagen based hydrogel generation.....	53
3.2	Gelatin slurry support bath .....	55
3.2.1	Components.....	55
3.2.2	Generation of the gelatin slurry support bath.....	57
3.3	Characterization of the collagen hydrogel: sol-gel transition.....	60
3.3.1	Tube inverting test .....	60
3.3.2	GLIM optical microscopy.....	60
3.3.3	FE-SEM.....	62
3.4	Scaffold printing.....	63
3.4.1	Rokit INVIVO .....	63
3.4.1.1	Printing parameters and initialization .....	64
3.4.2	BioX Cellink .....	69

3.4.2.1	Printing parameters and initialization .....	69
3.5	Three-dimensional model of a pulmonary acinus .....	71
3.5.1	3D bioprinting .....	74
3.5.2	Molding .....	75
<b>4.</b>	<b>Results.....</b>	<b>77</b>
4.1	Characterization of the collagen hydrogel .....	77
4.1.1	Tube inverting test .....	77
4.1.2	GLIM optical microscopy .....	78
4.1.3	FE-SEM .....	80
4.2	Scaffold printing .....	81
4.2.1	Rokit INVIVO .....	81
4.2.1.1	Freeform fabrication strategy .....	81
4.2.1.2	Deposition within a support bath .....	82
4.2.2	BioX Cellink .....	84
<b>5.</b>	<b>Conclusion.....</b>	<b>85</b>
<b>6.</b>	<b>Future work .....</b>	<b>87</b>
6.1	BioX Cellink: Collagen bioink. ....	87
6.2	Neutralization protocol: NaOH final concentration. ....	88
6.3	Alternative printing approach: the effect of riboflavin photocrosslinking.....	89
6.4	Study of the fibrillogenesis of collagen-riboflavin hydrogels: Thioflavin spectroscopic properties .....	91
6.5	Thioflavin-T: groundwork .....	92
6.5.1	Materials and methods.....	92
6.5.1	Results .....	94
	<b>Acknowledgments .....</b>	<b>95</b>
	<b>List of Abbreviations .....</b>	<b>96</b>
	<b>Bibliography.....</b>	<b>98</b>

# Abstract

Lung cancer is the leading cause of cancer death around the world. Management of lung disease often includes drug therapy and unfortunately, the development of safe and effective drugs is currently constrained by the lack of a robust preclinical models. There is a crucial need for *in vitro* human lung tissue models that would help to bridge the gap in the current knowledge of lung treatment and provide a better understanding of lung development, physiology and pathology.

Three-dimensional bioprinting is a potential method for creating biological tissues. The creation of multilayered hollow organs raises the possibility of reproducibly creating complex macro- and microscale architectures using multiple different cell types. Because hydrogels are one of the most feasible classes of ink materials for 3D printing, this work focuses on a hydrogel-based biomaterial ink, in particular a collagen-based bioink, used to develop a layered construct, in order to create an *in vitro* model of the lung. Different hydrogel-compositions and 3D printing approaches were exploited to finally identify the most promising technique. The finest results in term of printability were obtained using the freeform fabrication strategy, resulting in an easiest bioprinting setup, as well as real-time monitoring of the printing process. The protocol was optimized by obtaining a final concentration of collagen solution of 2% wt that demonstrates fullest gelation behavior. Thereby, the basis guidelines for future work are outlined.

Finally, a CAD (computer-aided design) model of a pulmonary acinus is presented with the future outlook of printing the 3D model in a scaled-up version.

**Keywords:** *in vitro* model, lung tissue, hydrogels, collagen, 3D bioprinting.

# 1. Introduction

## 1.1 The clinical problem

Lung disease remains a significant cause of morbidity and mortality in the world and can be either obstructive or restrictive in nature. Lung cancer must be considered separately because of its high incidence in both men and female individuals. Lung cancer is the leading cause of cancer death around the world. Almost as many Americans die of lung cancer every year than die of prostate, breast, and colon cancer combined [1]. Management of lung disease often includes drug therapy, oxygen therapy, radio therapy, surgery, and lung transplantation. Unfortunately, due to lack of donated lungs many patients currently on transplantation lists will succumb to their disease before transplantation [2].

Furthermore, the development of safe and effective drugs is currently constrained by the lack of a robust preclinical models. Existing animal models often lead to failure of drug compounds after human clinical trials, implicating tremendous cost of drug development and long timelines. For these reasons, there is a crucial need for new technologies that can quickly and reliably predict drug safety and efficacy in humans in preclinical studies.

One approach to meeting this challenge is the development of three-dimensional cell cultures in which cells are grown within extracellular matrix (ECM) gels to induce expression of more tissue-specific functions. These models are currently being used for testing drug efficacy and toxicities; however, they fail to provide organ-level functionalities (molecular transport across tissue-tissue interfaces, contributions of vascular and airflow, etc.) that are required for the development of meaningful disease models.

Problems to be faced in the development of any complex tissue, including lung, depend on the development of better systems to promote angiogenesis, the selection of appropriate cell sources, the reproducible differentiation of the selected cell type or types along organ-

---

specific lineages, and the development of appropriate scaffolds or matrices to enhance and support three-dimensional (3D) production of tissues[1].

Thus, there is a need for advanced *in vitro* models of the lung to improve candidate treatments prior to moving to human clinical trials. In this work, a thermosensitive collagen-based hydrogel was used to develop a layered construct, fabricated through microextrusion bioprinting in order to create an *in vitro* model of the lung alveoli unit. Further characterization and improvements will enable this lung tissue model to extend its utility for *in vitro* drug testing, to help identify signaling pathways and mechanisms for new drug targets, and potentially reduce animal models as standard pre-clinical models of study.

## 1.2 Overview of the Lung Tissue

### 1.2.1 *Organization of the respiratory system*

The respiratory system is divided into the upper and lower respiratory tract. Air enters the body via the upper respiratory tract that includes nasal and oral cavities. The lower respiratory tract includes the larynx, the trachea, the right and left primary bronchi and all the constituents of both lungs. The lungs are the major organs of the respiratory system and are responsible for performing gas exchange.

The respiratory system can also be said to be divided into conduction and respiratory regions. The upper respiratory tract and the upper most section of lower respiratory tract form the conduction region, in which air is conducted through a series of tubes and vessels. The respiratory region is the functional part of the lungs, in which external respiration takes place and consists of respiratory bronchioles, alveolar ducts, alveolar sacs and alveoli [2].

### 1.2.2 *External respiration*

**External respiration** is the process how oxygen diffuses from the lungs to the bloodstream and how carbon dioxide diffuses from blood to the lungs. Deoxygenated blood is delivered to the lobules via capillaries that originate from the right and left pulmonary arteries. Once reoxygenated, blood is sent back to the left-hand side of the heart via pulmonary veins, ready to be ejected into systemic circulation. External respiration only occurs beyond the respiratory bronchioles and the alveoli [2].

### 1.2.3 *Respiratory portion*

The terminal bronchioles give rise to respiratory bronchioles, which lead to alveolar ducts, alveolar sacs and alveoli. Basically, the respiratory system consists of a branching set of air spaces, which are in close proximity to pulmonary capillaries. This arrangement means there is a fast-efficient transfer of oxygen and carbon dioxide between the blood and the air [2], [3].

#### 1.2.3.1 Alveoli

The distal portion of the lung is formed by multifaceted and cup-shaped compartments called alveoli that have diameters of 150 to 500  $\mu\text{m}$ . Gaseous exchange between the blood and air takes place in the alveoli. Alveoli share structural walls with neighboring alveoli, and the space that separates an alveolus from its adjacent neighbor is referred to as the alveolar septum, which is composed of a layer of epithelial cells on the surfaces in contact with air, endothelial cells that line the capillaries that allow blood flow through the septal tissue, and matrix materials that comprise the basement membrane and interstitial space [4].

### 1.2.3.2 Alveolar Lining Cells

The alveolar epithelium itself is made up of two main cell types:

**Type I pneumocytes:** large flattened cells connected to each other by tight junctions and are underlined by a well-developed basal lamina. These cells numerically constitute only 40% of the alveolar lining cells but cover 90% of the alveolar surface, which represent a very thin diffusion barrier for gases [3], [5].

**Type II pneumocytes:** cuboidal cells that constitutes 60% of the total number of cells but covers only approximately 5% of the alveolar surface. These cells are connected to the epithelium and other constituent cells by tight junctions. They function is to secrete 'surfactant' which decreases the surface tension between the thin alveolar walls, and stops alveoli collapsing. Besides secreting surfactant, the type II alveolar lining cell also serves as the reserve cell, maturing into the type I cell [3], [5].

### 1.2.3.3 Alveolar septum

As mentioned previously, the alveolar septum, apart from cells, it is composed of matrix materials that comprise the basement membrane and interstitial space. The alveolar basement membrane that supports the epithelial cells; is composed of collagen, elastin, proteoglycans, and other ECM proteins; and is regulated by matrix metalloproteinases. Collagen is considered to higher strength the parenchyma, because it resists loads induced by large distension. Then, elastin allows the lung parenchyma to return to its original shape following deformation while proteoglycans contribute significantly to the mechanical structure of lung tissue, since they act as connectors between various load-bearing proteins[4].

### 1.2.3.4 Air-Blood Barrier

The endothelial and epithelial alveolar type I cell cytoplasm is spread as thinly as possible and the basal laminae are fused, leading to an air-blood barrier. The thickness of the alveolar-capillary barrier varies from 0.2 to 2.5  $\mu\text{m}$  [3].

The alveolar interstitial cells and interstitial fibers are minimal, between a rich inter-anastomosing network of capillaries.

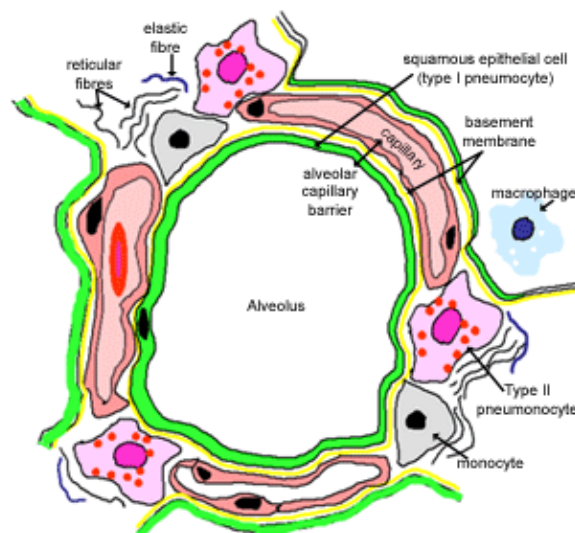


Figure 1.1 Air-Blood Barrier.

### 1.2.3.5 Capillary Endothelium

Endothelial cells are connected to each other by loose junctions, compared to the tight junctions of alveolar epithelial cells, and therefore more readily allow the passage of fluids and macromolecules into the interstitial compartment.

Serving as a barrier and actively regulating gas, water, and solute transport, the pulmonary endothelium also selectively processes and modifies a wide range of substances like the conversion of angiotensin I to angiotensin II [5].

### 1.2.3.6 Other Cells and Structures in the Alveolar Wall

Mesenchymal cells, including fibroblasts, pericytes of capillaries are present in the alveolar septum adjacent to the capillary and constitute the non-gas-exchanging portion of the septum [5]. They are responsible for the maintenance and metabolism of the elastic and collagen fibers and proteoglycans in the alveolar walls, contributing to the mechanical properties of the alveolus. Myofibroblasts (contractile interstitial cells) participate in the regulation of blood flow.

Typically, macrophages reside in the alveolar air space, but other immune cells can also be recruited into the interstitial space or into the air space[4]. Neutrophils, eosinophils, lymphocytes, plasma cells, basophils or mast cells, and fixed or migratory macrophages are present in small numbers in the alveolar wall and bronchial interstitial space [5].

### 1.3 Tissue Engineering (TE)

Tissue engineering refers to the practice of combining scaffolds, cells, and biologically active molecules into functional tissues. The goal of tissue engineering is to assemble functional constructs that enable the *in vitro* study of human physiology and pathophysiology, while providing a set of biomedical tools with potential applicability in toxicology, medical devices, tissue replacement, repair and regeneration [6], [7].

**Scaffolds.** A scaffold is a three-dimensional matrix in which cells are embedded displaying a set of critical signals for the determination of cellular proliferation, differentiation maintenance and function. A major goal in TE is the design of scaffolds capable of recreating the *in vivo* microenvironment, which is mainly provided by the extracellular matrix (ECM) [6].

Extracellular matrix (ECM) is a non-cellular three-dimensional network composed of collagens, proteoglycans/glycosaminoglycans, elastin, fibronectin, laminins, and several other glycoproteins, in which cells are embedded providing an essential physical scaffolding for the cellular constituents. Matrix components bind each other as well as cell to adhesion receptors forming a complex well-organized network. Cells interact with this macromolecular network through their surface receptors and regulates diverse cellular functions, such as survival, growth, migration and differentiation, vital for maintaining normal homeostasis [5].

**Cells.** What are the most suitable cells to use for any given tissue? Cells from native tissue could be the most suitable cell source but the first difficulty regards the number of cells necessary to provide a basis for tissue growth. The extraction of cells is generally done in humans by biopsy and usually results in an insufficient cell number, so there is the need of culturing and expand them. Although almost any cell types can be expanded, the process induces the loss of their particular phenotype; in other words, they dedifferentiate. As a result, once a sufficient number of cells have been reached, they have to be redifferentiated to the desired phenotype, which is not easily attainable [8].

Another approach consists of using undifferentiated cells, stem cells either Embryonic (ESCs) or Adult (ASCs). In adults, there are pools of undifferentiated cells which allow self-renewal of the organism over a lifespan, they have been isolated from different tissues including bone marrow, muscle and adipose tissue and umbilical cord. These cells, once isolated, can be differentiated in highly specialized tissues (multipotency) if provided the right conditions. It is important to full control the final phenotype before implantation. Furthermore, dedifferentiation is also possible [8].

An alternative cell type under study are induced Pluripotent Stem Cells (iPSCs), somatic cells that have been reprogrammed to a pluripotent state through the introduction of a defined set of transcription factors. The main advantages of these cells are their

autologous character, their differentiation capacity and the robustness and simplicity of reprogramming procedure [6].

**Bioactive molecules.** The presence and gradient of soluble factors such as GF, chemokines, and cytokines play an important role in biological phenomena such as chemotaxis, morphogenesis and wound healing. Can be added to the culture media as soluble factors or attached to the scaffold by covalent and non-covalent interactions. They modulate several aspects of cell biology, from proliferation capacity to specific phenotypic features of fully differentiated cells [6].

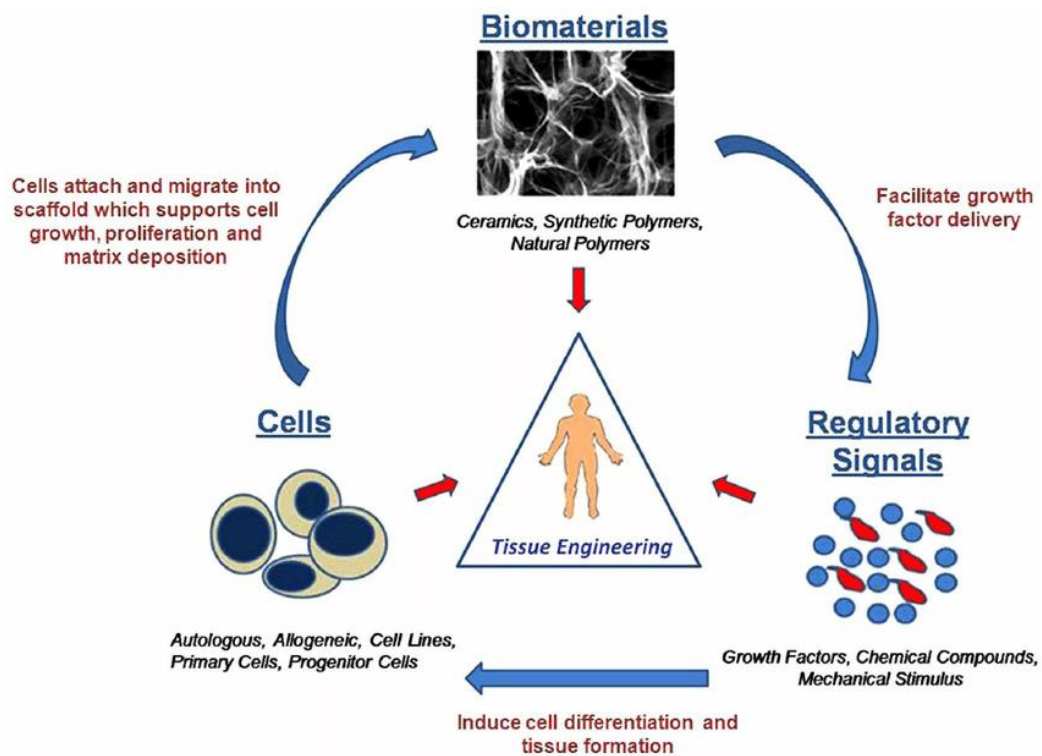


Figure 1.2 The three-essential component of TE [3].

## 1.4 Engineered tissue models of lung parenchyma

### 1.4.1 *Introduction*

Initially, cell culture studies have been performed on two-dimensional (2D) surfaces such as micro-well plates, tissue culture flasks, and Petri dishes because of the ease, convenience, and high cell viability of 2D culture. Thanks to these conventional cell culture systems, the science community has notably improved the understanding of basic cell biology, but 2D culture substrates not only fall short of reproducing the complex and dynamic environments of the body, but also are likely to misrepresent findings to some degree by forcing cells to adjust to an artificial flat, rigid surface. In the body, nearly all tissue cells reside in an extracellular matrix (ECM) consisting of a complex 3D fibrous meshwork that provide complex biochemical and physical signals. Two-dimensional substrates are considerably limited in emulating these complex 3D microenvironments because of the lack of structural architecture.

For that reason, three-dimensional cell culture matrices, also known as scaffolds, were introduced to overcome 2D culture limitations. These matrices are porous substrates that can support cell growth, organization, and differentiation on or within their structure. Architectural and material diversity is much greater on 3D matrices than on 2D substrates.

Applications of scaffolds can be divided into clinical and *in vitro* 3D modeling approaches. Clinical applications mainly consist of tissue engineering or regenerative medicine, which target the creation of a functional implants using artificial 3D matrices. The other application of a 3D matrices is their use as an *in vitro* 3D model system. Here, the aim is to facilitate systematic analysis of cell biology at the molecular level that will significantly improve the understanding of tissue physiology and pathophysiology [9].

Focusing on an *in vitro* application, hereafter, it is summarized the different tissue model systems that have been used to study the lung physiology. Initially, a brief overview of animal models and two-dimensional (2D) models are presented, highlighting advantages and limitations associated with each one. Followed by three dimensional (3D) models, discussed in relatively greater detail, due to their better mimicry of *in vivo* conditions and therefore increased usage towards modeling pulmonary tissue, along with the pros and cons.

### 1.4.2 *Animal Model*

#### 1.4.2.1 Animal models to recapitulate human diseases

Living systems like human beings and animals are extremely complex. Studying cell cultures in a petri dish, while sometimes useful, does not provide the opportunity to study interrelated processes occurring in the central nervous system, endocrine system, and immune system. Animal models have been developed to study the evolution of specific

diseases and identified several key mediators in different pathologies as an alternative to testing on a living, whole-body system.

An example of application of animal models can be the study of IPF (Idiopathic pulmonary fibrosis) made by Moeller et. al [10], as many others, in rodents. In humans, studying IPF is complicated by the fact that it is an age-related disease, so animal models have been developed to study the evolution of fibrotic responses and identify the key mediators in pulmonary fibrosis. Bleomycin is an antibiotic that, when it is administered intratracheally, causes inflammatory and fibrotic reactions within a short period of time (~1–2 weeks). One of the major drawbacks of using bleomycin is the inability to model the chronic nature of IPF. Repeated dosages are required to replicate chronic fibrosis. The advantages of the model include (a) its ease of replication with different routes of administration (b) well established dosage (c) replication of histological hallmarks of IPF, among others.

Another case of animal model application is the study carried out by Thotala et al. [11] at the Washington University in St. Louis. The group assayed the effect of a specific inhibitor (PLA-695) of the cytosolic phospholipase A2 (cPLA 2), a molecule that is associated with tumor progression and radioresistance in mouse tumor models. They found that PLA-695 inhibits cPLA2, radiosensitizing non-small cell lung cancer (NSCLC) cells and tumors, enhancing the efficacy of radiation, inducing cell death and attenuating invasion of lung cancer cells in two mouse models of lung cancer. In addition, PLA-695 inhibited the formation of new blood vessels and angiogenesis.

#### 1.4.2.2 Limitations

Compounds showing efficacy in limiting these pathologies in pre-clinical animal models have failed human clinical trials and the other way round some chemicals that are ineffective on, or harmful to, animals prove valuable when used by humans. The translation of results from pre-clinical animal models to humans is complicated by the fact that animal models possess inherently different airway anatomy, lung cell biology and immunity. Furthermore, it is cost effective in the way pathology is induced, the disease development in an animal model occurs over a long-term period of time [9].

The ethical aspect is another important matter. Performing animal testing is cruel and inhumane.

<i>ANIMAL MODELS</i>	<i>Uses</i>	<i>Advantages</i>	<i>Limitations</i>
	<i>Performing pre-clinical trials on a living, whole-body system</i>	<ul style="list-style-type: none"> <li><i>-Animal testing has contributed to many life-saving cures and treatments</i></li> <li><i>-There is no adequate alternative to testing on a living, whole-body system</i></li> <li><i>-Shorter life cycles</i></li> </ul>	<ul style="list-style-type: none"> <li><i>-Interspecies variability</i></li> <li><i>-Drugs that pass animal tests are not necessarily safe</i></li> <li><i>-Animal tests do not reliably predict results in human being</i></li> <li><i>-Ethical considerations</i></li> </ul>

Table 1. Summary of advantages and limitations of animal models [9].

### 1.4.3 Two-dimensional (2D) cell culture models

Two-dimensional (2D) models enable study of cell responses in a controlled setting with the ability to tweak individual cell responses to soluble cues, matrix molecules and matrix mechanics. Although, studies increasingly favor 3D, due to their better mimicry of *in vivo* conditions, 2D studies still maintain their role as a robust platform of *in vitro* investigation, due to the relative ease of imaging and profiling cells for genes expression and are concurrently used with other platforms of investigation for modeling lung diseases [9].

#### 1.4.3.1 Tissue culture plastic (TCP) or glass substrates

Provide researchers with a standard platform to evaluate single cell responses to soluble growth factor and extracellular matrix (ECM) cues. These 2D culture platforms are often multiplexed with animal studies or other culture types. Further, mechanically tunable substrates have been used to assess the effect of substrate mechanics on lung cell phenotype (e.g., pulmonary fibrosis) [9]. For example, in the study carried on by Engler et al. [12], tunable substrates have been used to assess the effect of substrate mechanics on fibroblast phenotype associated with pulmonary fibrosis. Variable stiffness polyacrylamide hydrogels (PA) were prepared, as they are the most frequently used substrates for fibrotic disease modeling.

Mishra et al. [13] compared the growth of human lung cancer cells in an *ex vivo* 3D model with a 2D culture under the same culture conditions for 15 days. They found significant differences in the formation of tumor nodules, total cell numbers, proliferation rates, cell death rates, and matrix metalloproteinase (MMP) production. Moreover, the human lung cancer cells grown in the *ex vivo* 3D lung model produced MMPs that are found in human samples, whereas the cells from 2D culture did not. Overall, the human lung cancer cells grown in the *ex vivo* 3D lung model have features that mimic lung cancer growth and metastasis in patients, whereas the cells grown in 2D culture did not.

#### 1.4.3.2 Limitations of 2D cell culture models

After the Mishra et al. example it is clear that the primary limitation of 2D cell culture models is their inability to mimic the 3D nature of lung tissue. Tissue culture plastic and glass are extremely stiff substrates and because matrix stiffness has been

shown to affect cellular phenotype, standard TCP culture substrates do not permit studies evaluating cellular mechanics. Mechanically tunable substrates can replicate normal and diseased lung mechanics, however all 2D substrates force cells to attain an apical- basal polarity, unlike their natural state in vivo, where cells exhibit a more rounded morphology with integrin cell adhesions in all three planes. Further, 2D culture substrates cannot replicate the complex gradient nature of soluble cues found in vivo and the variety of cell-cell, cell-matrix interactions experienced by cells within the normal human lung. With respect to epithelial cells, 2D substrates do not permit ALI culture required for basal cell differentiation and airway maturation. Most 2D studies utilizing epithelial cells are therefore relatively short-term studies (e.g., days) using epithelial cell lines, devoid of basal stem cells and not entirely representative of in vivo lung epithelia [9].

<b>2D MODELS</b>	<b>Uses</b>	<b>Advantages</b>	<b>Limitations</b>
<b>Tissue culture plastic (TCP) and glass substrates</b>	<i>Evaluate individual cell responses to soluble and/or matrix cues</i>	<ul style="list-style-type: none"> <li>-Well-studied</li> <li>-High throughput capacity</li> <li>-Ease of profiling cells for gene expression</li> </ul>	<ul style="list-style-type: none"> <li>-Very high stiffness</li> <li>-Migration, chemotaxis, traction, integrin adhesions only in X-Y planes</li> <li>-No air-liquid interface (ALI)</li> <li>-No soluble gradients</li> <li>-Forced apical-basal polarity</li> <li>-Limited cell-cell and cell-matrix interactions</li> </ul>

Table 2. Summary of advantages and limitations of 2D models [9].

#### 1.4.4 From 2D to 3D systems

##### 1.4.4.1 Transwell cell culture systems

Transwell systems is a closer approach to 3D models, as they permit studies of immune cell epithelial transmigration, endothelial extravasation and air-liquid interface (ALI) cultures of pulmonary epithelial cells.

While transwell monolayer cultures of epithelial/endothelial cells can be considered as transitional 2D to 3D systems, as they are monolayer cultures supporting fibroblast integrin adhesion only in the X-Y plane but enable reproduction of complex organ/tissue level processes including leukocyte transmigration and extravasation. The inclusion of a hydrogel encapsulated stromal fibroblast layer results in soluble growth factor gradients and differential integrin signaling, thereby constituting a 3D system.

Transwell cultures also permit epithelial maturation via ALI, a feature that is not possible with 2D cell cultures but achieved by most 3D cultures [9].

An example of application of transwell system is the research carried out by Katja Hattar et. al [14], where they study the crucial role that inflammatory tumor microenvironment plays in tumor progression, in this case, in lung cancer. In transwell-experiments, they

characterized the effect of isolated human neutrophils on proliferation of the non-small cell lung cancer (NSCLC) cell line A549. This pro-proliferative effect of neutrophils on A549 cells demonstrated to be depend (in a dose-dependent manner) on direct cell-to-cell contact.

#### 1.4.4.2 Basement membrane cell culture

The advent of new culture platforms to better mimic the 3D lung microenvironment has resulted in sandwich models and ECM cultures. The mentioned systems enable the formation of higher-level 3D epithelial acinar structures, albeit exposed to media on one surface.

In the normal human lung, both airway epithelial cells and microvascular endothelial cells are polarized structures attached to an underlying basement membrane. Airway epithelial and microvascular endothelial cells cultured on Matrigel basement membrane produce complex 3D structures, not reproducible by 2D systems, so basement membrane cell culture can also be considered as transitional 2D to 3D systems.

Microvascular endothelial cells from the lung and other sources undergo differentiation forming 3D tubular structures, replicating angiogenic programming when plated on Matrigel membranes [9]. Tahergorabi Z. et. al [15] with the scope of evaluating angiogenesis, performed appropriate assays using Matrigel based membranes to evaluate therapeutic angiogenesis (clinical manipulation of angiogenesis) and its importance during some clinical diseases.

#### 1.4.4.3 Sandwich cell culture

Neither transwell nor basement membrane culture systems support fibroblast integrin adhesions in X, Y and Z planes. Sandwich cultures are relatively newer *in vitro* models and are essentially fibroblasts or other cells sandwiched between two layers of mechanically tunable substrates (e.g., polyacrylamide), supporting integrin adhesions in all planes, like 3D models [9]. Although few or no studies have utilized these platforms for lung modeling, hepatocyte sandwich cultures have been widely used to investigate cell-cell and cell-ECM interactions, consisting of a monolayer of hepatocytes sandwiched between two layers of extracellular matrix (ECM) [10]. For example, Kern et al. [16] showed that sandwich culture of human hepatocytes, was an effective means of maintaining enzyme activity similar to in vivo levels, proving that sandwich culture can retain functional stability to enable studies of drug metabolism and enzyme induction of the liver.

#### 1.4.4.4 Limitations

Transwell systems and basement membrane cultures as 2D models, have the limitations that they do not contain soluble growth factor gradients and do not support integrin adhesions in all planes. Further, both systems are limited in their mechanical tunability.

Sandwich cultures overcome some of these limitations and are the closest to 3D systems, as they enable integrin adhesions in all planes, contain growth factor gradients and possess greater mechanical tunability. However, the ability of sandwich cultures to enable 3D migration, chemotaxis studies, are largely dependent on the hydrogels used. Finally, 2D to 3D systems provide greater cell-cell and cell-ECM interactions compared to 2D systems, they do not accurately mimic the varied cell and matrix interactions found in the human lung and thus are primarily used to evaluate the role of individual protein/matrix cues on cellular processes [9].

<i>From 2D to 3D models</i>	<i>Uses</i>	<i>Advantages</i>	<i>Limitations</i>
<i>Transwell systems</i>	<i>Epithelial air-liquid interface (ALI) culture and co-culture studies to investigate paracrine interactions</i>	<ul style="list-style-type: none"> <li>-High throughput</li> <li>-Migration, chemotaxis in all planes</li> <li>-Ease of profiling cells for gene expression</li> </ul>	<ul style="list-style-type: none"> <li>-Integrin adhesions only in X-Y plane</li> <li>-Forced apical polarity</li> <li>-No soluble gradients</li> <li>-No control over stiffness</li> </ul>
<i>Basement membrane culture</i>	<i>Evaluate acini formation with epithelial cells and tubule formation with endothelial cells</i>	<ul style="list-style-type: none"> <li>-High throughput</li> <li>-Migration, chemotaxis in all planes</li> <li>-Ease of profiling cells for gene expression</li> <li>-Cell-cell and cell-matrix interactions</li> <li>-Higher order epithelial structure</li> </ul>	<ul style="list-style-type: none"> <li>-Integrin adhesions only in X-Y plane</li> <li>-No soluble gradients</li> </ul>
<i>Sandwich culture</i>	<i>Evaluate 3D lung cell responses similar to hydrogel systems</i>	<ul style="list-style-type: none"> <li>-High throughput</li> <li>-Migration, chemotaxis in all planes</li> <li>-Integrin adhesions in all planes</li> <li>-Cell-cell and cell-matrix interactions</li> <li>-No forced polarity</li> <li>-Tunable stiffness fabrication</li> <li>-Does not require confocal microscopy imaging</li> </ul>	<ul style="list-style-type: none"> <li>-3D migration, chemotaxis studies, are dependent on the hydrogels used</li> </ul>

Table 3. Summary of advantages and limitations of different 2D to 3D models [9].

### 1.4.5 Three-dimensional (3D) cell and tissue culture models

Three dimensional *in vitro* models replicate native lung tissue microenvironment with greater accuracy compared to the previous models mentioned. Both paracrine cellular and matrix signaling take place in 3D models. Therefore, successful 3D models are those which replicate cell-cell and cell-matrix interactions, while mimicking native matrix stiffness and structure. They permit migration, chemotaxis, cellular traction and integrin adhesions, in all three planes. Further, these systems replicate soluble growth factor gradients and support ALI epithelial maturation, similar to *in vivo* conditions [9].

#### 1.4.5.1 Hydrogel systems

Hydrogels are water-swollen cross-linked natural or synthetic polymers mimicking human tissue composition for *in vitro* study. Depending on the polymeric network and crosslinking mechanism, hydrogels can be mechanically tuned. Hydrogels fabricated from collagen type I are the most-studied 3D culture system. For example, Rutter et. al [17] studied volatile biomarkers released by tumor cells with the scope of founding volatile compounds in exhaled breath and other biological fluids as biomarkers of tumors *in vivo*. Lung cancer cells and non-malignant lung cells were seeded in 3D collagen hydrogels at different cell concentrations and the release of acetaldehyde was measured. The same experiment has been carried out in 2D models in previous studies. The data obtained by Rutter et. al showed that the amount of acetaldehyde released by both cell types grown in a 3D model is higher when compared to that of the same cells grown in 2D models.

One of the significant limitations of natural hydrogels is the inability to support long-term *in vitro* culture, due to contraction/degradation during *in vitro* culture. Commonly used synthetic hydrogels for studying fibroblast biology include polyacrylamide hydrogels (PA) and poly-ethylene-glycol (PEG) hydrogels. PA hydrogels have toxic precursors and therefore are primarily used as 2D mechanically tunable substrates. PEG hydrogels enable 3D culture of cells possess mechanical tunability [9].

#### 1.4.5.2 Decellularized matrices

Decellularization is the removal of cells from a tissue or organ using detergents, leaving a complex mixture of structure and functional proteins that constitute the ECM. The final goal of decellularization is often *in vivo* implantation, where donor decellularized lungs can be reseeded with recipient cells (adult or stem cell populations) for tissue replacement. Decellularized lungs have emerged as models for *in vitro* study of pulmonary diseases, as they mimic native lung ECM composition, structure and stiffness. However, access to human lung tissue is a significant limitation [9]. Mishra et. al [13] compared the growth of human lung cancer cells in an *ex vivo* 3D lung model (decellularized lung matrices from rats) and 2D culture to determine which better mimics lung cancer growth in patients. The human lung cancer cells grown on *ex vivo* 3D model and organized tumor nodules with intact vascular space formed but not in 2D culture.

#### 1.4.5.3 Precision cut human/animal lung tissue (PCLT)

Normal or diseased lung tissue slices for *in vitro* investigation without decellularization are termed precision cut lung tissue (PCLT) slices or ex vivo lung tissue. PCLTs retain native lung tissue architecture, ECM protein composition and stiffness, with viable lung cells, similar to in vivo conditions [9].

Lehmann et al. [18] treated human and mouse PCLTs with different concentrations of pirfenidone and nintedanib, the only approved drugs known to decelerate the IPF progression. They utilized 2D cultures of ATII (Alveolar cells type II) to corroborate their findings. PCLTs represent a better tool to analyze antifibrotic mechanisms of the mentioned drugs. Moreover, both drugs regulate epithelial cell gene expression, contributing to their antifibrotic activities.

The problems with culture of tissue slices are that human organ slices can be difficult to obtain and survival of slices is limited to a few days [19].

#### 1.4.5.4 Lung spheroids and organoids

Lung spheroids refers to adult lung cells or lung stem cell populations cultured in the form of aggregates utilizing low-adhesion plates, hanging drop cultures, suspension cultures or micropatterned plates. Lung organoids are self-assembling structures of lung stem cells that follow sequential lung development, with discrete pseudoglandular, canalicular and saccular stages.

Both lung spheroids and organoids replicate cell-cell, cell-matrix interactions, human lung organ structure/function and are often multiplexed with other 3D culture systems. Studies utilizing spheroid cultures are often targeted towards recreating higher organ level 3D complexity with the goal of *in vitro* drug or toxicology testing [9].

Studies have shown the long-term culture capacity (up to 3 months) and both systems permitted chronic drug testing. Lung spheroids and organoids self-assemble into structures similar to the human lung (e.g., alveolar-capillary structure), although they do not replicate lung function.

Wilkinson et al. [20] developed a 3D bioengineered lung model, self-assembled human lung organoids, utilizing fetal lung fibroblasts seeded on functionalized 3D alginate hydrogel spheres, and presented their potential for disease modeling and drug discovery for lung diseases such as IPF. A model of the progressive scarring observed in IPF was generated by treating the cells with exogenous transforming growth factor- $\beta$ 1 (TGF- $\beta$ 1), showing efficacy in modeling the disease. Further studies incorporated, into the organoid seeding process, multiple other relevant cell types, indicating that could be applicable for modeling other lung diseases.

Spheroids are widely used for modeling cancer. They represent a better model compared with monolayer cultures as they mimic both architecture and share the limited drug penetration properties since drugs are largely confined to the outer cell layers. For

example, Xu et. al [21] study how to radiosensitize non-small cell lung cancer multicellular spheroids using doxorubicin-encapsulated micelles to achieve reduced toxicity and a higher therapeutic effect.

A primary limitation with both systems is the variability in the way they present highly variable size and shape, making it difficult to obtain consistent biologically meaningful results, especially regarding drug efficacy testing. Lung organoids do not develop fully due to the lack of vascularization.

Further, imaging of these structures has been difficult due to their 3D nature and migration inside hydrogel systems, making it difficult for long term time-lapse imaging. Finally, neither system permits ALI culturing and therefore lung epithelial cells cultured in these systems do not attain their terminally differentiated state [9].

#### 1.4.5.5 Limitations

Even if each type of 3D culture model has been discussed previously along with their particular limitations, it is necessary to mention a common drawback that all these systems share to proceed with the introduction of the last 3D model. The previous devices lack the ability to reproduce complex, dynamic mechanical and biochemical microenvironments that play a critical role in organ development and function. These models are currently being used for testing drug efficacy and toxicities; however, they fail to provide organ-level functionalities (molecular transport across tissue-tissue interfaces, contributions of vascular and airflow, etc.) required for the development of meaningful disease models [22]. A potential solution to this problem is the development of microfluidic devices that recapitulate the physiological and mechanical microenvironment of whole living organs, discussed below in detail.

#### 1.4.5.6 Lung-on-chip

Organ on chip devices are bioengineered devices which replicate organ/tissue level responses in miniature chips created using lithography techniques. Lung on chip devices are 2D systems, similar to transwells, in that they contain monolayers of epithelial/endothelial cells, providing the possibility of investigating under a much more dynamic environment, with biomechanical cues in the form of shear stress due to perfusion and strain similar to human breathing. Sellgren et al. [23] presented an advanced a three-dimensional (3D) model by co-culturing interstitial fibroblasts with epithelial and endothelial cells, separated by porous membranes. Sellgren et al. showed the feasibility of including a stromal layer within lung on chip devices.

With the aim of studying IPF, Mondrinos et al. created a human organ fibrosis chip by encapsulating fibroblasts within collagen hydrogels inside the lung on chip device where, modulating the soluble microenvironment, they were able to activate fibroblast into a pathologic phenotype [1] .

Lung-on-chip platforms are the only 3D *in vitro* tissue system replicating lung function in the form of breathing (strain) and blood flow (shear due to perfusion). These systems replicate the lung alveolar-capillary structure.

#### 1.4.5.7 Limitations

Although organ-on-chip microdevices are a robust platform for mimicking the key structures and functions of lung tissue, they also have limitations. Firstly, there are inherent limitations associated with these systems, including technical difficulties like bubble formation which are known to injure cells, contraction/degradation of ECM gels or coatings or microbial contamination that is often associated with long-term culture systems [9]. Secondly, usually the porous membranes are PDMS made and they differ in thickness and mechanical properties from their *in vivo* counterparts, and even more not being able to mimic the composition of the ECM, the main goal of the current thesis.

Another potential limitation is the irreversible permanent bonding between PDMS layers, which is required to construct organ chips, making it technically challenging to access, isolate and process intact human tissues produced in the microdevice for certain types of analysis, such as histology and electron microscopy. Relying on fluorescence microscopy, microfluorimetry and real-time imaging for analysis.

Small airway-on-a-chip devices have been *in vitro* cultured for 5 weeks and future work will determine whether these systems can be sustained for longer time periods [9].

<i>3D models</i>	<i>Uses</i>	<i>Advantages</i>	<i>Limitations</i>
<i>Hydrogel systems</i>	<i>Model early and late stages of wound remodeling</i>	<ul style="list-style-type: none"> <li>-Easy fabrication</li> <li>-Easy availability</li> <li>-High throughput capacity</li> <li>-Low costs</li> <li>-Thickness, dimensional tunability</li> </ul>	<ul style="list-style-type: none"> <li>-Cannot model long-term responses, undergoes degradation and contraction (collagen)</li> <li>-Limited mechanical tunability</li> </ul>
<i>Decellularized matrices</i>	<i>Models for in vitro study of pulmonary diseases and in vivo implantations</i>	<ul style="list-style-type: none"> <li>-Cell-matrix interactions similar to in vivo</li> <li>-Retain native matrix stiffness</li> <li>-High throughput capacity</li> <li>-Can be stored frozen</li> <li>-Long-term culture</li> <li>-Thickness, dimensional tunability</li> <li>-Time-lapse live imaging</li> </ul>	<ul style="list-style-type: none"> <li>-Decellularization related ECM loss</li> <li>-Access to human, animal lung samples</li> <li>-Loss of cell-cell interactions</li> </ul>
<i>Precision cut human/animal lung tissue (PCLT)</i>	<i>In vitro culture substrate mimicking native or disease lung microenvironment</i>	<ul style="list-style-type: none"> <li>-Accurate cell-matrix interactions</li> <li>-Thickness, dimensional tunability</li> <li>-High throughput capacity</li> <li>Time-lapse live imaging</li> </ul>	<ul style="list-style-type: none"> <li>-Short-term culture</li> <li>-Requires fresh live human, animal samples</li> <li>-Storage not possible</li> </ul>
<i>Lung spheroids and organoids</i>	<i>Recreating higher organ level 3D complexity for in vitro drug or toxicology testing</i>	<ul style="list-style-type: none"> <li>-High throughput capacity</li> <li>-Relatively easy fabrication (spheroids)</li> <li>-Replicate cell-cell, cell-matrix interactions</li> </ul>	<ul style="list-style-type: none"> <li>-Variation in size</li> <li>-Difficult to observe via live imaging</li> <li>-Heterogeneities in drug penetration</li> <li>-Do not support ALI culture</li> <li>-Requires long-term culture (organoids)</li> </ul>
<i>Lung-on-chip</i>	<i>Evaluate effects of drugs, genes, cell responses due to dynamic lung microenvironment</i>	<ul style="list-style-type: none"> <li>-Replicates dynamic organ level processes including cyclical strain breathing and shear stress due to blood flow, not possible with other systems</li> <li>-Replicate cell-cell, cell-matrix interactions</li> </ul>	<ul style="list-style-type: none"> <li>-Time-lapse live cell imaging requires complex imaging equipment</li> <li>-Materials used for the fabrication of the chip differ in thickness and composition from their in vivo counterparts</li> </ul>

Table 4. Summary of advantages and limitations of different 3D models [4].

## 1.5 Three-dimensional matrix fabrication techniques: State of Art

### 1.5.1 First considerations: structural and materials properties

It is clear 3D systems are superior in that they better represent the geometry, chemistry, and signaling environment of natural extracellular matrix. There are structural properties and essential material properties that need to be considered at multiple scales for successful replication of natural ECM [9].

Structure: A multi-scale approach is especially important in mimicking living systems, because nature is characterized by hierarchical structures. Multiple levels of structural control include matrix size and shape, pore size, geometry and density, pore interconnectivity, and surface topology. Multiple scales can be defined:

- Macro-scale ( $10^{-1}$ – $10^{-3}$  m), determines properties of a 3D matrix including size and shape.
- Micro-scale ( $10^{-3}$ – $10^{-6}$  m), is valuable to mimic the microscopic tissue structure, such as the multi-cellular spatial organization within ECM proteins, closely interrelated with tissue architecture and function. One of the critical issues in microscale design is the facilitation of mass transport, therefore pore geometry, size and distribution are other critical factors.
- Nano-scale ( $10^{-6}$ – $10^{-9}$  m), Cell-ECM interaction take place via nanoscale proteins, responding to their environment by modulating various cellular activities. Surface topography have a significant influence on cell functions at nanoscale in that it regulates cell adhesion, organization, morphology, and differentiation [9].

Thus, multiple scales must be considered to proper design of 3D cell culture matrix structure that will provide distinct features to the matrix, such as macro-scale shape, micro-scale internal architecture, and nano-scale surface topology.

Biomaterials: they can be divided into 4 groups: metals, ceramics, polymers, and composites. Due to versatility of polymeric materials, specifically biodegradable ones, they are rapidly replacing other biomaterial classes, such as metals, alloys, and ceramics for use in biomedical applications[24]. Polymeric materials can be divided into natural and synthetic polymers and their innate properties have been summarized in Table N° 5.

<i>Natural polymers</i>		<i>Synthetic polymers</i>	
<i>PROS</i>	<i>CONS</i>	<i>PROS</i>	<i>CONS</i>
<ul style="list-style-type: none"> <li>- Biocompatible</li> <li>- Biomimetic</li> <li>- Bioactive</li> </ul>	<ul style="list-style-type: none"> <li>- Difficult to control degradation rate</li> <li>- Poor mechanical stability</li> <li>- Undesirable immunological effects</li> <li>- Temperature sensitive</li> <li>- Transfer of pathogen is possible</li> </ul>	<ul style="list-style-type: none"> <li>- Versatility</li> <li>- Control over degradation and other derived properties</li> <li>- Control over bulk and surface properties</li> <li>- Tuned mechanical properties</li> </ul>	<ul style="list-style-type: none"> <li>- Degradation products may cause adverse effects</li> <li>- Non biomimetic properties</li> </ul>

Table 5. Summary of advantages and limitations of both natural and synthetic polymers.

Bulk properties: includes biocompatibility, wettability, transparency, biodegradability, and mechanical properties.

- Biocompatibility: depending on the application of the scaffold, the degree of biocompatibility can vary from the lack of toxicity with respect to in vitro cultures to the lack of long-term immunological systemic response of the human body regarding in vivo applications.
- Wettability: natural ECM is a fully hydrated gel so bulk materials with more hydrophilic chemistry are better at mimicking the aqueous in vivo environment.
- Transparency: transparent materials are advantageous to collect optical signals from optical-based instrumentation and also allows microscopic detection of cellular behaviors within the 3D matrix.
- Biodegradability: essential requirement for implantable 3D scaffolds in which biodegradability must be strictly controlled.
- Mechanical properties: scaffolds should have mechanical properties resembling those of healthy/disease tissue intended to be modelled in in vitro applications. In in vivo implementations, this factor is crucial to be insured over the period of tissue regeneration[9].

Surface properties: include stiffness, charge, polarity, and chemistry, among others. Surface properties determine the first interaction between cells and a substrate and as a result, the amount of protein adsorption and resultant cell adhesion[9].

### 1.5.2 Fabrication techniques

The earliest is the encapsulation of cells within a hydrogel matrix. In this culture format, a hydrated nano-scale fibrous structure similar to natural ECM surrounds cells completely.

Computer-assisted fabrication systems emerged with the greater necessity for complex and customized 3D matrix structure design and manufacture. Currently, the RP technique, known as rapid prototyping, is the most broadly used of computer assisted methods that allows control over macroscopic properties, as well as microscopic internal architecture[9].

#### 1.5.2.1 Cell entrapment technique

**Technique.** A hydrogel precursor solution is mixed with a cell suspension and then quickly gelled using random or self-assembling polymerization via changes of physical or chemical conditions. The exceptional advantage of this technique is that allows a complete interaction between cells and the 3D environment that completely surrounds them, enabling the delivery of signals to cells in all directions[9].

**Structure.** Normally, the mold in which they are formed defines macroscale structures. In the case that cell-entrapping precursor solution is dropped into an initiator solution, the structure takes on a spherical shape. There is no distinct microporous structure; thus,

mass transport mainly depends on slow diffusion through submicron-size pores. Although the ECM-like environment is an ideal condition for cell culture, weak mechanical properties are a major limitation of the exceptionally hydrophilic nature of the matrix[9].

**Biomaterials.** Three-dimensional cell entrapping materials are natural or synthetic hydrogels that can undergo fast polymerization around cells. The monomeric components must be nontoxic and biocompatible, because cells are mixed with the precursor solution before gelling. 3D hydrogel matrices show excellent wettability, and many demonstrate superior transparency in the UV-vis range. Surface properties of entrapping hydrogel are derived from bulk properties because 3D matrix completely surround cells. Mechanical properties of the matrix can be tuned by adjusting the concentration of monomer and cross-linker. Natural hydrogels, such as Matrigel, fibrin gel, alginate gel and collagen gel, are commonly applied as cell-entrapping materials because of their biocompatibility and mild gelling conditions. However, some of the major drawbacks include poor control of gelation kinetics, uncontrolled material composition, and lack of mechanical integrity[9].

Synthetic hydrogels have been introduced for greater control over physical and chemical properties of 3D culture environments, what significantly promotes reproducibility of experimental results. The homogeneous nature of synthetic hydrogels provides matrix uniformity and simpler biochemical assays than natural hydrogels. In contrast, synthetic hydrogels normally are not bioactive, and harsh polymerization conditions[9].

**Applications.** Cell-entrapment techniques have been used extensively in constructing 3D *in vitro* model systems because of distinct differences in cellular morphogenesis, function, migration, and differentiation from conventional 2D culture. For example, Weaver et al. [25] developed a human breast cancer model with epithelial cells cultured within 3D Matrigel. This was the first report of an acinus structure possessing a cellular morphology akin to that of an *in vivo* structure that was never observed in 2D culture. Subsequently, they treated the tumor cells with integrin blocking antibodies that led to a morphological and functional reversion to a normal phenotype.

#### 1.5.2.2 Polymer processing techniques

**Techniques.** Fibrous matrices are typically fabricated using an electrospinning process that can generate micro- or nano-scale diameters of fibers with simple set-up, inexpensive handling costs, and versatile material selection. High surface-to-volume ratio and a structure similar to the 3D fiber network of collagen and elastin in natural ECM[9].

Other types of matrices, sponge-like structures, displayed stochastic architecture. Sponge-like 3D substrates have a porosity and surface-to volume ratio that is similar to or lower than electrospun matrices but larger pores that can significantly improve cell seeding and migration. In this context, fabrication techniques can be divided into 2 groups based on whether a porogen is employed[9].

Freeze-drying and gas foaming are two methods that do not use a porogen. The freeze-drying process includes the use of organic solvents to dissolve polymer and can be recognized as a major hindrance that can be avoided with gas foaming. The gas-foaming process involves high-temperature compression molding of the polymer to form a solid disk-like structure then infiltrated with CO<sub>2</sub> at high pressure. As the pressure is decreased, the gas escapes the polymer, leaving a porous, sponge-like structure. As no organic solvent is used, gas foaming process is favorable for incorporating biological molecules[9].

Solvent casting and particulate leaching are representative methods of achieving a sponge-like porous matrix with a porogen. The concept behind particulate leaching is to mix polymer and solvent with particulates that can be dissolved with a separate solvent. Generally, synthetic polymers are dissolved in an organic solvent and mixed with porogen particles. Typical porogens include salt or sugar particles, because they are insoluble in organic solvents and can be removed by exposure to liquid water. The polymer–solvent–particulate mixture is then cast into a mold, and the solvent is evaporated, leaving a solid polymer–particulate construct. After exposing the construct to the particulate solvent, the remaining polymer will have a porous structure with empty cavities where the crystals resided[9].

The main difference between using or not a porogen is the effect in the pore interconnectivity of the sponge – like structure. In porogen-based techniques, particles in a porogen are frequently fused together.

**Structure.** The shape and size of the mold in which it is created or cutting a structure from a larger matrix piece normally determines the macro-scale structure of 3D matrices. In clinical applications, a patient-specific macro-scale scaffold structure is typically achieved by using 3D molds fabricated using computer assisted fabrication methods[9].

Characteristics of the micro-scale structure of fibrous 3D matrices include fiber diameter, fiber alignment, and pore size among fibers. Fiber diameter is sensitively affected by physical and electrical properties of polymer solution such as viscosity and conductivity. Fiber alignment can be achieved by modifying the design of the collector (i.e., a high-speed rotating frame) or by using 2 conductive electrodes separated by an insulating gap. Pore size can be controlled by using multi-layer spinning to create 3D matrices having micro-fiber and nano-fiber layers.

The micro-scale structural characteristics of sponge-like 3D matrices include porosity, pore interconnectivity, pore size and geometry, and pore distribution. The internal architecture of 3D sponge-like matrices leads to stochastic structure of scaffolds that contributes to the simplicity of its preparation but may not be beneficial in terms of its mechanical and mass transport properties[9].

**Biomaterials.** The electrospinning process is widely versatile as it employs a diverse set of synthetic polymers or combinations of synthetic and natural materials with functional nano-materials (e.g., DNA, hydroxyapatites, and proteins). For scaffolds fabricated using

gas foaming, because of the absence of organic solvent, many biologically active molecules can be incorporated.

In the solvent casting and particulate leaching technique, salt crystals, sugar spheres, and paraffin spheres are commonly used as porogen particles. Virtually any material that undergoes liquid to solid transition can be used as a bulk material, but synthetic polymers, particularly PLA, PGA, and their copolymers, are commonly used. Biological molecules can be incorporated into bulk materials combined with carrier systems to protect them from organic solvents[9].

**Applications.** In fibrous structures, fiber diameter and alignment are key parameters. Smaller fiber diameter tends to result in greater protein adsorption, which mediates cell interactions with scaffolds. For example, Woo et al. [26] observed that a nano-scale fibrous scaffold supported more serum protein adsorption than solid-wall scaffolds (four times more) and promoted almost twice the amount of osteoblastic cell attachment, demonstrating that the biomimetic nano-fibrous architecture serves as superior scaffolding for tissue engineering.

In sponge-like structures, pore size and pore interconnectivity are critical considerations for proper cell seeding and growth. For example, 3D matrices with similar pore sizes but different levels of pore interconnectivity made using heat-treatment of porogen caused significant differences in the surface. Uebersax et al. [27] developed 3D biomaterial matrices fabricated from silk fibroin with controlled pore diameter and pore interconnectivity with the scope of engineering bone starting from human mesenchymal stem cells (hMSC). In this study, they observed that scaffolds with higher levels of pore interconnectivity promoted cell migration distances, whereas the lack of interconnecting channels in control scaffolds limited cell migration, and most cells were observed near the surface.

#### 1.5.2.3 Computer-assisted fabrication

**Technique.** Computer-assisted fabrication has several advantages. Primarily, scaffolds can be manufactured as customized multi-scale 3D structures. Additionally, manufacturing is time effective and economical [9].

Fabrication consists of up to 3 steps: acquiring 2D image slices of a target specimen from CT, MRI, quantitative ultrasound, or other nondestructive imaging methods; designing micro-scale internal architecture and reconstructing the macro-scale 3D matrix shape using CAD or other software; and fabrication of the 3D matrix using automated layer-by-layer construction with SFF processes (Solid freeform fabrication). The 3 main types of SFF processing techniques are laser-based, nozzle-based, and printer-based systems[9].

Laser-based techniques include photopolymerization, in which a liquid monomer solution is exposed to a UV beam and as a result, polymerizes the exposed layer; and selective laser sintering (SLS) that uses a laser beam to scan a powder bed, raising the temperature and sintering the powder of the exposed area. Whereas, laser assisted bioprinting (LAB)

consist of focusing a laser beam on the ribbon (a transparent quartz glass slide coated with a gold absorbing layer), onto which a thin layer of cellularized ink is spread. The energy created by the incidence of the laser beam creates a cavitation that propels a microdroplet, containing cells, towards the receiving substrate [28]. Fused deposition modeling (FDM), a nozzle-based technique, extrudes molten scaffold material through a nozzle that moves in the x-y plane, directly building a 3D matrix in layers. Three dimensional printing is a process that deposits a liquid solution onto a bed using an ink jet printer, forming the 3D matrix layer by layer[9].

**Structure.** 3D matrix structural design for computer assisted fabrication is based on CAD design then used as instructions for the 3D printing of a matrix, using various materials, porosities and internal architectures.

Micro-scale features can be moderately controlled in that many geometries can be constructed, allowing for the design of numerous internal architectures. In contrast, control of internal structure on the scale of a few hundred microns and smaller is limited because of inherent constraints of manufacturing parts (e.g., laser spot size, nozzle diameter, degree of position controller handing), as well as material constraints (e.g., particle size of powders)[9].

**Biomaterials.** Composite materials often improve the mechanical properties of bulk material so functional materials are mixed with basic bulk materials in that mechanical properties and biodegradability of the scaffold is better controlled. Typically, the selected fabrication process determines the choice of applicable materials. For example, nozzle-based techniques are limited to synthetic polymers because of the high temperatures involved. Printing-based processes, such as 3D printing, use mainly PLA, PGA, and PLGA as basic building materials and chloroform as a binding solution. The use of organic solvents is a problem with this method. For photopolymerization, the selection of precursor solution is limited to materials that can undergo UV polymerization (e.g. hydrogels) and so on[9].

**Applications.** Computer-assisted fabrication methods have been used to study pore geometry and architecture influences on dynamic mechanical properties. Moroni et al. [24] demonstrated that elastic properties of scaffolds could be modulated using internal structure design. They used FDM to build scaffolds in which pores were varied in size and shape, by changing fiber diameter, spacing and orientation, and layer thickness. They observed that, with greater porosity, elastic properties (dynamic stiffness and equilibrium modulus) decreased, while viscous parameters (damping factor and creep unrecovered strain) were increased [6,24].

The most promising clinical application of SFF scaffolds is bone and cartilage tissue engineering, because mechanical integrity and anatomical shape are especially important with these tissues, even more in a in vivo application. Keriquel et al. [28] reported the in situ printing of a bone substitute consisting of mesenchymal stromal cells, associated with collagen and nano-hydroxyapatite, in order to favor bone regeneration, in a calvaria defect

model in mice. Thanks to the printing resolution and precision of laser assisted bioprinting (LAB) the group showed that, although with some variability, this approach could improve bone regeneration, while not inducing a deleterious effect on the adjacent brain tissue.

**Modifications.** With most scaffolds, the seeding process after fabrication can lead to limited 3D cell distribution and depth. Three-dimensional cell printing is an interesting derivation of the SFF process in that a cell suspension is mixed into in situ cross-linkable hydrogels (e.g., gelatin, agarose, alginate gel) in a cartridge and then printed following a programmed 3D pattern. This technique is also known as Microextrusion Bioprinting. As a result, a 3D cell–matrix hybrid structure is constructed that can potentially accelerate the organization of cells into a functional tissue combining the advantages mentioned in the cell entrapment technique with the computer-assisted fabrication pros.

Although all the fabrication methods have unique advantages, there is no one standard or superior fabrication process. In the current study we justify the application computer-assisted fabrication technique in combination with the cell-entrapment method to obtain a 3D cell-matrix hybrid structure as it allows to harness the advantages of both fabrication techniques. On one hand, cell-entrapment techniques have been used extensively in constructing 3D *in vitro* model systems because of distinct differences in cellular morphogenesis, function, migration, and differentiation from conventional 2D culture. On the other hand, an important potential for computer-assisted manufacturing that sets it apart from other manufacturing techniques is the ability to construct matrices with specific macro-scale architecture. Still, the ability to build a matrix layer by layer in any 3D configuration is limited in many manufacturing techniques but, a support bath material can be displayed, which allows building in any direction and fabricating almost any shape matrix.

The capability of large-scale manufacturing of consistent micro-scale 3D structure is another compelling advantage of the 3D printing technique. Computer instructed scaffold manufacturing processes can remove scaffold-to-scaffold variability and standardize *in vitro* models in a time effective and economical way.

#### 1.5.2.4 Extrusion Bioprinting

The fusion of these two techniques (computer assisted fabrication and cell entrapment) is known as **Microextrusion bioprinting**. It is one of the most promising biofabrication technologies nowadays due to its unique characteristics of high-throughput efficiency, cost effectiveness and full automation. This technique takes digital data from a computer and reproduces it layer-by-layer by extrusion of continuous filaments (direct write system) or droplets on previously printed successive layers.

It is possible to print only low viscosity systems:

- Cell beads in a polymer solution becoming hydrogel post printing (embedding cells),
- Cell beads without hydrogel in suspension.

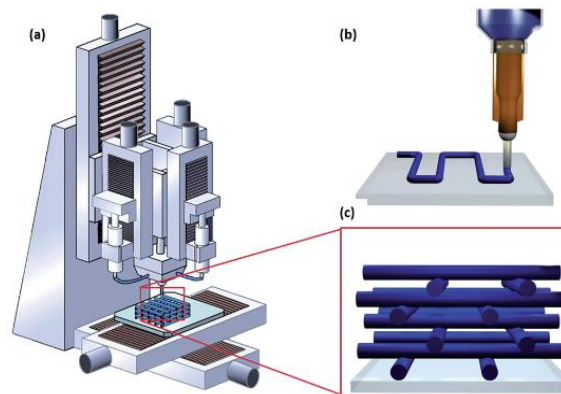


Figure 1.3 Microextrusion bioprinting [29].

Advantages:

- Low cost,
- Fast (< 10000 droplets/s),
- Versatile (suspensions of cells, biomolecules, growth factors).

Disadvantages:

- High shear stress due to small orifices (low viscosity materials are thus employed to avoid excessive stresses to the cells),
- Due to small size of the orifice, it is not possible to print high cell density.

Other considerations:

Generally, nozzle size is 30-200 $\mu\text{m}$ , leading to a resolution of around 85-300  $\mu\text{m}$ ;  
Ejected drop volumes are around 0.015  $\mu\text{L}$  per nozzle [30].

A particular challenge for the application of cell-laden hydrogels in extrusion bioprinting is to find a suitable concentration that can meet the processing conditions for accurate printing and also support cell viability and function. Often these criteria impose opposing requirements. Printing fidelity generally increases with polymer concentrations and cross-link density, whereas high polymer concentration limits cell migration and proliferation and subsequent ECM formation [31].

## 1.6 Scientific Background

### 1.6.1 *Hydrogels*

#### 1.6.1.1 Definition and properties

Hydrogels are polymeric networks that absorb large amounts of water without solubilizing and preserving their characteristic 3D structure [32]. The biocompatibility of hydrogels is determined by their hydrophilicity, which make them attractive for the design and fabrication of tissue constructs within cell encapsulation strategies.

Can be classified as either physical or chemical gel, depending on the nature of the network or based on their origin, as either naturally derived, are often ECM constituents, or synthetic, made in laboratory.

Specifically, biological hydrogels composed of polysaccharides and/or proteins are a class of materials that are challenging to 3D print because they must first be gelled in situ during the fabrication process and, simultaneously, supported so that they do not collapse or deform under their own weight. This gelation typically occurs through cross-linking reaction, initiated either by light (photosensitive), by a chemical, by hydrophobic or complexation interactions (ionic), or by a thermal transition (thermosensitive) [32]. For these soft biological hydrogels there is a narrow range of thermal, mechanical, and chemical conditions that must be ensure to prevent damage to the materials and potentially integrated cells [31].

#### 1.6.1.2 Cross-Linking Mechanisms of Hydrogels

Hydrogel polymerization can occur via physical, chemical, or combinatorial processes. Physical cross-linking mechanism is a nonchemical reversible interaction (ex.: ionic cross-linking by adding di/trivalent cations or printed thermosensitive polymers rapidly form a gel by changing the temperature), whereas, chemical cross-linking is usually achieved with gel precursors, such as monomers and an initiator, or UV-light exposure[32].

Collagen can be used for bioprinting by utilizing its physical gelation properties subsequently presented.

### 1.6.2 *Collagen*

#### 1.6.2.1 Definition and structure

Collagen is the most abundant protein in mammalian extracellular matrix where it is present primarily as fibrils, organized differently in different tissues. Collagen fibers not only impart mechanical strength to the tissue but also interact with cells through cell surface receptors and soluble proteins, which is integral to cell proliferation, migration, survival, attachment and cellular differentiation [33].

The current model of the basic unit of collagen (the “tropocollagen” molecule – Figure 1.4) consists of a helical quaternary structure called triple helix, which is composed of three left-handed alpha helices. In the collagen type I isoform, two of the chains are identical and the third has a similar but distinct sequence. The alpha chains are composed of the repeating structure Gly-Xaa-Yaa, in which Xaa and Yaa can be any amino acid but are frequently the amino acids proline and hydroxyproline and glycine at every third interval. Glycine is the smallest essential amino acid, and its presence in the chain allows the rotational freedom needed to form a helical structure. Inter-chain covalent and hydrogen bonding between the residues of these amino acids imparts stability and rigidity to the molecule [34].

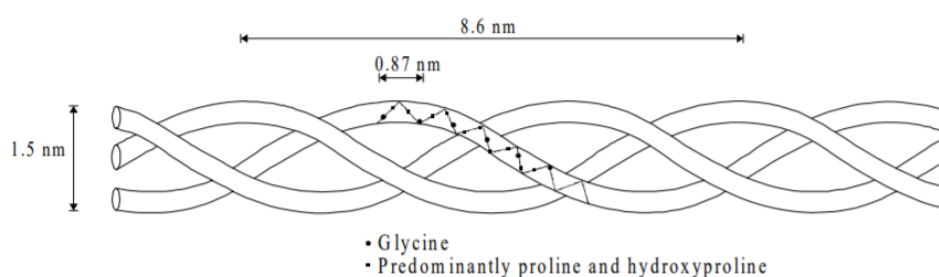


Figure 1.4 The collagen triple-helix.

An important characteristic of collagen type I is its well understood hierarchical structure from the nanoscale to the macroscale, shown schematically in Figure 1.5. Cells internally synthesize, modify, and assemble the alpha chains into a procollagen form, which is secreted to the extracellular space and then partially cleaved by specific enzymes to form the tropocollagen molecule. These nanoscale subunits (typically about 1.5 nm in diameter and 300 nm in length) further self-assemble into fibrils that consist of multiple tropocollagen molecules, which can be tens to hundreds of nanometers in diameter and on the order of microns in length. The tropocollagen molecules are covalently bound to each other in a staggered manner, giving collagen fibrils a distinctive banded pattern when viewed at high magnification. Fibrils can then assemble into larger and longer fibers and fiber bundles on the order of microns to centimeters in scale, and such fibers are major structural components of many tissues. The intricate and highly organized architecture of collagen materials, from the level of alpha helices to fiber bundles, results in a stable extracellular matrix protein with high tensile strength [34].

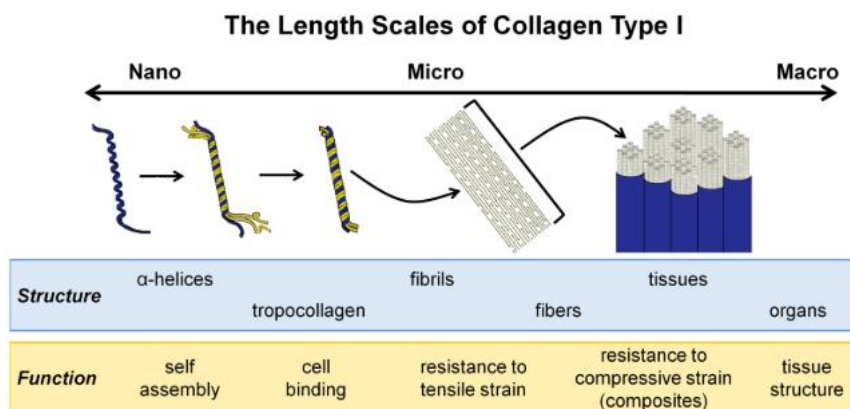


Figure 1.5 The hierarchical structure of collagen type I [34].

### 1.6.2.2 Properties: fibrillogenesis

Collagen fibril formation is a multiple step process which involves molecular packing into an ordered structure. Its ability to self-assemble *in vitro* to form insoluble fibrils, make collagen a useful and versatile material for tissue-engineered scaffolds [35]. Both *in vivo* and *in vitro*, collagen I monomers self-assemble into fibrillar structures that may cross-link and/or entangle to form viscoelastic gels with varied network structures and mechanical properties. *In vitro*, network structural and mechanical properties can be tuned through introducing cross-linkers and secondary gel components, as well as through varying temperature, pH, and ionic strength during self-assembly. Collagen network properties are sensitive to these factors because these conditions affect the self-assembly of collagen monomers into fibrils, process known as collagen fibrillogenesis [33].

Figure 1.6 shows that it is possible to induce fibrils formation from monomeric solutions in two ways. The first is to take a solution of collagen molecules and by changing the pH at a certain temperature and ionic strength, a rigid, three-dimensional gel network will be formed. The second way, consist on taking a cold neutral solution of soluble collagen molecules and raise the temperature, after a delay of some period of time, a fibrous precipitate forms showing an increase in the optical density [36].

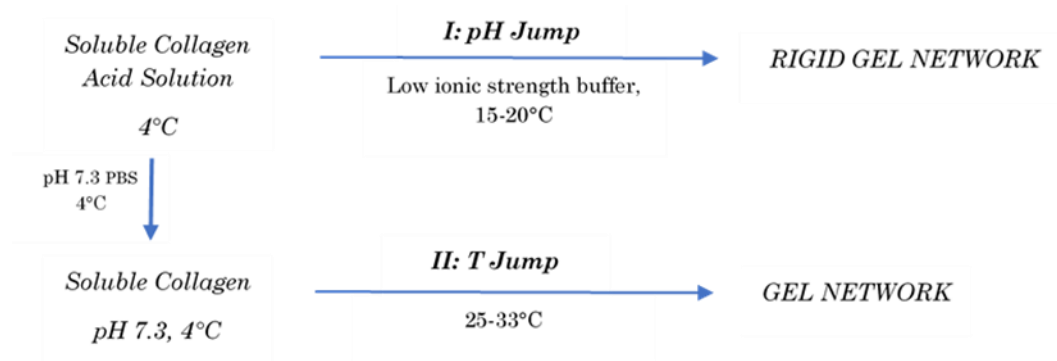


Figure 1.6 Routes for the *in vitro* production of collagen fibers from solution [36].

Fibrillogenesis is a thermally driven process which is favored by hydrophobic interactions. Hydrophobic interactions between non-polar regions of adjacent molecules are the predominant effect governing collagen fibril formation due to the negative temperature coefficient of collagen. When the pH approaches the pI (isoelectric point), the surface charge of the collagen monomers is reduced, which would minimize the electrostatic repulsion and favor collagen molecule aggregation. It has also been reported that the collagen fibrillogenesis is driven by hydrogen bonding between polar residues through direct measurement of forces between collagen molecules. Ionized residues along the collagen regulate the stability of the collagen triple-helix. Charges on ionizable groups, whose charging is pH-dependent, take part in electrostatic interactions leading to the fact that the pH of the medium affects the stability of collagen fibrils. Also, salts which bind to the collagen might also affect the electrostatic interactions. A strong influence of the ion species on the surface charge on collagen was found in the zeta potential measurement carried out by Li et al. [35] in their study of collagen fibrillogenesis *in vitro*. They observed a shift in the pI that might be the result of preferential adsorption of phosphate ions.

### 1.6.2.3 Collagen: Animal Sources and Biomedical Application

In the present study a brief description of collagen will be given including its characteristics, source and application in various fields, with the aim of summing up the work performed to date by different groups of scientists.

#### **Collagen types**

At least 28 different collagens have been identified in vertebrates. All of them have a characteristic triple helix but the length of the helix and the size and nature of non-helical portion varies from one to another type. Among these, the 5 most common ones are:

- Collagen I: Skin, bone, teeth, tendon, ligament, vascular ligature, organs (main constituent of the organic part of bone).
- Collagen II: Eyes and cartilage (main constituent of cartilage).
- Collagen III: Reticulate (main constituent of reticular fibers), skin, muscle, blood vessels.
- Collagen IV: Forms the epithelium-secreted layer of the basement membrane and the basal lamina.
- Collagen V: Hair, cell surfaces and placenta.

90% of the collagen in the body is of type I due to its wide prevalence in almost all connective tissues, followed by type II and III [37]. We will focus the review on type I collagen since is the main component used as the basic matrix for the lung tissue model carried out in this work.

#### **Collagen sources from animals**

The principal sources of collagen reported for biomedical applications are cow hide, pig intestines and skin, bovine tendon, rat tail and fish skin, with techniques used to obtain their solutions of collagen including acidic environments or neutral salt solutions [38].

**Bovine:** It is one of the major industrial sources of collagen. It makes use of the skin, tendon and bone of cow. Type I collagen is industrially obtained from Bovine Achilles tendon. Due to the outbreak of diseases such as Transmissible Spongiform Encephalopathies (TSE) especially mad cow disease, which suppose a threat to the humans, researchers are in search for an alternative safer source of collagen. Another drawback is that nearly 3% of the population is allergic to bovine collagen, causing an impediment in its usage [37].

**Porcine:** Obtained from pig's skin, tendons and bones. Since porcine collagen is almost similar to human collagen it does not cause much allergic response when used. But just like the bovine source the setback of possible transmission of animal diseases poses a risk for the humans and pigs are forbidden due to religious constrains.

Collagen extraction from animal source (bovine and porcine source) is complex, time consuming and expensive. The yield obtained is also lower when compared to other sources (approximately 12 g of collagen per 1kg of the raw material used) [37].

**Marine:** This source includes the use of marine invertebrates and vertebrates such as fishes, star fish, jellyfish, sponges, sea urchin, octopus, squid, cuttlefish, sea anemone and prawn. Due to the concern over adverse inflammatory and immunologic response and prevalence of various diseases among land animals, marine sources have started to be researched. Marine source is found to be the safest source for obtaining collagen presently.

Advantages of marine source over the land animal are:

- Free of zoonosis such as TSE among others
- High content of collagen
- Environment friendly
- Greater absorption due to low molecular weight
- Less significant religious and ethical constraints
- Minor regulatory and quality control problems
- Presence of biological contaminants and toxins almost negligible
- Low inflammatory response
- Less immunogenic
- Metabolically compatible

Collagen mainly type I was obtained from the skin of silver carp, bullhead shark and sole fish; and bone of thunnus obesus, skipjack tuna, carp among others [37].

**Other animal sources:** It includes chicken, kangaroo tail, rat tail tendon, duck feet, equine tendon (horse), alligators' bone and skin, birds' feet, sheep skin (ovine source), frog skin and sometimes even from humans. Recombinant human collagen is used which lower immunogenicity compared to other sources.

## Cases of study

### 1.6.2.3.1 BOVINE COLLAGEN

**Case of study:** "Development of 3D printed fibrillar collagen scaffold for tissue engineering", by Aden Díaz Nocera, Romina Comín, Nancy Alicia Salvatierra & Mariana Paula Cid [38].

They isolated collagen from bovine Achilles tendon and examined the purity of the isolated collagen. After designing and fabricating a low-cost 3D printer, collagen printing was assayed, obtaining 3D printed scaffolds of collagen at pH 7. Overall, their results show the capability of the presented protocol to obtain printable fibrillar collagen at pH 7, structures which maintained the fibrillar collagen structure after incubation in culture media without using additional strategies as crosslinking. Finally, the cytocompatibility of the scaffolds was assayed.

### Protocol

**Collagen Solution:** A gel-like consistency was reached by hydrating 60 mg lyophilized collagen with 1 ml of PBS at pH 7.

**3D printing:** A 21G needle ( $0.517 \pm 0.019$  mm inner diameter) was used and a resolution of 500  $\mu\text{m}$  on the X and Y axes, and 1 mm on the Z axis were used. Due to the high viscosity of the collagen gel, a delay time of 300 ms was applied after each material deposition, which prevented the printing head from moving to the next position before having deposited the required amount of material.

Each scaffold was constructed by four layers -of about 1 mm thickness- in a  $4 \times 6$  mm square. The printing was carried out at room temperature. After printing, the scaffolds were covered with ethanol 70% to sterilize the printed structures.

### Results

Characterization of 3D printed collagen scaffold:

They obtained collagen 3D printed scaffolds using a concentrated dispersion of isolated collagen (60 mg/ml in PBS at pH 7), higher than others reported ([39],[40]), an ink which permitted homogeneous extrusion of the material through a needle with an inner diameter of 516  $\mu\text{m}$  and deposition at room temperature. They associate the feasibility of obtaining collagen printable scaffolds not just to the high concentration of the bio-ink but also, to the source and extraction method used to obtain type I collagen. They argue that, fibrillar structures that consist primarily of type I collagen, such as those from tendon, appear to have distinct structural features. Zeugolis et al. [41] shown that bovine tendon derived fibers demonstrated higher denaturation temperature than the rat tendon derived ones; possibly attributed to higher amount of crosslinks. The collagen fibrillar structure of the bovine tendon could explain the printing and thermal stability of their collagen scaffolds without crosslinking compared to others reports.

SEM images showed that the scaffolds presented highly interconnective **pores of sizes** between 50 and 500  $\mu\text{m}$ , adequate for neovascularization and cell penetration [42]; and micropores with diameters lower than 10  $\mu\text{m}$ , necessary for cell attachment and mobility [43]. The macropores crossing the whole construct only were fabricated in its lateral sides because the strands fused with the ones on the bottom and with the ones on the side to form a block during printing process.

The **porosity ratio** of the collagen 3D printed scaffold was  $90.22\% \pm 0.88\%$ , thus scaffolds may achieve neovascularization and cellular infiltration[42]; and the **swelling ratio** was  $1437\% \pm 156\%$ .

Cytotoxicity analysis (based on ISO 10993):

Collagen scaffold extracts were evaluated to assess cytotoxicity in two cell lines after 24h incubation. The Vero and NIH 3 T3 cells viabilities were at least 70% in all cases, thereby indicating a lack of toxicity in the extract composite to these cell lines (ISO 10993–5, recommends cell viability to be greater than 70%).

Cytocompatibility:

Fluorescence images by DAPI staining showed that NIH 3 T3 and Vero cells were able to attach and proliferate on the collagen scaffolds, showing an increase in the number of cells attached to scaffolds along with culture time. In the cross-section histological cuts, cells seemed to be concentrated at the edges of the constructs, suggesting that they cannot penetrate to the center of the construct.

SEM pictures show that the fibrillar collagen structure of the construct could be maintained *in vitro* after 7, 10 or 14 days of incubation at 37 °C. Once the cells adhered to the substrate, they began to respond to this by changing their morphology, growth, proliferation, differentiation pattern and behavior.

**Future:** In vivo studies are still necessary of 3D printing collagen scaffolds in which the neovascularization, immune response, recellularization, and biodegradability are evaluated. Mechanical studies were not performed.

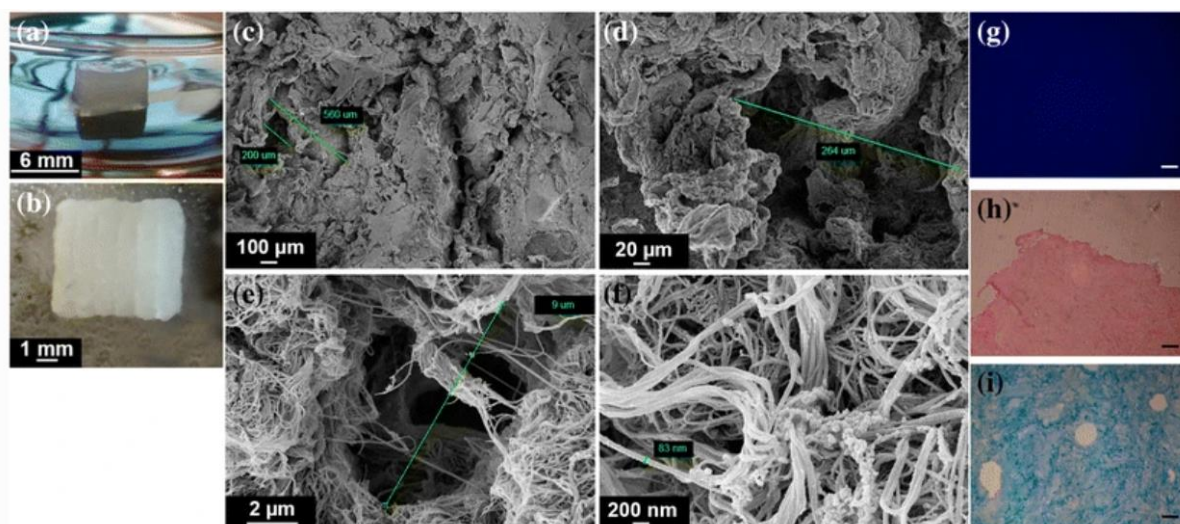


Figure 1.7 Characterization of 3D printed collagen scaffold. a-b Macroscopic shape of 3D–printed collagen scaffold. c-f SEM representative microphotographs of 3D–printed collagen scaffolds at different magnifications. g Representative image of DAPI staining from 3D–printed collagen scaffolds; h Representative image of H&E; i Masson stains from cross sections of 3D–printed collagen scaffolds. Scale bar is 100  $\mu\text{m}$  (g,h,i) [38].

### 1.6.2.3.2 PORCINE COLLAGEN

**1st Case of study:** “Strategy to Achieve Highly Porous/Biocompatible Macroscale Cell Blocks, Using a Collagen/Genipin-bioink and an Optimal 3D Printing” by Yong Bok Kim, Hyeongjin Lee, and Geun Hyung Kim [44].

They propose a printing strategy for obtaining a 3D porous cell block composed of a biocompatible collagen-bioink and genipin, a natural cross-linking agent. To show the feasibility of the process, cell-laden constructs were manufactured using osteoblast-like cells (MG63) and human adipose stem cells (hASCs).

#### Protocol

**Collagen Solution (bioink):** type-I collagen (Matrixen-PSP; SKBioland, South Korea) derived from porcine tendon was used. To make a neutral collagen solution, 10× enriched DMEM solution was mixed with the collagen solution at a volume ratio of 1:1. The neutralized weight portions (3, 5, and 7 wt %) of collagen were used in this cell-printing process, and the mixture of cells ( $1 \times 10^6$  cells mL<sup>-1</sup> for MG63s and hASCs) and collagen solutions was utilized as a collagen bioink.

**Cross-linking method (Genipin):** For the cross-linking of the printed cell laden collagen structures, they were incubated in 0.1, 0.5, 1, 3, and 5 mM genipin solution (Challenge Bioproducts, Taiwan) in medium for 1, 6, 24, and 48 h.

**3D printing:** a printing nozzle (outer diameter of 310 μm) was used to obtain a multilayered mesh structure and the temperature of the barrel/nozzle and working stage both precisely controlled at 10°C and 35°C, respectively. Pneumatic pressure was applied in the range of 110–300 kPa in the microsize nozzle. The speed of the moving nozzle was fixed at 10 mm s<sup>-1</sup> and a mass flow rate between 1.52–1.62 mg/s. A mesh structure (a 0°/90° strut structure) was obtained using a layer-by-layer manner.

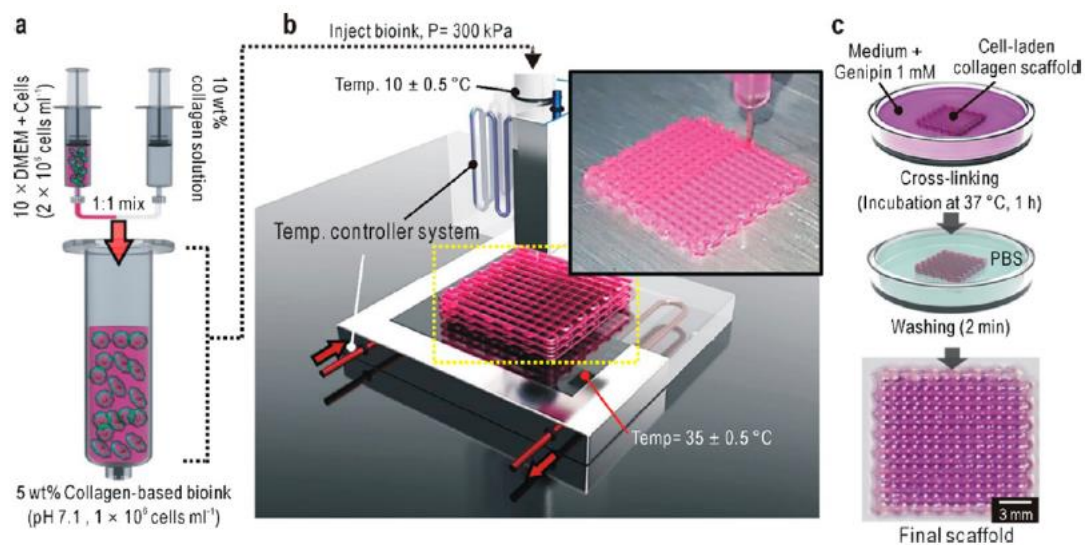


Figure 1.8 Scheme of procedure for fabricating cell-laden collagen-mesh structure. (a) Collagen bioink mixed with culture medium, (b) 3D printing system supplemented with temperature controllers, and (c) cross linking with genipin and washing [44].

## Results

Viscoelastic properties - rheological behavior:

3, 5, and 7 wt % of cell (MG63 density =  $1 \times 10^6$  cells mL<sup>-1</sup>)-laden collagen, were used to measured storage modulus ( $G'$ ) and tangent delta ( $\tan \delta$ ). Based on the rheological assessment results, it was possible to select a reasonable weight fraction of collagen in the bioink and a processing temperature in the nozzle that resulted in high cell viability (93% in a 5 wt % collagen concentration used in the in the subsequent experiments).

The temperature of the working plate was gelation temperature (35°C). 10 °C in the barrel/nozzle resulted in relatively stable formation of the porous structure until 1.2 mm thickness compared to the others. The most appropriate thickness having homogeneous pore size in the cell-laden structure was about 4 mm using the gelation temperature.

Optimal Concentration of Genipin for Cross-Linking - As expected, as the genipin concentration and crosslinking time increased, the qualitative stiffness of the mesh structure continuously improved, and also the blue color of the cross-linked structure became denser because of the increased fluorescence intensity (emission at 630 nm) induced by genipin cross linking. Viabilities of the collagen structures exposed to the genipin solutions of 0.1, 0.5, and 1 mM for 48 h were relatively high for osteoblast-like cells, fibroblasts and human adipose stem cells.

To achieve the macroscale cell-laden structure, by using several steps and one protruding structure like a brick unit of LEGO blocks was attained, successfully achieving a highly porous (**pore size** = over 400  $\mu$ m)/mechanically stable and biocompatible cell-laden collagen block of  $21 \times 21 \times 12$  mm<sup>3</sup> (Figure 1.9)

## Cytocompatibility:

The *in vitro* assessment of in situ cell viability, live/dead, and DAPI/phalloidin staining outcomes for several culture periods of the 3D porous cell block showed that the osteoblast-like cells and hASCs were sufficiently viable without damage during the printing and cross-linking processes.

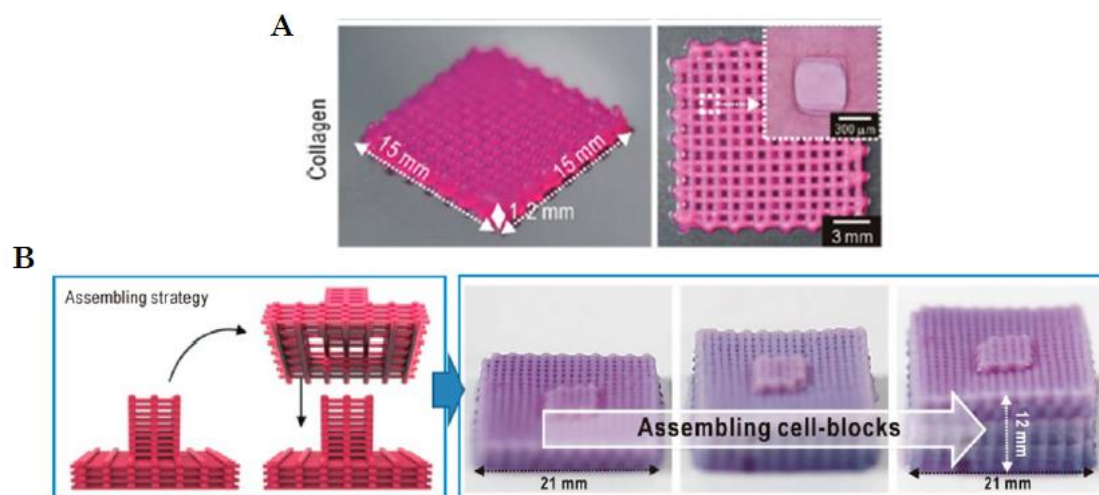


Figure 1.9 A- Optical images of 3D mesh structures printed using MG63-laden collagen bioink. B- Assembling method and an assembled macroscale rectangular cell-laden structure ( $21 \times 21 \times 12$  mm<sup>3</sup>) [44].

**2nd Case of study:** “A cell-printing approach for obtaining hASC-laden scaffolds by using a collagen/polyphenol bioink”, by Myung Gu Yeo and Geun Hyung Kim [39].

They proposed a collagen bioink, which was mixed with human adipose stem cells (hASCs) and crosslinked with a polyphenol (tannic acid (TA)), a natural cross-linking agent. The feasibility of the bioink was demonstrated using several *in vitro* assessments for comparison of the macroscale porous cell-laden collagen/polyphenol structure containing the hASCs with the control (alginate-based cell-laden structure). The levels of the metabolic activity, including the cell viability and cell proliferation, of the cell-laden collagen structure were significantly higher than those of the control.

### Protocol

**Collagen Solution (bioink + TA):** In this work, human adipose-derived stem cells (hASCs) and type-I collagen from porcine tendon were used in the bioink. A fixed weight fraction (4wt%) of collagen was used in the printing process; the collagen was mixed with the cell density ( $2 \times 10^6$  cells  $\text{ml}^{-1}$ ). The solution was mixed with TA solution (1–6 wt% in phosphate buffered saline solution (PBS)) in a 4:1 volume ratio.

**3D printing:** A dispensing system with a nozzle (outer diameter = 310  $\mu\text{m}$ ) was used. In the system, the temperature of the both the barrel/nozzle and working stage was set at 30 °C. The applied pneumatic pressure in the barrel/nozzle was in the range of 140–600 kPa. The moving speed of the nozzle was  $5\text{mm s}^{-1}$ . After fabricating the cell-laden mesh structure, it was immersed in  $\alpha$ -MEM medium and washed in PBS solution.

### Results

Viscoelastic properties - tube inverting test (qualitative):

Qualitatively the viscosity was evaluated of both, pure collagen (4wt%) and the mixtures of collagen with various weight fractions of TA (1–6wt%) after mixing for 1 h. Pure collagen instantaneously flowed out, whereas the mixtures did not easily flow. Physical non-flow phenomenon was due to the crosslinking of collagen by the formation of multiple hydrogen bonds between collagen and TA.

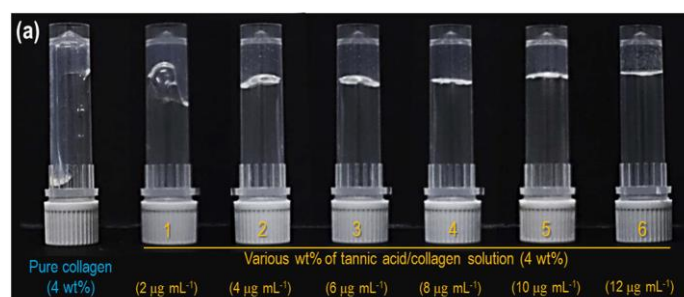


Figure 1.10 Optical images demonstrating the viscosity of pure collagen and the mixtures of collagen/various weight fractions of TA after mixing for 1 h.

Viscoelastic properties - rheological behavior (quantitative):

Storage modulus ( $G'$ ), and tangent delta ( $\tan \delta$ ) of the mixtures were analyzed using time and temperature sweep. With an increase of the weight fraction of the TA in the collagen/TA mixture, the  $G'$  value of the mixture gradually increased. The time dependent modulus level ( $G'$ ) of the collagen/TA, showed that with an increase of the weight fraction of the cross-linking agent, less cross-linking time was required. From the results, it is possible to set the crosslinking time for each mixture of collagen/TA. Based on the viscoelastic properties of the collagen/TA mixtures, the temperature for stable processing of the cell-laden collagen crosslinked with TA was about 30 °C, and the time for stable cross-linking of collagen/TA should be over 30 min.

Cytotoxicity:

The range of 1–3 wt% TA was a relatively safe range (cell viability  $\geq 90\%$ ) for the hASCs.

Printability and Cytotoxicity:

The diameter distribution of the strut for the CT-2 (2wt% TA) and CT-3 (3wt% TA) samples was significantly constant compared to that of CT-1 (1wt% TA). Based on the results of the in-situ cell viability analyses, the optimal concentration of TA for crosslinking is 2 wt% ( $2 \mu\text{g ml}^{-1}$ ). CT-2 fabricated scaffold shows a **pore size** resolution about  $49 \pm 30 \mu\text{m}$  (smallest) and  $635 \pm 43 \mu\text{m}$  (largest).

Mechanical properties:

The compression test was conducted in the wet state, results depicted in Figure 1.11.

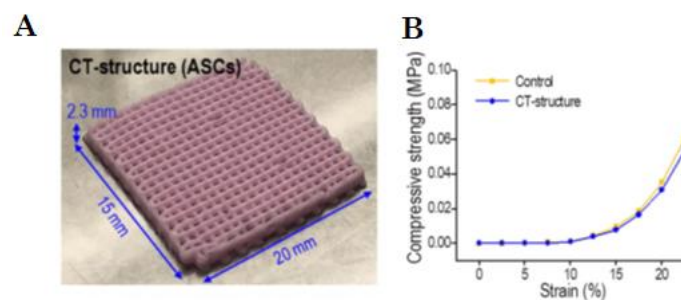


Figure 1.11 A- hASC-laden collagen-TA bioink (CT-structure). B- Compressive stress–strain curves and strengths at 5% and 10% strain. Control: alginate bioink [38].

Cytocompatibility:

Analysis of the live/dead cells and DAPI/phalloidin images of the 3D porous mesh structures demonstrated that the hASCs were not damaged by the wall shear stress applied by the pneumatic pressure in the extrusion process, and the embedded cells were well migrated/proliferated for long culture periods (10 to 35 days tested) due to the safely cross-linked collagen and its biocompatible components (e.g., RGD sequences) compared to the control (alginate based cell-laden structure).

**3rd case of study:** “Viscoll collagen solution as a novel bioink for direct 3D bioprinting”, by Egor O. Osidak et. al [45].

In the study was showed that concentrated solutions of collagen branded Viscoll were effective as bioinks with high fidelity performance. Collagen Viscoll represents a smoothly soluble collagen fraction sterilized by filtration and obtained by acidic extraction from animal tendons, followed by purification with different salt precipitation and ion-exchange chromatography. Viscoll containing 20, 30, or 40 mg/ml collagen were used for direct extrusion 3D bioprinting to form scaffolds appropriate to support spatial arrangement of tissue spheroids into rigid patterns. Incorporated cells demonstrated sufficient viability.

### Protocol

**Collagen Solution:** Lyophilized sterile collagen Viscoll (Viscoll, Imtek Ltd., Russia) was reconstituted in 20mM acetic acid to a stock concentrations 40, 60 and 80 mg/ml and packed in individual syringes with a luer-lock connection. The dilution and neutralization of collagen solutions were made at +4°C as follows: (1) A syringe with the culture medium (DMEM, 10% fetal bovine serum, 100mM Tris-HCl) was hermetically coupled with a syringe containing equal volume of Viscoll collagen. (2) The collagen solution was carefully mixed with the culture medium, resulting in neutralized homogenous 20, 30, and 40 mg/ml collagen solution. For bioprinting of cell-laden 3D constructs, the neutralized Viscoll collagen solution was mixed just before use with the culture medium containing the cells in 9:1 ratio, the result cell density in the collagen solutions was  $0.5 \times 10^6 \text{ ml}^{-1}$ .

**3D printing:** plastic needle with inner diameter 250  $\mu\text{m}$ . The temperature of Viscoll collagen in syringes was maintained 15 °C during the bioprinting process, while Petri dishes bottom was heated up to 37 °C. The bioink flow rate in experiments was 5 mm min<sup>-1</sup>.

### Results

Printability:

10 layer  $30 \times 30 \times 2$  mm meshes using 2%, 3% and 4% Viscoll bioinks were successfully bioprinted and from the dimension of 3D printed cubes a comparison with digital calculations of bulk volume revealed that cubes applying 15 mg/ml Viscoll bioink were generated with about 70% structural fidelity, 20, 30 and 40 mg/ml Viscoll bioink—with 80%, 83 and 85% fidelity respectively.

Viscoelastic properties:

The results showed the ability of Viscoll solution to maintain the predesigned shape once being extruded from the needle, avoiding immediate deformation and allowing subsequent polymerization at +37°C.

Mechanical properties:

The mechanical properties of the bioprinted  $6 \times 6 \times 6 \text{ mm}^3$  cubes consisting of 30 layers were analyzed and the compressive modulus of the constructs were:  $7.2 \pm 0.6 \text{ kPa}$ ,  $8.2 \pm 0.9 \text{ kPa}$ ,  $9.5 \pm 0.4 \text{ kPa}$  and  $21.5 \pm 1.4 \text{ kPa}$  when concentration of the collagen increased from 15 mg/ml to 20, 30, and 40 mg/ml, respectively.

Cytotoxicity:

The viability of NIH 3T3 cells inside the bioprinted constructs on 7th day in culture was  $97.2\% \pm 1.2\%$ ,  $95.2\% \pm 1.3\%$  and  $87.2\% \pm 2.1\%$  for Viscoll bioinks at 2%, 3 and 4% collagen concentrations respectively.

Cytocompatibility:

Spread cells was observed on 3rd day for all variants of Viscoll bioinks applied. Additionally, observed cell adhesion and proliferation confirmed good biocompatibility of the collagen bioink. Cell migration was more intense within constructs printed applying less concentrated Viscoll.

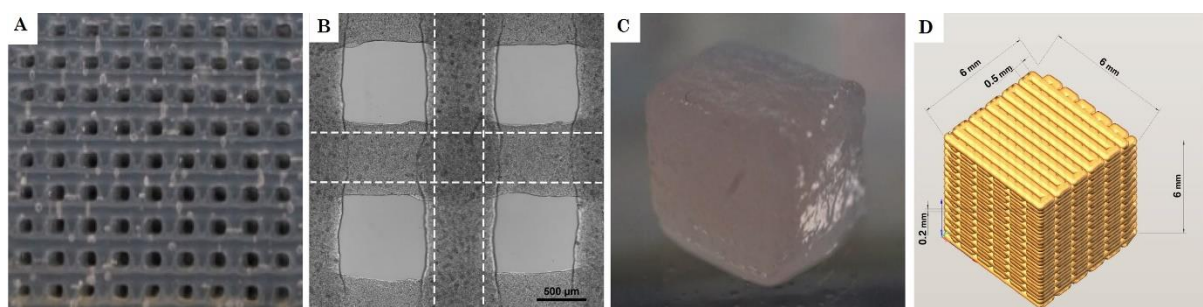


Figure 1.12 Direct bioprinting of a 3D scaffold using 30 mg/ml Viscoll collagen solution. A- B-Ten layer meshes bioprinted. C- Cube printed. D- CAD model of cube [45].

#### 1.6.2.3.3 MURINE COLLAGEN

**1st case of study:** “Design and Fabrication of Human Skin by Three-Dimensional Bioprinting”, by Vivian Lee, Gurtej Singh, John P. Trasatti, Chris Bjornsson, Xiawei Xu, Thanh Nga Tran, Seung-Schik Yoo, Guohao Dai and Pankaj Karande [40].

In this work, it is described the development, optimization, and application of a 3D cell and protein printing platform for the engineering of biological tissues and organs using human skin as a prototypical example. A multi-layered matrix structure was constructed in which human keratinocytes (KCs) were grown at the ALI on collagen matrices embedded with human dermal fibroblasts (FBs). They were able to effectively control the number of layers, the cell density, and their precise location in the generation of this skin model.

### Protocol

**Collagen Solution:** Collagen hydrogel precursor (Rat tail, type I; BD Biosciences) was used as a scaffold material for printing. The collagen precursor was diluted to 3.0mg/mL with 1 x Dulbecco's PBS and was maintained on ice until it was ready to be loaded into a syringe for printing.

**3D printing:** Before printing was initiated, nebulized sodium bicarbonate ( $\text{NaHCO}_3$ ) vapor was applied onto the petri dish surface, enabling the quick gelation of the first printed collagen layer and thereby increasing its adhesion to the bottom surface. Subsequent to the printing of the first collagen layer, nebulized  $\text{NaHCO}_3$  vapor was applied onto the printed collagen layer for gelation. To provide a firm base for the next layer of printing, a time lapse of one minute could facilitate the phase transition of collagen to a gel. Table 6 summarizes the printing parameters used for both collagen and cell suspension.

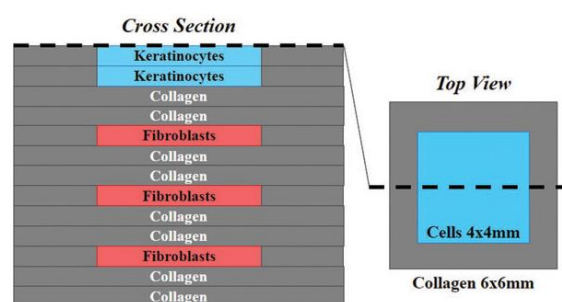


Figure 1.13 Schematic of the 3D printed skin tissue. Layer-by-layer printing of collagen matrix, KCs, and FBs to construct the dermal and epidermal compartments in a single structure. Cross-section (left) and top view (right) [40].

Printing parameters	Collagen	Cell suspension
Air pressure	2.5-2.7 psi	1.4-1.5 psi
Valve opening time (pulse duration)	750 $\mu\text{s}$	750 $\mu\text{s}$
Droplet volume	52.77 $\pm$ 3.81 nL	28.53 $\pm$ 3.15 nL
Droplet spacing (resolution)	500 $\mu\text{m}$	500 $\mu\text{m}$
Concentration/density	3.0 mg/mL	2 and 5 million cell/mL (FBs and KCs)

Table 6. Printing parameter of collagen-ink an cell suspension-bioink.

### Results

Printability and cytotoxicity:

Optimization of printing parameters for individual cell cultures was necessary, in terms of cell suspension density and resolution (spacing between droplets) resulting in 2 million FBs/mL and 5 million KCs/mL at 500  $\mu\text{m}$ , parameters that showed a cell viability of ~98%.

Cytotoxicity:

Viability for both cell types employed in this study, KCs and FBs, was sufficiently high (~95% or greater for a majority of conditions).

Cytocompatibility:

For both cell types employed in this study, KCs and FBs, it was possible to achieve uniform distribution of FBs in the dermal compartment and that of KCs in the epidermal compartment and formation of stratified layers after ALI culture (Figure 1.14 – C).

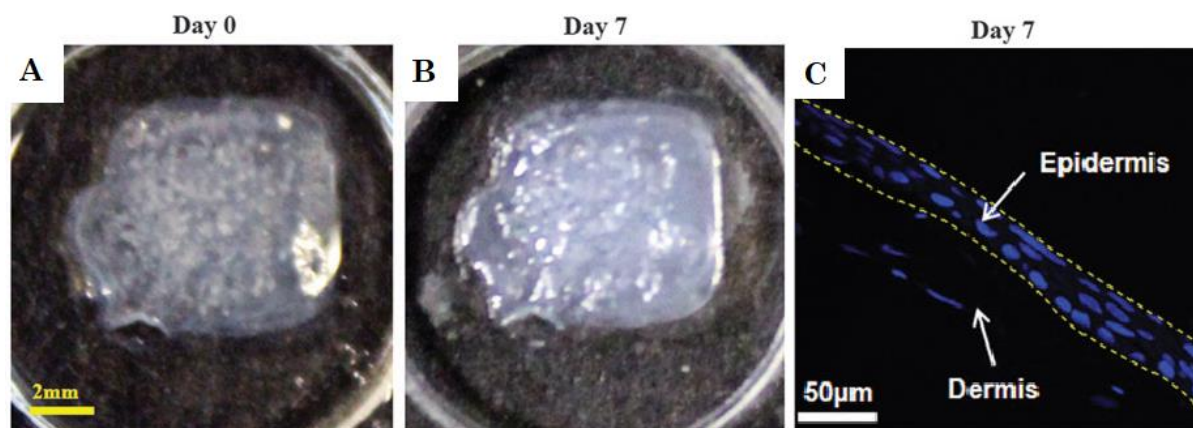


Figure 1.14 Printed skin samples 6x6 mm and the height of the printed skin structure varied from 1100 to 1400 mm. A,B- retain their form (dimensions) and shape, whereas manually deposited structures (images not showed) shrink and form concave shapes under submerged culture condition after 7 days. C- Histology of printed skin cultures using nuclear staining at day 7 [40].

**2nd case of study:** “Correlating rheological properties and printability of collagen bioinks: the effects of riboflavin photocrosslinking and pH”, by Nicole Diamantides et al. [46].

In this study, they investigated the effects of riboflavin photocrosslinking and pH on type I collagen bioink rheology before, during, and after gelation and directly correlated these findings to the printability of each bioink formulation.

### Protocol

**Collagen Solution:** After collagen extraction from tendons obtained from rat tails, collagen hydrogels were fabricated by mixing the stock collagen solution with a working solution of 1X phosphate buffered saline (PBS), 10X PBS and 1 N NaOH. All components were kept on ice before mixing. In the case of the riboflavin study, 2.0mM riboflavin in 1X PBS was added to the working solution to obtain a final riboflavin concentration of 0.5mM and final collagen concentration of 4, 8, or 12 mg/ml. In the pH study, the final collagen

concentration was 8 mg/ml and the volumes of 1X PBS and 1 N NaOH in the working solution were varied to achieve the desired final pH, which ranged from 6.1 to 10.1.

**3D printing:** The printer's platform was set at 37°C. 0.25-mm-diameter stainless steel needle was used on the end of the syringe. The bioink was exposed to blue light using a LED curing device (1200mW/cm<sup>2</sup>, Maxima RU1200 LED curing light, Henry Schein Inc., Melville, NY) for 10 s beginning at the onset of dispensing for each dot. Three different shapes were printed to assess shape fidelity and printability at varying pH levels. The taller one was a three-layer square 25.0 × 25.0 × 1.2mm<sup>3</sup>.

## Results

Viscoelastic properties:

As image A from Figure 1.15 illustrates, three phases were observed during rheological testing of collagen bioinks with riboflavin crosslinking: an initial plateau phase corresponding to the 30 s before UV exposure, a growth phase corresponding to the 10 s during UV exposure, and a final plateau phase corresponding to the 30 s after UV exposure. Samples without riboflavin did not experience a growth phase and the moduli remained constant for the entire test length. After exposure to UV light, samples containing riboflavin experienced a large increase in  $G'$ , while, the growth rate increased with increasing collagen concentration. UV light exposure caused a 12-fold increase in  $G'$  in 4mg/ml bionink. Increasing collagen concentration from 4 to 12 mg/ml led to an increase in  $G'$  before UV exposure from 0.5 to 8.6 Pa and that, in samples with riboflavin, the crossover time decreased from 5.75 to 1.75 s. But, the mechanical enhancement after UV exposure due to riboflavin crosslinking was less pronounced at higher collagen concentrations.

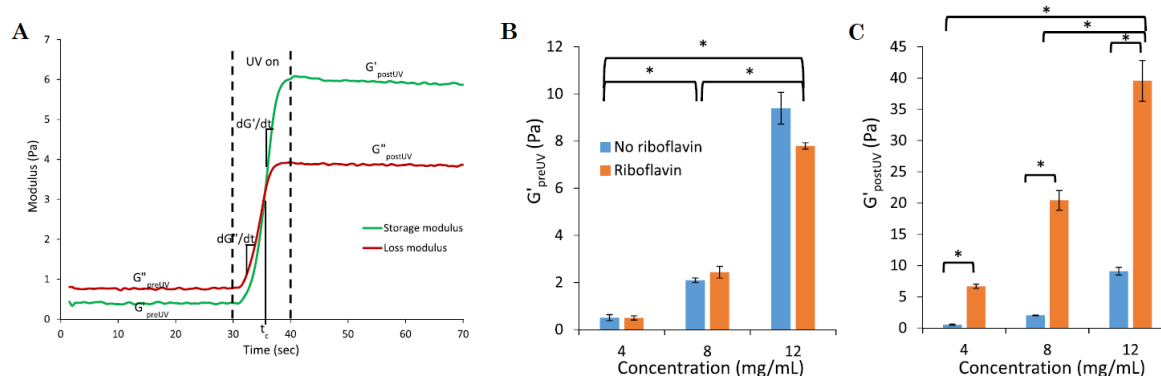


Figure 1.15 Rheological properties of collagen bioinks before, during, and after UV light exposure with and without riboflavin. A- Representative results of rheological testing of collagen bioink with riboflavin. B-  $G'$  of bioink before UV light exposure. C-  $G'$  of bioink after 10 s of UV light exposure [46].

Ph study: The results from the pH study show that the storage modulus after gelation and the growth rate of the storage modulus during gelation of collagen bioinks are highly dependent on pH. The average  $G'_{\infty}$  for the 7.5–8.0 and 8.0–8.5 pH ranges were more than 2 times greater than the  $G'_{\infty}$  of the control 7.0–7.5 pH range. The storage modulus of the bioink before gelation and the crossover time were found to vary little with pH.

Combining the findings of the riboflavin and pH studies, they found that the best way to improve the printability of collagen bioinks is to increase the storage modulus of the ink before extrusion.

Printability:

The addition of blue light activated riboflavin crosslinking was found to improve printability, resulting in a 10%–28% reduction in dot footprint area compared to samples without riboflavin. Higher collagen concentrations tended to result in smaller dot footprint areas.

Cytotoxicity:

Cell viability was high (>95%) at all collagen concentrations tested. However, the addition of blue light activated riboflavin crosslinking decreased viability to 76%–77%. Collagen concentration did not influence cell viability with or without riboflavin.

#### 1.6.2.3.4 Comparative table

For a comparative analysis of each case of study, a summarizing comparative table is presented (Table 7) for a better visualization of the collagen solution protocol, the printing parameters used for scaffold realization and relevant results of our interest for each case of study. Subsequently, in line with the need of identifying the optimum conditions that will let us build a robust 3D collagen-based construct, an analysis of each factor will be discussed in detail to reach a consistent conclusion. In Table 7 each review has been identified with a number from I to IV to facilitate its mention.

Collagen source:

Starting with the most widely used collagen source, they can be ranked as follows: rat tail, porcine tendon and finally bovine sources. A research work carried out by Zeugolis et al. [41] consisted on a comparison between collagen solutions of equal concentration derived from bovine Achilles tendon (BAT) and rat tail tendon (RTT), and extraction methods: acid (AS) and pepsin (PS) solubilization on the properties of extruded collagen fibers. The substructure of the collagen fibers was the same independent of the treatment, but when it comes to thermal response, BAT-derived fibers demonstrated higher denaturation temperature (not influenced by the extraction method). BAT-derived fibers also showed higher solution viscosity, related with the fact that relative amount of collagen types present is species and/or tissue dependent. The RTT is comprised almost entirely of type I (95%) with as little as 5% type III, while the BAT is composed of ~90% type I and 10% type III collagen. Another research work demonstrated that there are

subtle mechanical and enzymatic differences in scaffolds composed of bovine and porcine collagen-derived [47].

Up to now, there are limited numbers of comparative study on the species-related properties of type I collagen, so we can conclude that as no significance difference has been revealed between one or other source of collagen, it is correct to implement any of them, probably preferring a murine source, justifying this statement because of its highest relative composition of type I collagen (95%), meaningful for our application in lung tissue.

Collagen final concentration and crosslinking mechanism:

A wide range of collagen concentrations were used for the scaffold printing by the different investigation groups, between 2% and 12% wt, mostly for general TE applications or bone tissue application, whereas one group focused on soft tissue implementation (V-skin) and remained under 3% wt of collagen. Surprisingly, all of them obtained high viability and promising cytotoxicity results after cell culture analysis.

It has been extensively studied the effect of collagen concentration in the mechanical and biological properties of the scaffold, proving direct influence in cell motility, viability and growth. For example, Tierney et al. [46] studied the effects of varying collagen concentration (0.25%, 0.5% and 1% wt) revealing that the largest pore size, permeability rate, compressive modulus, cell number and cell metabolic activity (MC3T3-E1 mouse clonal pre-osteoblastic cells) was all found to occur on the 1% collagen scaffold due to its increased collagen composition. Moreover, Zhu et al. [47] studied how extracellular matrix concentrations can modulate fibroblast contraction of collagen gels affecting in cell viability; more contraction results from gels with lower initial collagen concentrations. The greater the degree of shrinkage, the greater the decrease in DNA content. This loss of cell number appeared to be due to apoptosis, suggesting that the release of mechanical tension is responsible for the induction of apoptosis. Once more, better results were obtained when increasing collagen composition. However, its augment is also associated with less cell motility and cell migration ([44], [48]), and with the increment on the stiffness of the material, limiting its application in soft tissue model. Osidak et. al [45] demonstrated the influence on collagen concentration in the scaffold stiffness (IV). This is a remarkable aspect to point out as we are focusing our implementation on lung tissue modeling, with the specific need of complying with the lung tissue mechanical properties.

Regarding the crosslinking approach faced by each group, all of them resulted in an improvement in printing fidelity during the process or once the printing model was synthesized, being the use of temperature and nebulized sodium bicarbonate ( $\text{NaHCO}_3$ ) vapor the simplest and most frequently techniques reported in literature.

### 3D Printer and printing parameters:

Each research group used different types of bioprinters, some of them developed their own low-cost bioprinters (I and V) and others used commercial ones: Dongbu Robot (II and III), Fabion bioprinter (IV) and Fab@Home 3D printer (VI), Figure 1.16. In 2015, 3Ders.org cataloged in order the 20 most promising 3D bioprinters, being Fabion bioprinter ranked in 5th place, while the other two technologies do not compare in the ranking. Besides, the printers used differ in the drive system, from stepper motors, to encoders, to servo motors.

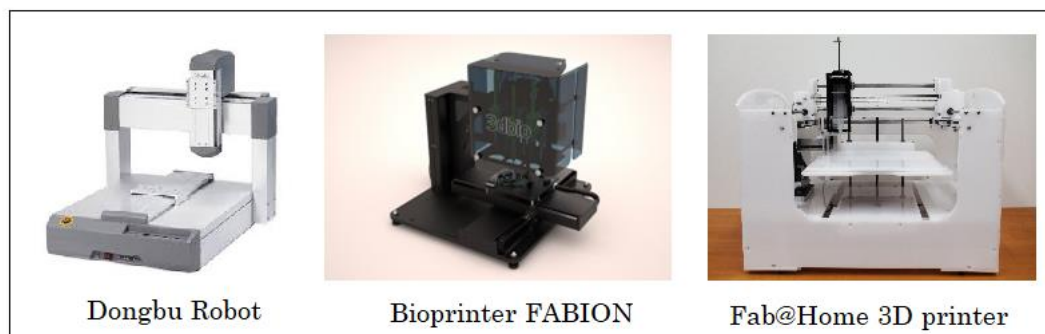


Figure 1.16 Commercial 3D printers used for printing 3D collagen-based scaffolds.

Even if the Dongbu Robot allowed the research groups to obtain robust scaffolds (2.3 to 4 mm height), we cannot associate the promising results to the 3D printer, since propitious results were also obtained within the other technologies.

Regarding the printing parameters, they varied from one printer to the other and even if, the same printer was used (II and III), the printing parameters differ because the hydrogel solution was diverse, so is not possible to standardize them. Depending on the printer technology and the collagen solution viscosity and composition, an optimization process of the printing parameters must be carried out definitely, with a trial-and-error approach.

In terms of the 3D printing technology available at the Polytechnic of Turin, we are well-positioned with both printers, the ROKIT Invivo (DIMEAS Laboratory), and the BioX Cellink (Polito BIO Med Laboratory). The Cellink Inkredible bioprinter was positioned in 9th place in the 3Ders.org ranking and, even if it is not the same device available at the Polytechnic, the BioX is a newest version developed following the Cellink Inkredible. Moreover, the ROKIT Invivo is in the 20th place on the 3Ders.org ranking of 2015 [48].

		I	II	III	IV	V	VI
Source		BOVINE (Tendon)	PORCINE (Tendon)	PORCINE (Tendon)	PORCINE (Tendon)	MURINE (Rat tail)	MURINE (Rat tail)
Work		Collagen scaffold, ph 7	Collagen-bioink scaffold + genipin bath	Collagen-bioink-TA scaffold	Collagen-bioink scaffold	Collagen-bioink scaffold	Collagen-bioink- riboflavin scaffold
Application		Scaffold for TE	Scaffold for TE (bone)	Scaffold for TE (bone)	Scaffold for TE	Skin	Scaffold for TE
PROTOCOL	Collagen (wt%)	6 wt%	5 wt%	4 wt%	2-3-4 wt%	3 wt%	4-8-12 wt%
	Crosslinking mechanism	Incubation	Genipin bath	Tannic Acid 2 wt%	Temperature	Nebulized (NaHCO <sub>3</sub> )	Riboflavin
	3D Printing	Needle $\theta_i=516\mu\text{m}$  $T^\circ = \text{room}$ temperature	Nozzle $\theta_o=310\mu\text{m}$ PnP=110-300 kPa Nozzle speed=10 mm/s Flow rate=1.52-1.62 mg/s Nozzle $T^\circ= 10^\circ\text{C}$ Bed $T^\circ= 35^\circ\text{C}$	Nozzle $\theta_o=310\mu\text{m}$ PnP=140-600 kPa Nozzle speed=5 mm/s Nozzle/Bed $T^\circ= 30^\circ\text{C}$	Nozzle $\theta_i=250\mu\text{m}$ Flow rate=5 mm/min Nozzle $T^\circ= 15^\circ\text{C}$ Bed $T^\circ= 37^\circ\text{C}$	Table N° 6	Nozzle $\theta=250\mu\text{m}$ Bed $T^\circ= 37^\circ\text{C}$
RESULTS	Dimension of the final construct	4×6×4 mm <sup>3</sup>	21×21×12mm <sup>3</sup>	20×15×2.3mm <sup>3</sup>	6×6×6 mm <sup>3</sup>	6×6×1.4mm <sup>3</sup>	25×25×1.2mm <sup>3</sup>
	Pore size resolution	10 – 500 $\mu\text{m}$	400 $\mu\text{m}$	49 ±30 - 635±43 $\mu\text{m}$	-	-	
	Porosity ratio	90.22% ± 0.88%					

		I	II	III	IV	V	VI
Source		BOVINE (Tendon)	PORCINE (Tendon)	PORCINE (Tendon)	PORCINE (Tendon)	MURINE (Rat tail)	MURINE (Rat tail)
	Rheological properties	-	Allowed to select a reasonable weight fraction of collagen in the bioink and a processing temperature in the nozzle	Allowed to set the crosslinking time for the mixture of collagen/TA (30min) and the T° for stable processing	Compressive modulus from 7.2 to 21.5 when the [collagen] increased from 15 to 40 mg/ml.	-	Large increase in G' and growth rate increased while crosslinking effect reduced with increasing [collagen]
	Cytotoxicity (cells viability)	≥ 70%	93%	≥ 90% Allowed to select the optimal concentration of TA	≥ 87.2%	~98%	76%–77%
	Cytocompatibility	Cells at the edges of the constructs they cannot penetrate to the center of the construct	The printed cells were proficiently distributed/proliferated on the cell embedded strut surface	Cells were well migrated/proliferated for long culture periods (35 d)	Spread cells at d 3. Cell adhesion and proliferation observed. More intense cell migration in less concentrated Viscoll constructs.	Uniform distribution of both cell types and formation of stratified layers after ALI culture	
Reference		[38]	[44]	[39]	[45]	[40]	[46]

Table 7. Comparative table about collagen: animal sources and biomedical application.  $\theta_i$  =inner diameter,  $\theta_o$ =outer diameter, PnP=Pneumatic pressure, dimension of the final construct = ((square) × thickness).

## 2. Aim of the work

Considering the previously discussed advantages of 3D cell and tissue culture models, the feasibility of microextrusion technique over other matrix fabrication techniques, and the potential of working with a collagen-based hydrogel, the final aim of this work is the development of an *in vitro* model of the human lung that better mimics the stromal component of the lung tissue.

Different hydrogel-compositions and 3D printing approaches will be exploited to finally obtain a proper scaffold suitable for tissue engineering applications. Regarding the 3D printed scaffolds, collagen type I will be the main constituent because of its biocompatibility and its physical gelation property: the ability to self-assemble *in vitro* to form insoluble fibrils under proper conditions. This last characteristic of biological hydrogels represents an advantage and meanwhile, a limitation as they are challenging materials for 3D printing applications because they must be gelled *in situ* during the fabrication process and, simultaneously, supported so that they do not collapse or deform under their own weight. In particular, two different 3D printing approaches will be implemented: a freeform fabrication strategy and deposition within a support bath, and the printing parameters will be optimized, leading to a better control of the scaffold final shape.

Morphological and mechanical characterization of 3D printed structures will be performed by scanning electron microscopy (SEM). Concerning the hydrogel, different concentrations of collagen hydrogels will be explored, and they will be characterized in terms of morphology with gradient light interference microscopy (GLIM), and mechanical properties performing both qualitative and quantitative tests.

Finally, a CAD (computer-aided design) model of a pulmonary acinus will be design according to the real nominal size of the human lung acinus with the future outlook of printing the 3D model in a scaled-up version.

## 3. Materials and Methods

### 3.1 Collagen solution

#### 3.1.1 Components

#### Collagen

In this work, type-I collagen was used for the bioink, obtained from Blafar Ltd. Blafar's atelocollagen type I is extracted from certified BSE/TSE-free bovine Achilles tendons (Australia origin) and is treated to minimize viral and endotoxin contamination. Atelocollagen is pepsin-digested in an acidic solution to remove antigenic telopeptides [49].

	<b>Supplier</b>	Blafar Ltd.
	<b>Product name</b>	Bovine Collagen Type I Powder
	<b>Form</b>	Collagen Type I Powder
	<b>Purity</b>	> 85%
	<b>pH</b>	2.0 – 3.0
	<b>Solubility</b>	10 mg/mL in chilled HCl (< 1 mM) or chilled purified endotoxin-free water

Table 8. Collagen type I powder, product description [49].

### DMEM

DMEM (Dulbecco's Modified Eagle Medium) is a widely used basal medium for supporting the growth of many different mammalian cells.

	<b>Supplier</b>	Thermo Fisher Scientific
	<b>Product name</b>	Dulbecco's Modified Eagle Medium
	<b>Form</b>	Liquid

Table 9. DMEM, product description [50].

### Acetic Acid

Acetic acid is an aliphatic organic acid. It is a hygroscopic, corrosive liquid with a vinegar-like odor. Glacial acetic acid is the anhydrous acetic acid and is widely employed as solvent for various oxidation reactions [45].

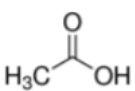
	<b>Supplier</b>	Sigma – Aldrich
	<b>Product name</b>	Acetic acid - glacial
	<b>Form</b>	Liquid

Table 10. Acetic acid – glacial, product description [51].

### Sodium hydroxide

Sodium hydroxide (NaOH) also known as caustic soda is a water-soluble inorganic base. This common laboratory alkali is used as a buffer solution (adjusting pH), among other applications [52].

	<b>Supplier</b>	Sigma – Aldrich
	<b>Product name</b>	Sodium hydroxide
	<b>Form</b>	Pellets
	<b>Solubility</b>	1,260 g/L at 20 °C in H <sub>2</sub> O

Table 11. Sodium hydroxide, product description [52].

### 3.1.2 Collagen based hydrogel generation

The bovine tendon collagen is dissolved in 0.5 M acetic acid. To prepare this solution, the procedure was the following (Figure 3.1):

1. After deciding the volume and the final concentration of the collagen solution, proceed with mixing the solvents: DMEM and glacial acetic acid (final concentration 0.5M), in a volumetric flask or beaker. It results in an acid solution, pH < 4.0.
2. Preserve the solution under stirring (~350 rpm) assuring a cold platform (~10°C).
3. Weigh out the required mass of collagen. Under stirring, gradually add the powder to the solution. Mix until dissolve the solid.
4. Place a cap on the beaker and storage the solution under stirring (~60 rpm) in the fridge (~4°C) for at least 12 hours to ensure complete homogenization of the solution.

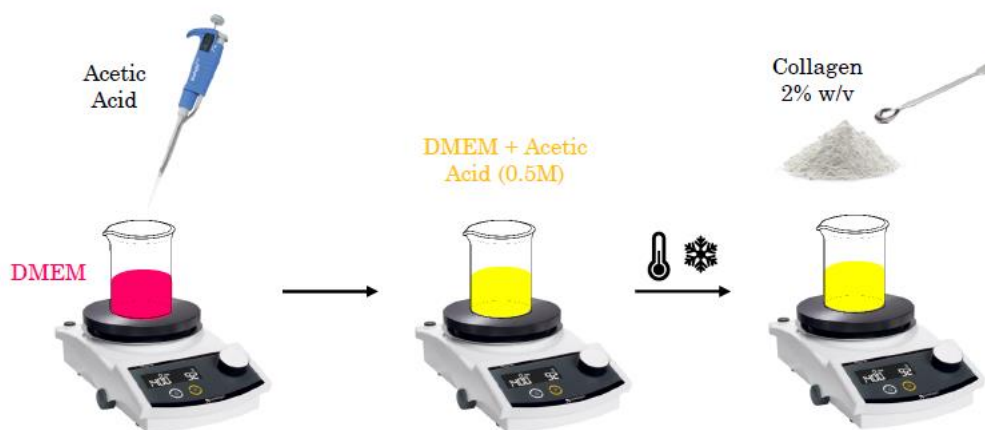


Figure 3.1 Collagen based hydrogel preparation.

After ensuring that the solution is homogeneous, the next step consists of neutralizing the pH of the final solution (Figure 3.2).

5. Check the pH using a pH meter and adjust the pH as necessary using sodium hydroxide (NaOH, 1M) until reaching the closest value to physiologic pH (7.14).

During the neutralization process, the color of the solution let us estimate the pH of the solution, as it changes from yellow to peach (pinkish orange), showing the transition from acid to neutral pH. Nevertheless, the final pH is measured with the pH meter.

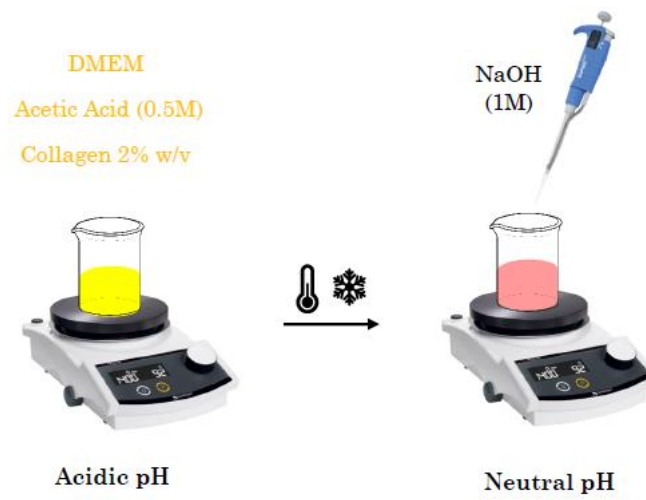


Figure 3.2 Neutralization of the collagen based solution.

## 3.2 Gelatin slurry support bath

Printing collagen-based 3D structures turned out to be challenging as biological hydrogels must first be gelled in situ during the fabrication process and then supported so that they do not collapse or deform under their own weight.

In this context, an alternative printing method was implemented, the innovative freeform reversible embedding of suspended hydrogels (FRESH, [53]). Consists in the deposition and embedding of the hydrogel(s) being printed within a second hydrogel support bath that maintains the intended structure during the print process and significantly improves print fidelity. The support bath is composed of gelatin microparticles that act like a Bingham plastic during the print process, behaving as a rigid body at low shear stresses but flowing as a viscous fluid at higher shear stresses [53]. Once the entire 3D structure is FRESH printed, the temperature is raised to a cell-friendly 37°C, causing the gelatin support bath to melt in a non-destructive manner. In addition to its rheological and thermoreversible properties, gelatin was selected as the support bath material because it is biocompatible, thus residual gelatin will not negatively affect cell integration.

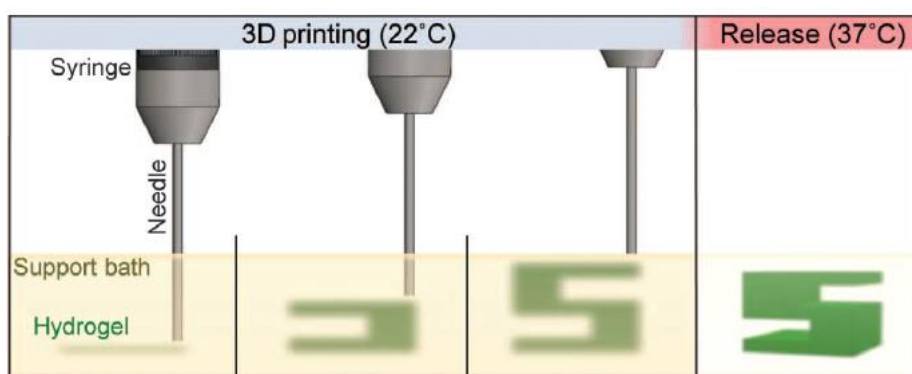


Figure 3.3 Schematic of the FRESH process showing the hydrogel (green) being extruded and cross-linked within the gelatin slurry support bath (yellow). The 3D object is built layer by layer and, when completed, is released by heating to 37°C and melting the gelatin [53].

### 3.2.1 Components

#### Gelatin

Gelatin is a heterogeneous mixture of water-soluble proteins of high average molecular weights, present in collagen. The proteins are extracted by boiling skin, tendons, ligaments, bones, etc. in water. Type A gelatin is derived from acid-cured tissue and Type B gelatin is derived from lime-cured tissue [54].

In this work, the gelatin used was purchased from Sigma – Aldrich. The gelatin type A powder is obtained from porcine skin and has an off-white to yellow appearance.

	<b>Supplier</b>	Sigma – Aldrich
	<b>Product name</b>	Gelatin from porcine skin powder
	<b>Type</b>	A
	<b>Form</b>	Powder
	<b>Solubility</b>	50 mg/mL of H <sub>2</sub> O

Table 12. Gelatin, product description [54].

### Calcium dichloride

Calcium chloride (CaCl<sub>2</sub>) is an inorganic compound. It is a white colored crystalline salt at room temperature, and it is highly soluble in water.

	<b>Supplier</b>	Sigma – Aldrich
	<b>Product name</b>	Calcium chloride
	<b>Form</b>	Beads
	<b>Molar mass</b>	110.98 g/M

Table 13. Calcium chloride, product description [55].

### HEPES

HEPES has been described as one of the best all-purpose buffers available for biological research. At biological pH, the molecule is zwitterionic (contains an equal number of positively charged functional group(s) and negatively charged functional group(s)), and is effective as a buffer at pH 6.8 to 8.2. HEPES has been used in a wide variety of applications, including tissue culture [56].

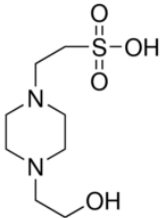
	<b>Supplier</b>	Sigma – Aldrich
	<b>Product name</b>	HEPES buffer solution
	<b>Form</b>	Liquid
	<b>Concentration</b>	1 M in H <sub>2</sub> O 238 g/L HEPES in H <sub>2</sub> O

Table 14. HEPES, product description [56].

### 3.2.2 Generation of the gelatin slurry support bath

Two different solutions were necessary to prepare the final gelatin slurry support bath following the protocol described by Hinton et al. [31]. The first one (I) is the gelatin solution and the second one (II) is the rinse solution.

- I. **Gelatin solution (150ml).** In a volumetric flask: 150 ml of 4.5% (w/v) gelatin (Type A, Sigma – Aldrich) in 11 mM  $\text{CaCl}_2$  (Sigma-Aldrich) was mixed into a solution. The solution was supplemented with 10 mM HEPES to maintain a pH of  $\sim 7.4$ . The gelatin solution was transferred to a 500-ml mason jar, then gelled it for 12 hours at  $4^\circ\text{C}$ .
- II. **Rinse solution (500ml).** Calcium dichloride beads were dissolved in water+HEPES. Final concentration  $\text{CaCl}_2=11\text{mM}$ , HEPES= $10\text{mM}$ . The solution was kept under  $4^\circ\text{C}$ .

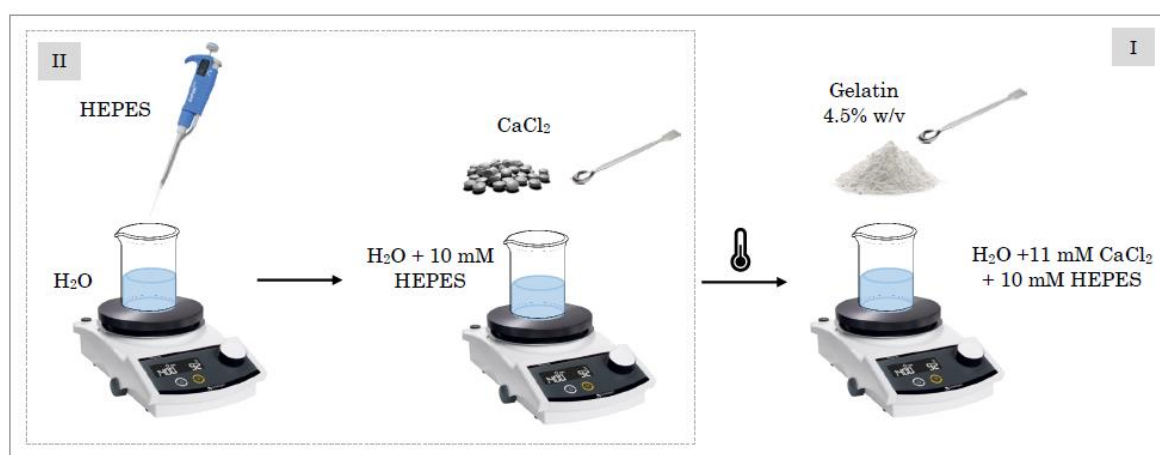


Figure 3.4 Elaboration of the solutions necessary for the generation of the gelatin slurry support bath. II- Rinse solution and I- Gelatin solution.

Protocol for the generation of the gelatin slurry support bath:

1. 350 ml of 11 mM  $\text{CaCl}_2$  (Solution II) at  $4^\circ\text{C}$  was added to the jar (Solution I) and its contents were blended (at “pulse” speed) for 120 s with a blender.
2. The blended gelatin slurry was loaded into 50-ml conical tubes or falcon.
3. Then, the falcons were centrifuged at 4200 rpm for 2 min, causing slurry particles to settle out of suspension.
4. The supernatant was removed and replaced with 11 mM  $\text{CaCl}_2$  at  $4^\circ\text{C}$  (Solution II).
5. The slurry was vortexed back into suspension and centrifuged again.

This process (steps 4 and 5) were repeated until no bubbles were observed at the top of the supernatant, which indicated that most of the soluble gelatin was removed. At this point, gelatin slurries could be stored at  $4^\circ\text{C}$ .

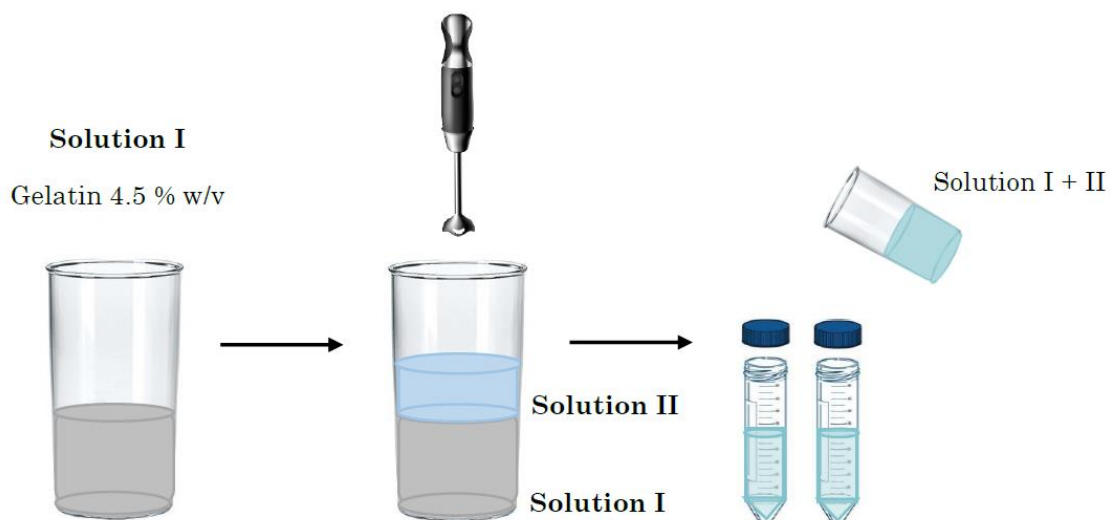


Figure 3.5 Generation of the gelatin slurry support bath. Steps 1 and 2.

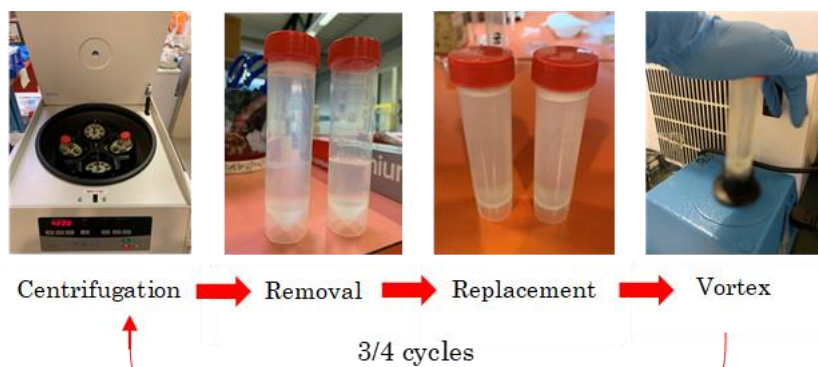


Figure 3.6 Generation of the gelatin slurry support bath. Steps 3,4 and 5.

For FRESH printing, the slurry was poured into a petri dish where the 3D structure was going to be printed. During the process, the support bath was supplemented with 10 mM HEPES to maintain a pH of  $\sim 7.4$  and neutralize the acetic acid of the collagen solution.

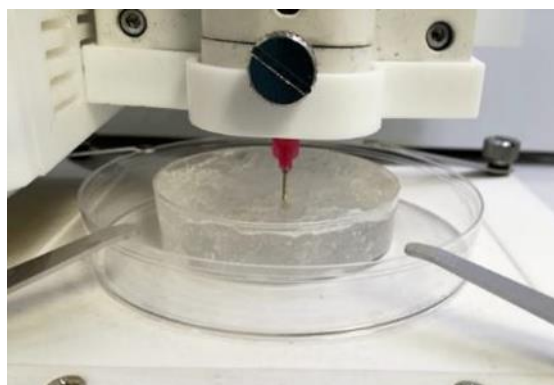


Figure 3.7 Gelatin slurry poured into a petri dish ready for 3D printing.

### 3.3 Characterization of the collagen hydrogel: sol-gel transition.

#### 3.3.1 *Tube inverting test*

The most common diagnostic test of gelation is to turn a test-tube or vial containing the sample upside-down and then to note whether the sample flows under its own weight, giving qualitative information of the sol-gel transition.

The sol (flow) - gel (no flow) phase transition temperatures of three different collagen solutions were tested using the test-tube-inverting method: 0.5 % w/v, 1 % w/v and 2 % w/v, coded as Coll 0.5, Coll 1 and Coll 2 respectively. Samples of 2 mL were tested inside plastic test tubes (bijoux). The incubation temperature was set at 37°C and the test was carried out for 20 minutes, with a time-lapse of 5 minutes to note the transition. The phase transition was observed visually by inverting the bijoux, and a gel was defined when no significant flow was observed within 1 min.

The analysis was performed inside a laboratory incubator (DIMEAS Laboratory, Dipartimento di Ingegneria Meccanica e Aerospaziale, Politecnico di Torino).

#### 3.3.2 *GLIM optical microscopy*

GLIM (Gradient light interference microscopy) is an add-on module to a commercial DIC microscope. In a differential interference contrast (DIC) microscopy the contrast is generated by visualizing the modifications of the wavefront when light propagates through the sample. DIC is qualitative—that is to say, it does not measure the wavefront deformation quantitatively (Figure 3.8).

In GLIM, the two interfering fields are identical except for a small transverse spatial shift. This geometry ensures that the two fields suffer equal degradation due to multiple scattering. As a result, GLIM rejects much of the multiple scattering contributions and yield high contrast of thick objects. GLIM can provide tomographic imaging of both thin samples, for example, single cells, and thick specimens, such as multicellular systems.

#### **GLIM principle**

GLIM can be considered as an extra module set up in a commercial DIC microscope as shown in Figure 3.9. Via a Wollaston prism, a typical DIC microscope generates two replicas of the image field, cross-polarized, shifted transversely by a distance smaller than the diffraction spot. Removing the analyzer that normally renders the two polarizations parallel in DIC and, instead, letting the fields enter the GLIM module. These fields are spatially Fourier transformed by the lens L1 at its back focal plane. A spatial light modulator (SLM), device that is used to modulate the spatial distribution of light waves, is placed at this plane with its active axis aligned to the polarization direction of one field.

The SLM retards its phase by  $\phi_n = n\pi/2$  with  $n = 0, 1, 2, 3$ , and leaves the other field unmodified. Both fields are Fourier-transformed again by lens L2 to generate the image at the camera plane. A linear polarizer, P1, is aligned at  $45^\circ$  with respect to both polarizations to render them parallel. The resulting field at the detector is a coherent superposition of these two fields [57].

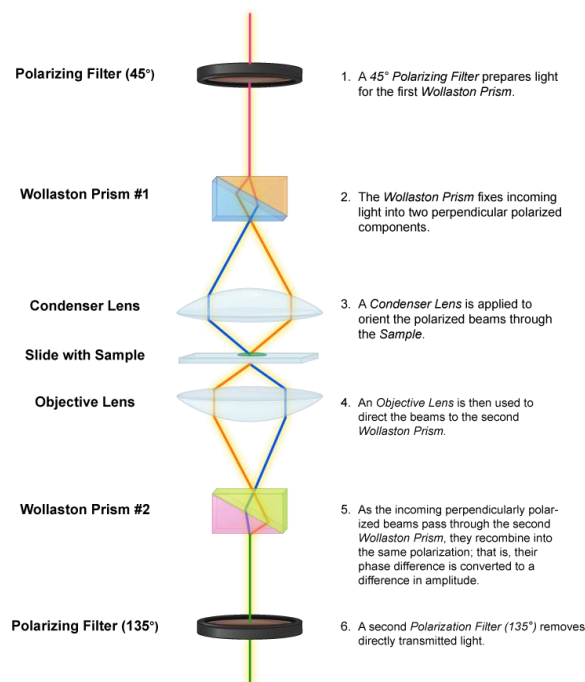


Figure 3.8. Differential interference contrast (DIC) mechanism [58].

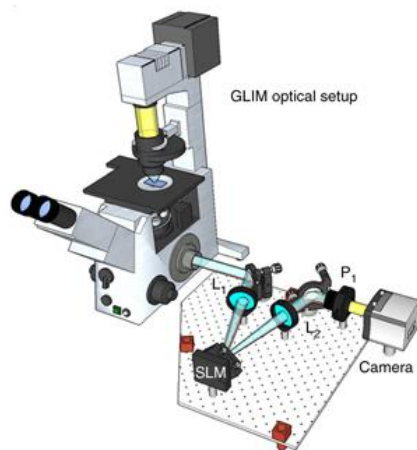


Figure 3.9 GLIM optical setup [57].

GLIM can be applied to imaging live cells and thick samples nondestructively over broad temporal and spatial scales. This technique is not limited by photobleaching and phototoxicity commonly associated with other techniques like fluorescence microscopy. Also, it provides excellent optical sectioning and obtains 3D information from unlabeled specimens [57].

GLIM optical microscopy tests of neutralized Coll 2 solution were carried out by using a gradient light interference microscopy to study the fibrillogenesis process during the gelation of the collagen sample, influenced by temperature. The aqueous solution was placed on the sample holder, and the microscopic image was photographed for 20 minutes with 2' intervals (resulting in 10 images) and heating the sample holder at 37 °C.

### 3.3.3 *FE-SEM*

Field Emission Scanning Electron Microscope or FESEM is microscope that works with electrons instead of light. These electrons are liberated by a field emission source and the object is scanned by them according to a zig-zag pattern. This technique is used to visualize topographic details on the surface or entire or fractioned objects. Compared with convention scanning electron microscopy (SEM), field emission SEM (FESEM) produces clearer, less electrostatically distorted images with spatial resolution down to 1 nanometer – three to six times better.

The FE-SEM has been used to analyze the presence microfibrillar structure in lyophilized collagen samples. The instrument available at DIMEAS is the ZEISS MERLIN, figure 3.10.



Figure 3.10 FE-SEM Zeiss Merlin.

The sample preparation consisted in the lyophilization of a Coll2 sample, followed by the slicing of the sample into a smaller specimen and placement on a FE-SEM stub. Finally, the sample was coated with a 10 nm chrome layer. The morphology was observed at an accelerating voltage of 3 kV.

## 3.4 Scaffold printing

### 3.4.1 Rokit INVIVO

The Rokit Invivo (DIMEAS Laboratory, Politecnico di Torino) is a 3D bioprinter made by ROKIT, a manufacturer from South Korea. The INVIVO is suitable for biomedical applications. It allows to create versatile 3D cellular structures with multi material and extensive designs. It consists in a modular system and sterile environment, with android OS touchscreen where users can upload/download and print the 3D file with Wi-Fi network, monitoring printing status.

This 3D bioprinter is compatible with a wide range of materials for biofabrication. These include proprietary biopolymer filaments, hydrogels, and photo-curable bio-ink (or “bioink”).



Figure 3.11 Rokit Invivo bioprinter

#### INVIVO biofabrication print heads

- FDA-approved extruder: to 3D print with ROKIT's proprietary filament.
- Bio dispenser: for mechanical extrusion (0.008 to 0.2 mm nozzle diameters).
- Pneumatic dispenser (optional): in order to use high-viscosity materials (0.1 to 0.5 mm nozzle diameters). This dispenser can heat up to 350°C.

#### INVIVO main features

- Onboard camera: users can monitor their 3D prints from a distance.
- Air filtration: the INVIVO features a H14 HEPA filter, to reduce particle emissions.
- Bio-ink warmer: this function preheats bio-ink to prepare for 3D prints.
- UV LED (365nm) and UV lamp (12W/254nm): to solidify photo-curable materials and sterilize the environment.
- Print bed temperature control (optional): the print bed is able to maintain specific temperatures, ranging from -4°C to 80°C.

## 3.4.1.1 Printing parameters and initialization

Digital models were created in computer-aided design (CAD) software (SOLIDWORKS 2016). All 3D models were then exported as an STL format file and processed in NewCreatorK slicer software to generate G-code instructions for the printer. The main parameters varied were layer height, fill density, printing temperature, print speed, filament diameter and input flow.

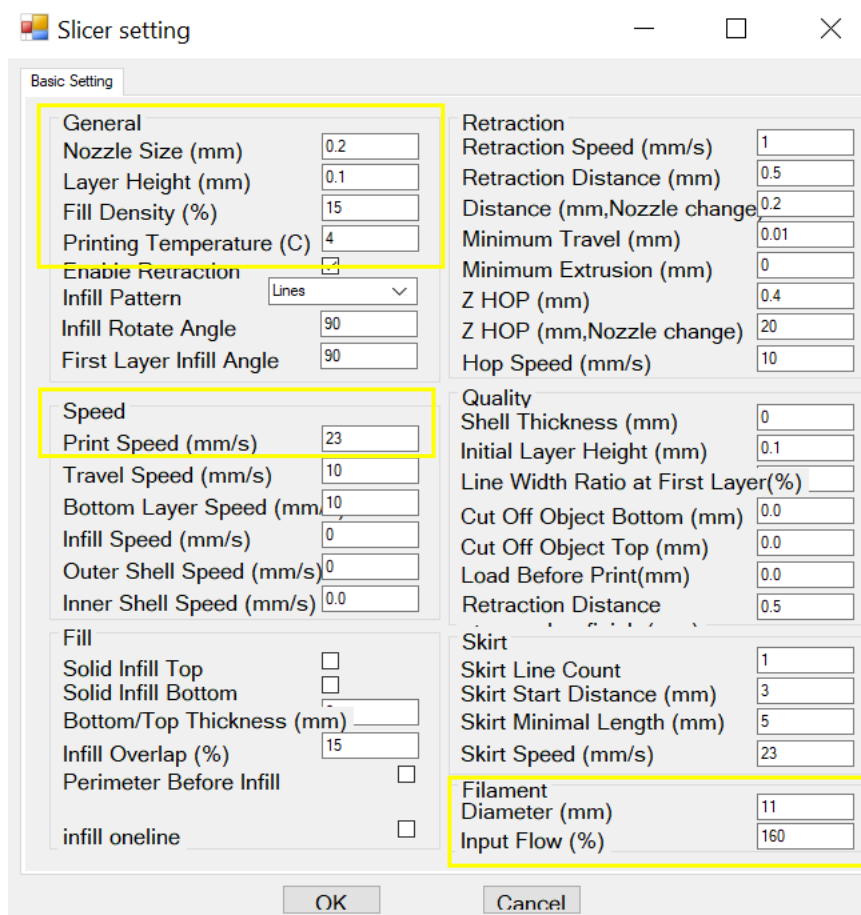


Figure 3.12 NewCreatorK slicer settings.

- Layer height (mm): is the thickness of each layer, and it is the step along the z-axis taken before extruding a new layer in the top of the previous one.
- Fill density (%): goes from 0% to 100%. It is the amount of filament printed inside the object, for instance, 100% means that the model is completely filled with the printing material. Instead, most models can be filled with less material and still have good mechanical strength.
- Printing temperature (°C): bioink dispenser temperature.
- Print speed (mm/s): refers to the speed at which the extruder travels while it lays down the filament.
- Filament diameter (mm): not necessary equivalent to the needle inner diameter.
- Input flow (%): allows the fine tuning of the extrusion flow rate. The quantity of extruded material is multiplied by this value.

In general, slicer settings were varied around the next values: print speed of 4-6-8 mm s<sup>-1</sup>, layer height of 0.08-0.1-0.2 mm, filament diameter 11-12 mm, input flow 120-160% and 15% fill density. While maintaining a printing temperature of 4°C (temperature referred to the bioink dispenser), to avoid the collagen gelation. Prior to printing, collagen bioink was transferred into a gastight plastic syringe (10 mL) and mounted into the Biodispenser. A needle was fitted to the syringe and primed. The needle was typically a plastic needle with an inner diameter (ID) of 200 µm. We also used a stainless steel with an ID of 200 µm.

A Petri dish large enough to hold the construct to be printed was set in the printing bed, previously heated at 37°C, temperature maintained until the printing process ended.

The touch screen allows the user to manually calibrate the position of the biodispenser, thus the needle was manually positioned in the x-y center of the petri dish and lowered to 1 mm above the bottom of the print container (z-axis calibration). The 3D print was then started.

Upon print completion, the container was removed from the platform and incubated at 37°C.

#### Considerations

**Gcode.** The printing process was performed following the optimized Gcode from a previous work [59] in which a 60 seconds pause was established between one layer and the subsequent, with the aim of ensuring collagen-layer polymerization. By the use of a programming language, specifically Python, the Gcode files were modified to add a set of instructions (Figure 3.13) that allowed the addition of the pause.

```

C:\Python27\python.exe
Python 2.7.6 (default, Nov 10 2013, 19:24:18) [MSC v.1500 32 bit (Intel)] on win32
Type "help", "copyright", "credits" or "license" for more information.
>>> p = ('\n')
>>> i = 1
>>> j = 1
>>> z = 0.1
>>> l = 0.05931
>>> v = 90
>>> f1 = open('C:\Users\laraa\Desktop\Pausa.txt', 'w')
>>> with open('C:\Users\laraa\Desktop\A.gcode') as f:
...     for line in f:
...         x = line.startswith("M73")
...         if x == True and line[5] != "0":
...             E = 0.05000
...             Es = E + (i*0.00008)
...             e = round(Es,6)
...             z1 = z + (i*0.1)
...             z2 = round(z1,2)
...             load = l + 0.06013
...             l = round(load,6)
...             pausa='\n;ENABLE RETRACTION\nG1 F60 E-{0} (retractionAmount)
\nG1 Z{1} F60 H1(retractionZHop)\n;PAUSA\nG1 Z40.000 F60 (Nozzle Hop)\nG1 F60 E{2} (
Back-retraction)\n'.format(e,z2,l)
...             f1.write(pausa+p+line)
...             i += 1
...         else:
...             f1.write(line)
>>> f1.close()

```

Figure 3.13 60 seconds PAUSE algorithm.

The following parameters vary from one layer to the other and need to be modified manually (but automatically calculated by the algorithm) when adding the pause instructions:

- E: the extrusion value. It increases with each new layer. It can be positive (+) when corresponds to a load value, but it can also be negative (-) associated to a retraction amount, usefull when adying the pause and proceed to rising the tip.
- Z: extruder position in the Z axis. Initially, it is equal to 0.1 (height of each layer), and increases in 0.1 at each layer.

```
for line in f:
    x = line.startswith("M73")
    if x == True and line[5] != "0":
        E = 0.05000
        Es = E + (i*0.00008)
        e = round(Es,6)
        z1 = z + (i*0.1)
        z2 = round(z1,2)
        load = l + 0.06013
        l = round(load,6)
```

The beginning of a new layer is pointed out as follows: "M73 P # ( Layer: #) "

It is unnecessary to add the pause before the 1st layer, so the code will avoid the first layer (identified with the number "0")

```
x = line.startswith("M73")
if x == True and line[5] != "0":
    E = 0.05000
    Es = E + (i*0.00008)
    e = round(Es,6)
    z1 = z + (i*0.1)
    z2 = round(z1,2)
    load = l + 0.06013
    l = round(load,6)
```

Load = corresponds to the increase between one layer and another of the load.

This value must be obtained from the gcode and is calculated as follows:

$$\text{Elayer2} - \text{Elayer1}$$

The resultant value remains equal from one and another layer

```
;Layer count: 49
M73 P0 ( LAYER: 1 )
;LAYER:1
M106 S255 (Fan On)
G0 F420 X43.900 Y40.500
G0 F420 Z0.200

;TYPE:SKIRT
G1 Z0.200 F60
G1 F120 E0.00000 (Back-retraction)
G1 F240 X60.900 Y40.500 E0.00859
G1 X60.900 Y57.500 E0.01717
G1 X43.900 Y57.500 E0.02576
G1 X43.900 Y40.500 E0.03435
G0 F180 X44.100 Y40.700
G1 F240 X60.700 Y40.700 E0.04273
G1 X60.700 Y57.300 E0.05111
G1 X44.100 Y57.300 E0.05950
G1 X44.100 Y40.700 E0.06788
G0 F180 X44.300 Y40.900
G1 F240 X60.500 Y40.900 E0.07607
G1 X60.500 Y57.100 E0.08425
G1 X44.300 Y57.100 E0.09243
G1 X44.300 Y40.900 E0.10061
G0 F180 X47.469 Y44.656
;TYPE:FILL
G1 F240 X57.329 Y44.656 E0.10559
```

**Elayer1**

```
M73 P2 ( LAYER: 2 )
;LAYER:2
G0 F180 X56.652 Y53.929
G0 F90.0 Z0.100

;TYPE:FILL
G1 F240 X56.652 Y44.069 E0.13796
G0 F180 X55.319 Y44.069
G1 F240 X55.319 Y53.929 E0.14045
G0 F180 X53.986 Y53.929
G1 F240 X53.986 Y44.069 E0.14294
G0 F180 X52.653 Y44.069
G1 F240 X52.653 Y53.929 E0.14543
G0 F180 X51.320 Y53.929
G1 F240 X51.320 Y44.069 E0.14792
G0 F180 X49.987 Y44.069
G1 F240 X49.987 Y53.929 E0.15041
G0 F180 X48.654 Y53.929
G1 F240 X48.654 Y44.069 E0.15290
```

**Elayer2**

Figure 3.14 Command specifications.

```

...          pausa='\n;ENABLE RETRACTION\nG1 F60 E-{0} (retractionAmount)
\nG1 Z{1} F60 H1(retractionZHop)\n;PAUSA\nG1 Z40.000 F60 (Nozzle Hop)\nG1 F60 E{2} (
Back-retraction)\n'.format(e,z2,l)
...          f1.write(pausa+p+line)

```

```

;ENABLE RETRACTION
G1 F90.0 E-0.05007 (retractionAmount)
G1 Z0.2 F90.0 H1(retractionZHop)
;PAUSA
G1 Z40.000 F90.0 (Nozzle Hop)
G1 F90.0 E0.13472 (Back-retraction)

```

→ Pause settings: the discharge (E - #), the extruder rise (z, nozzle Hop) and load (E + #) values.

Figure 3.15 New commands introduced for the PAUSE.

**FRESH printing.** For the 3D bioprinting of collagen type I performed using the FRESH support bath [53], the slurry was poured into a petri dish where the 3D structure was going to be printed. Almost all printing parameters described above remained unaltered, only the temperature of the printing bed was lowered to 22°C, temperature that preserves the slurry rheological properties. The Gcode files implemented were exactly the same used previously but, without the addition of the pause instructions. Upon print completion, the container was removed from the platform and incubated at 37°C to melt the FRESH support bath and release the printed construct.

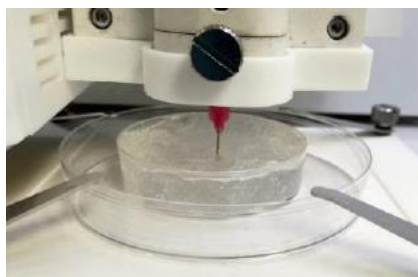


Figure 3.16 FRESH printing method.

### 3.4.2 *BioX Cellink*

The Cellink Bio X (Polito BIO Med Laboratory, Politecnico di Torino) is a desktop bioprinter. The BIO X software allows the user to built-in features along its user-friendly software managed through the touchscreen display. It has two high-power fans that produce a powerful airflow through the top of the 3D printer where two HEPA H14 filters are built in. This creates a positive pressure inside the chamber and ensures that more than 99.995% of unwanted particles and microorganisms are retained. The UV-C germicidal lamps in the Bio X allow you to sterilize the printing environment by running sterilization cycles.



Figure 3.17. BioX Cellink bioprinter

Its main features are:

Three (swappable) print heads, including:

- Standard Pneumatic Printhead
- Electromagnetic Droplet Printhead
- Temperature-controlled Pneumatic Printhead
- Syringe Pump Printhead
- Thermoplastic Printhead
- Photocuring Toolhead: exchangeable photocuring modules of 365 nm and 405 nm.
- HD Camera Toolhead

Temperature Controlled Printbed (4°C to 60°C).

Clean chamber technology with UV-C germicidal lamps and HEPA H14 dual-filter system.

#### 3.4.2.1 Printing parameters and initialization

The same Gcodes used for the ROKIT bioprinter were transferred and used in the Bio X. Some manual modifications were performed in the Gcodes to adapt them to the new bioprinter, like the initial position of the printhead since both printers differ in size. One point of view in favor of the BioX bioprinter is that the printing parameters are set up in the initial calibration point and some of them can be modified while the printing process is carried out.

BIO X guides you through the process of setting up your bioprint (Figure 3.18, [60]):

- A. Choose the option to start a new bioprinting process using a 3D model.
- B. Select the file (Gcode or .stl file).
- C. Select the surface to bioprint on and indicate the surface size. We select Petri dish.
- D. Depending on the printhead, different settings are required for configuration. A simple structure, a 3D cube ( $10 \times 10 \times 5 \text{ mm}^3$ ), was printed using CELLINK® START bioink with a pneumatic printhead and inactive photocurable tool. At this point calibration settings were the following: nozzle type 0.410 mm, print speed 5 and 3mm/s, pressure 200 kPa, temperature for both print bed and printhead were inactivated as the printing process was performed at room temperature.

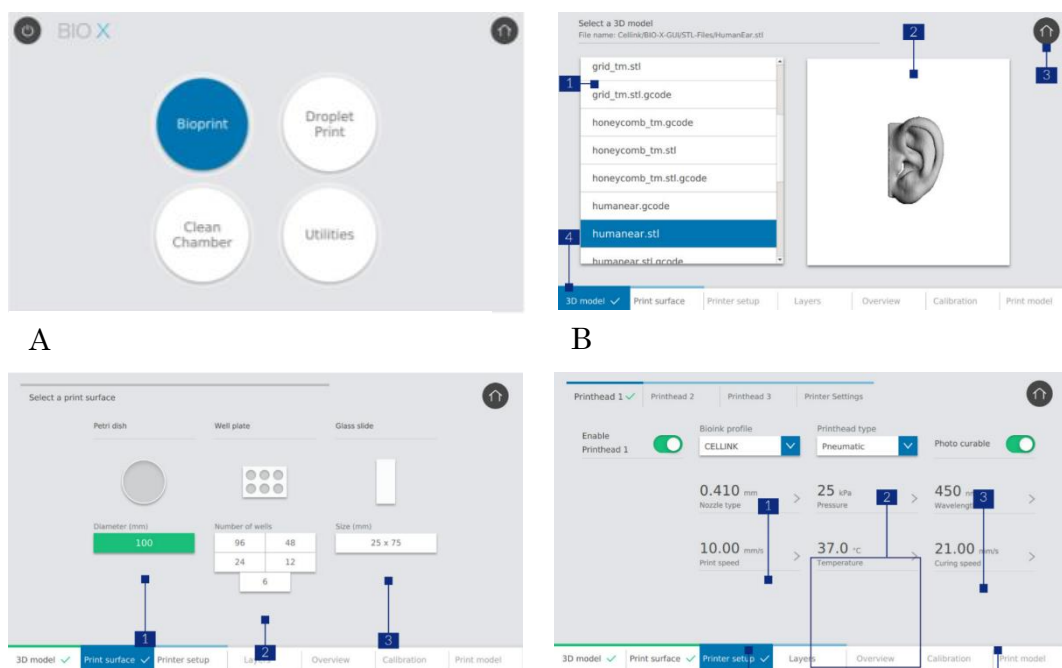


Figure 3.18 BioX calibration settings.

### 3.5 Three-dimensional model of a pulmonary acinus

A computational model of a lung acinus was created in CAD (computer-aided design) using the Solidworks® platform. The pulmonary acinus model presented consists in a central respiratory bronchiole surrounded along its surface by spherical units representing single alveoli (Figure 3.19). Since vascularization is a central challenge of all tissue engineering, this review will not discuss it at length, instead focusing on the specific challenges associated with alveolar printing. The lung acinus is the basic functional unit of the lung with a nominal size of 6-10 mm<sup>3</sup>. In the alveoli that form de acinus model, the alveoli are represented by spheres with an inner diameter ~ 500 μm, the septal layer simulating the connective matrix and alveolar walls have been designed with a nominal size of 50 μm. The central bronchiole is represented by a hollow cylinder of 250 μm inner diameter with 50 μm wall thickness and ~1 mm length. Dimensions that are reported in Figure 3.20 for better understanding.

We propose that the hole acinus model can be printed/molded scaled up by an order of magnitude with an overall length from trunk to tip of ~2.5 cm.

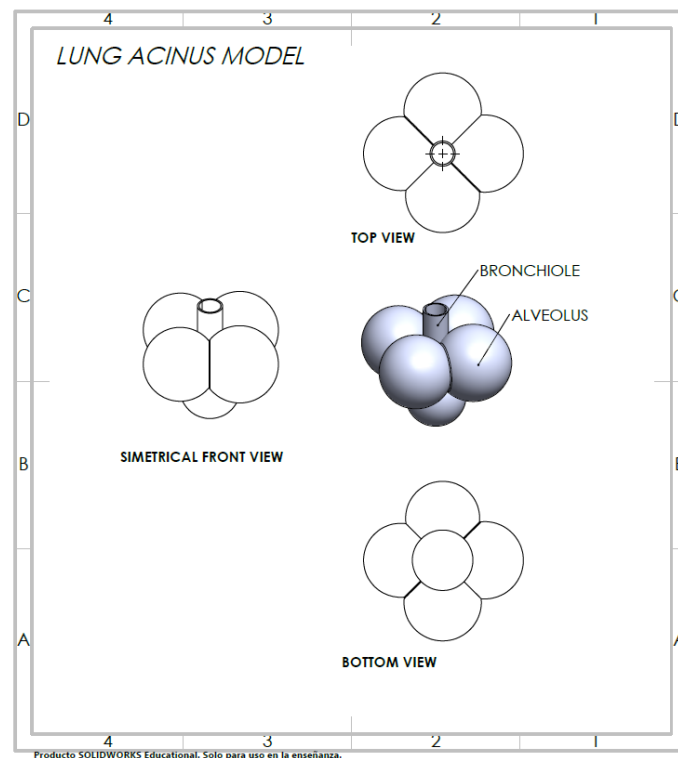


Figure 3.19 3D CAD model of the pulmonary acinus. Top, bottom and simetrical front views.

With the intent to model both internal and external architecture, two particular inner structures can be identified in the model (Figure 3.21). The first one refers to discrete holes in walls of adjacent alveoli corresponding to pores of Kohn. In the lung physiology, these apertures in the alveolar septum allow the communication of two contiguous alveoli.

Then, the second unit refers to the openings of the alveolar ducts that communicate the alveolus cavity with the bronchiole lumen.

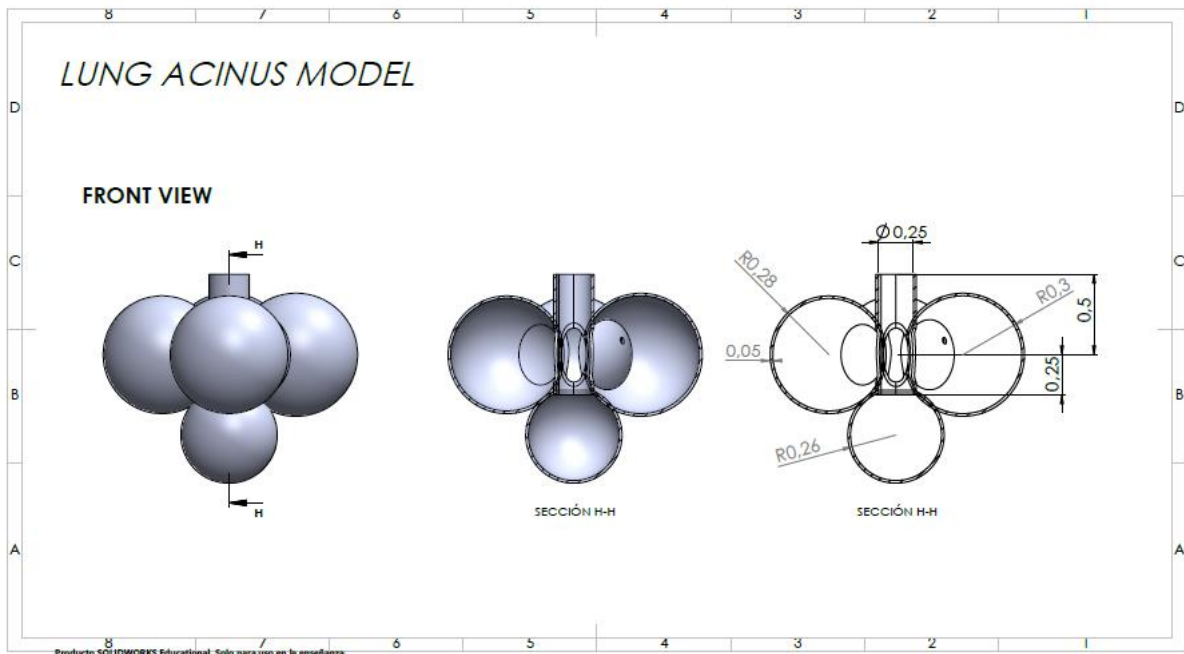


Figure 3.20 3D CAD model of the pulmonary acinus. Front view and H-H section view with dimensions in mm

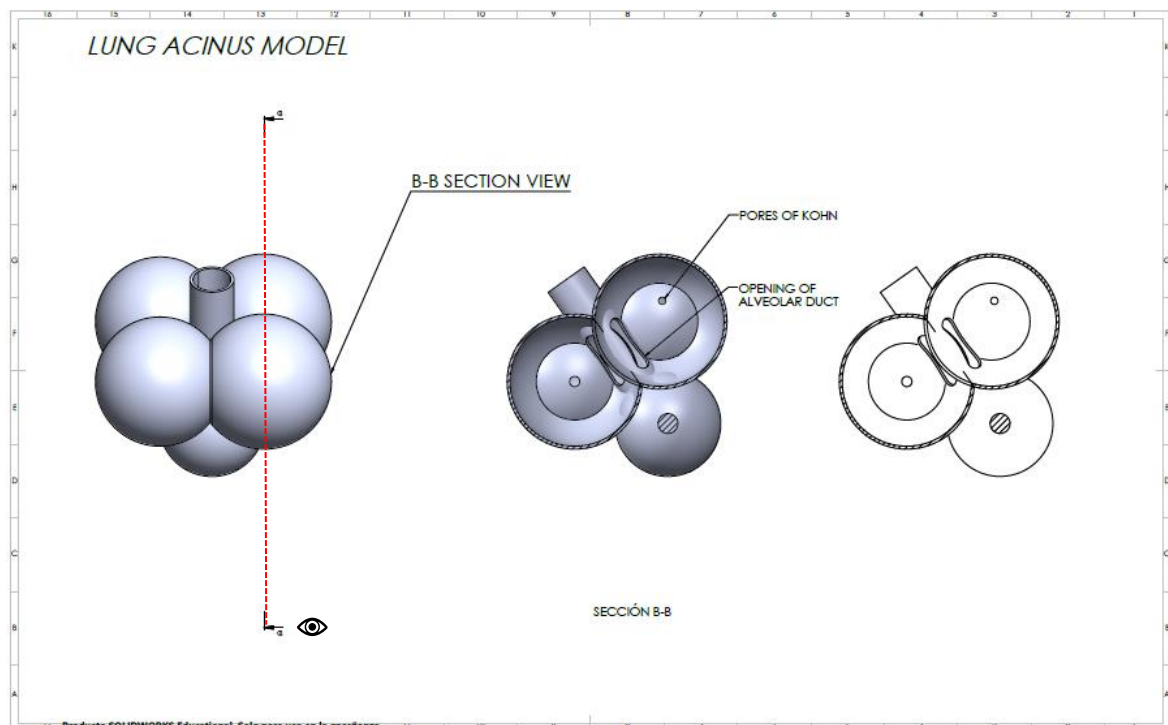


Figure 3.21 3D CAD model of the pulmonary acinus. Section B-B view. Two different structures can be identified: Pores of Kohn and the opening of the alveolar ducts.

Finally, in Figure 3.22 it is possible to observe the relation between adjacent alveoli and how they share their alveolar walls, except from one and only complete spherical structure (red circle).

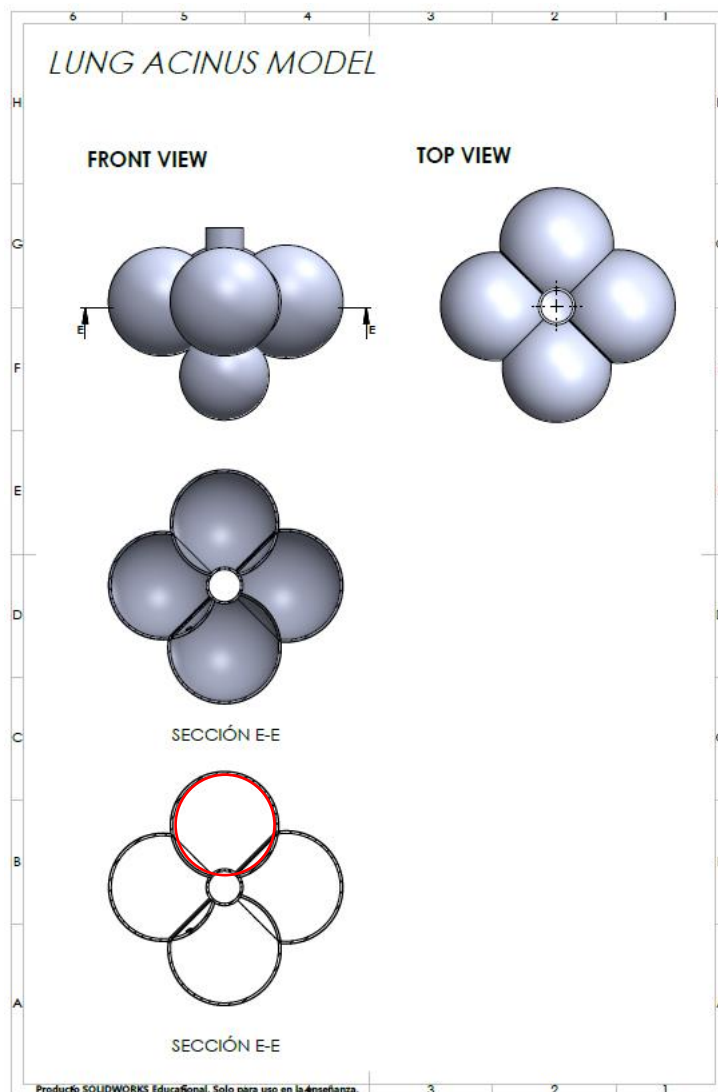


Figure 3.22 3D CAD model of the pulmonary acinus. Section E-E view. The red circle corresponds to the only complete sphere, the other ones share their wall with the neighbour sphere.

For the realization of the model we propose two different matrix fabrication techniques, considering two main limitations: the printing material and the complex architecture of the pulmonary acinus model. To build a complex multiscale organ from a material such as collagen I, advanced fabrication techniques are needed to transform a soft biological material into stable 3D structures.

Approaches are limited in their ability to obtain 3D complex structures from a collagen hydrogel because soft materials must first be gelled in situ during the fabrication process and then supported so that they do not deform under their own weight. Using support

materials can be a good method to deal with the collapse issue. In addition, thermal, mechanical, and chemical conditions must be preserved to prevent damage to biological hydrogels and potentially integrated cells.

### 3.5.1 3D bioprinting

Bioprinting has the advantage of creating high complex architectures accompanied with the potential to address problems of insufficient cell ingrowth into decellularized matrices, since cells can be introduced directly throughout the volume of the bioprinted construct.

Hinton et. al [53] demonstrate the unique ability of FRESH to print hydrogels with complex internal and external structures, this method, developed in section 3.2 and depicted in Figure 3.6, uses a gelatin microparticle support bath. FRESH was used to print complex biological structures based on medical imaging data from brain (scaled down to ~3 cm) and embryonic chick heart (scaled up to ~2.5 cm) and proved the capability of this technique to fabricate challenging structures with complex internal and external architectures.

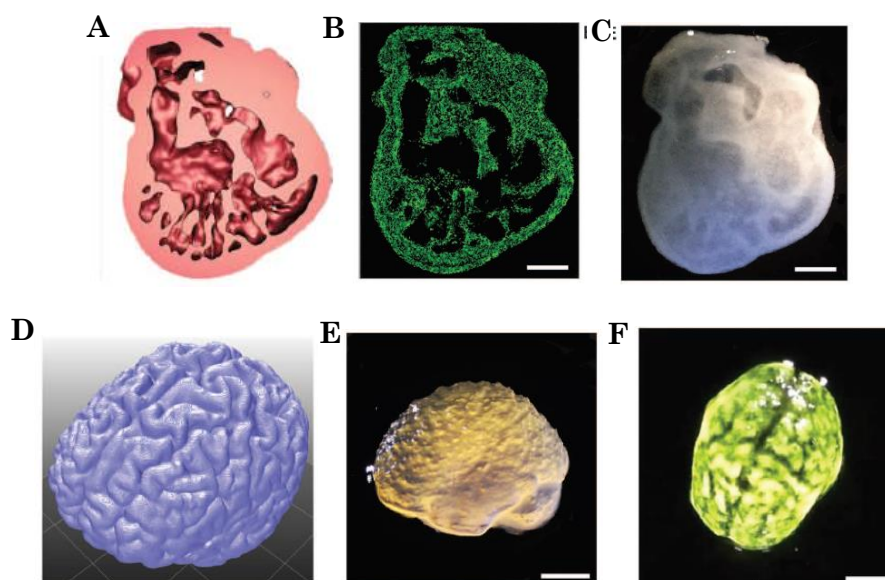


Figure 3.23 FRESH printed scaffolds with complex internal and external architectures based on 3D imaging data from whole organs. A) Cross section of the 3D CAD model of the embryonic heart. B) Cross section of the 3D printed heart in fluorescent alginate (green). C) A dark-field image of the 3D printed heart with internal structure visible through the translucent heart wall. D) A 3D rendering of a human brain from MRI data. E) Lateral view of the brain 3D printed in alginate (cortex and cerebellum). F) Top down view of the 3D printed brain with black dye dripped on top to help visualize the white matter folds printed in high fidelity. Scale bar 1cm [49].

In this context, 3D printing can be an optimal approach for the realization of the pulmonary acinus model using collagen type I hydrogel with and without the FRESH

slurry support bath. The BioX Cellink, printer available at the Polito BIO Med Laboratory of the Polytechnic of Turin is suitable for this type of processing as it offers high resolution and precise printing parameters set up.

### 3.5.2 Molding

To date, the most common biofabrication method is molding, in which a liquid material is poured into a plastic or metal mold and allowed to cure or crosslink. Once the material has solidified, the mold can be removed to release the scaffold. However, it can be difficult to fabricate intricate geometries or very small (<1 mm) features via traditional molding techniques. The complexity and resolution are limited by (1) the resolution of the mold itself (3D printing can be used to generate high-resolution molds) and (2) the ability to remove the scaffold from the mold without destroying the desired structures (appeal to sacrificial materials to preserve delicate features during mold removal, such as gelatin) [61].

Aiming to mimic the strength and flexibility of the trachea, Park et al. [62] designed a bellows style graft through the molding method. So, they 3D printed the sacrificial mold, then injected with PCL/gelatin (desired biomaterial), crosslinked and finally, dissolved the outer mold (Figure 3.24). The sacrificial mold was a negative structure of the designed structure and made of alkali-soluble photopolymer (ASP), which dissolves in NaOH (0.5 N).

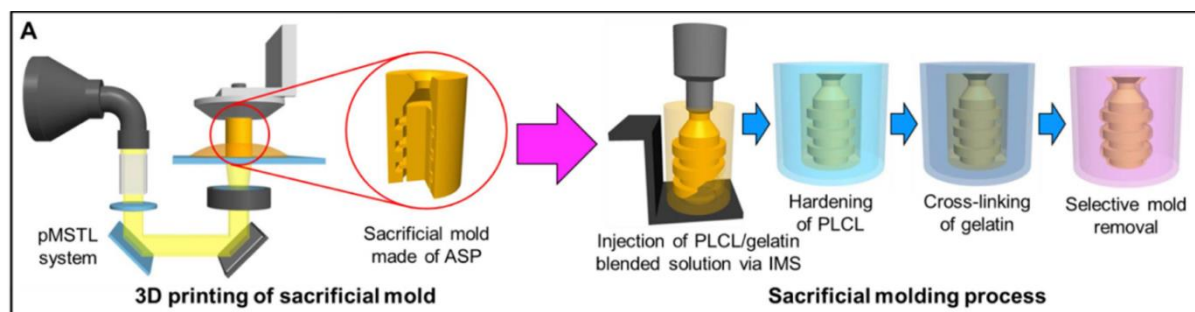


Figure 3.24 Schematic illustration for the development procedure of the tissue-engineered trachea. (A) Preparation of PLCL/gelatin bellows scaffold by indirect 3D printing including 3D printing of sacrificial mold using pMSTL system and sacrificial molding process [62].

While this approach uses traditional plastic printing to create a mold, a mold design could be printed with traditional 3D printing. Then, the whole protocol can be emulated using the collagen hydrogel to be casted inside the mold, crosslinked at 37°C, then sacrificed the mold immersing it in NaOH, and finally, the remaining collagen scaffold washed with distilled water.

To facilitate the casting process, the model needs to be partitioned in two, part A and B are depicted in Figure 3.25. Then both negatives, of part A and B, will be printed.

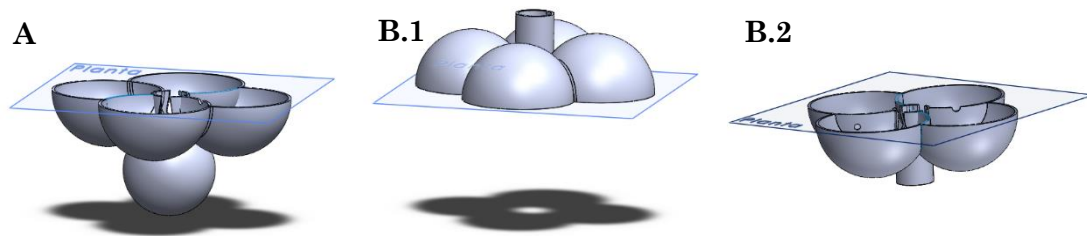


Figure 3.25 3D CAD model of the pulmonary acinus. In the molding technique will be necessary to divide the model in two parts A and B. B.2 is equal to B.1 overturned.

## 4. Results

### 4.1 Characterization of the collagen hydrogel

#### 4.1.1 *Tube inverting test*

The non-flowing gel formed as time went on of the Coll 2 hydrogel aqueous solution, process that started after 10 minutes (10') of incubation and remained stable throughout the 20 minutes period-test. Otherwise, this phenomenon was not visible in less concentrated solutions of collagen hydrogels (Coll 1 and Coll 0.5). Therefore, these demonstrated that the collagen concentration played a critical role in the gelation behavior and after 15 minutes a Coll 2 solution undergoes complete gelation.

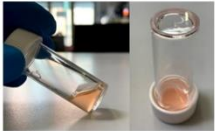
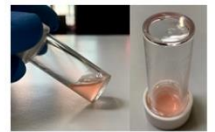
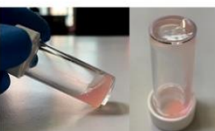
TUBE INVERTING TEST					
	0'	5'	10'	15'	20'
0,5 %					
1%					
2%					

Table 15. Sol-gel phase transition of the hydrogel tested by the tube-inverting method at three different concentrations: 0,5 – 1 – 2 wt % collagen type I.

### 4.1.2 *GLIM optical microscopy*

To understand the fibrillogenesis phenomenon induced by the temperature, GLIM optical microscopic images of the neutralized Coll 2 solution were carried out to study the morphology during the gelation.

An initial solid structure was observed in the photograph of the collagen aqueous solution taken after placing the polymer solution on the sample holder at 37°C (Figure 4.1, image A time 00:00). As time went on, a gel gradually formed; consequently, the GLIM optical microscopic image showed a homogenization of the gel morphology, with the vanishing of the initial structure among the gel by the time of ending the imaging (Figure 4.1, image J time 00:18).

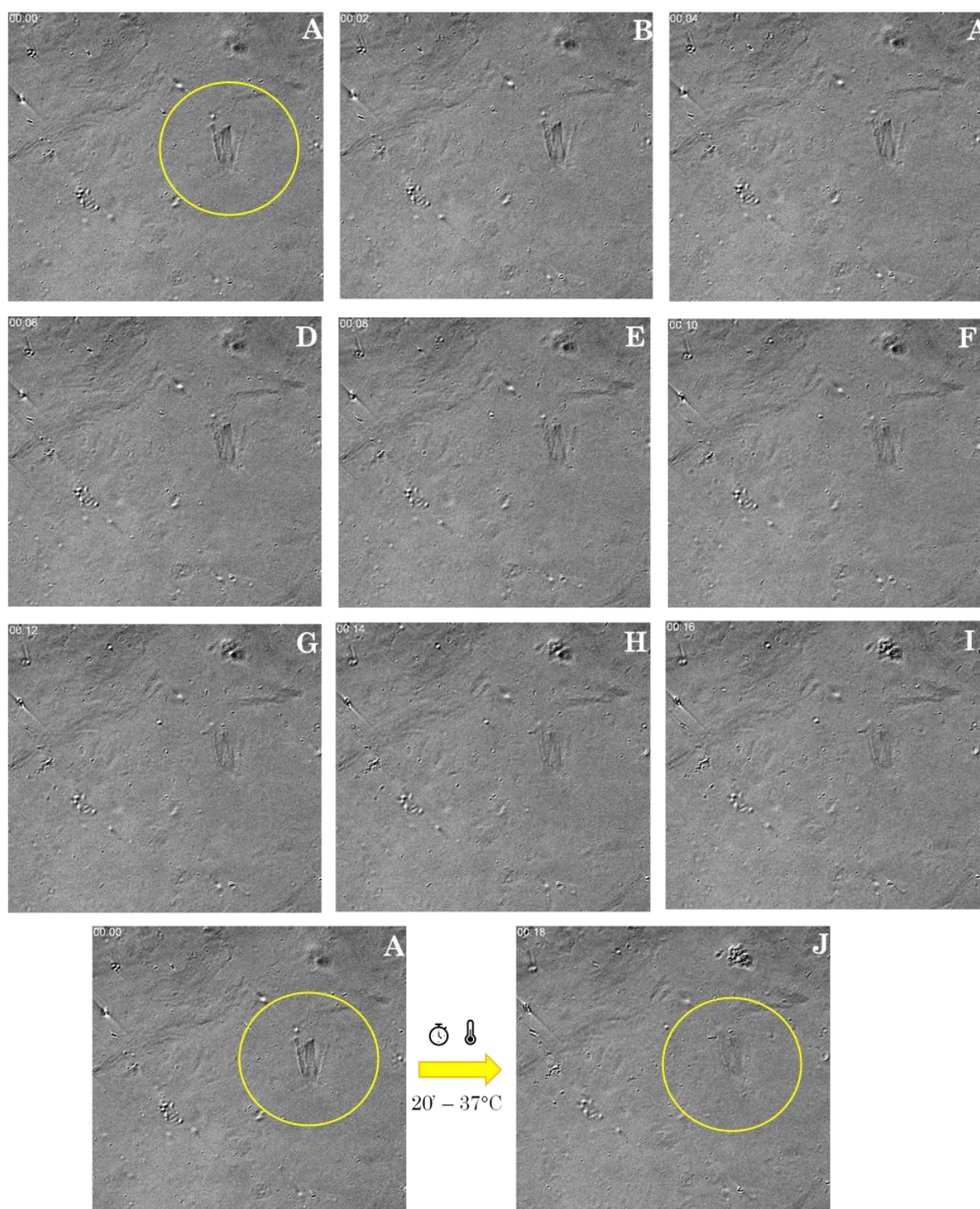


Figure 4.1 GLIM optical microscopic images images of the collagen hydrogels formed by direct heating at 37 °C for 20 minutes. Ten images, from 00:00 (A) to 00:18 (J) minutes with a time-lapse of 2'.

### 4.1.3 FE-SEM

Figures 4.2 and 4.3 show FE-SEM images of a lyophilized Coll 2 sample at different magnification. The images reveal many collagen fibrils that are intertwined with one another with various diameters and directions, confirming a randomly disposed fiber arrangement inherent to collagen among secondary grainy structures, probably associated with NaOH salt debris.

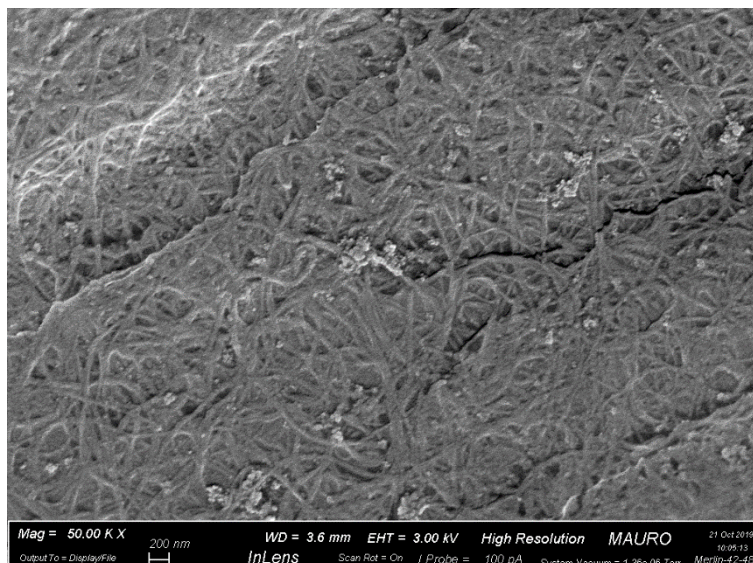


Figure 4.2 SEM analysis of Coll 2 sample. Magnification 50.000.

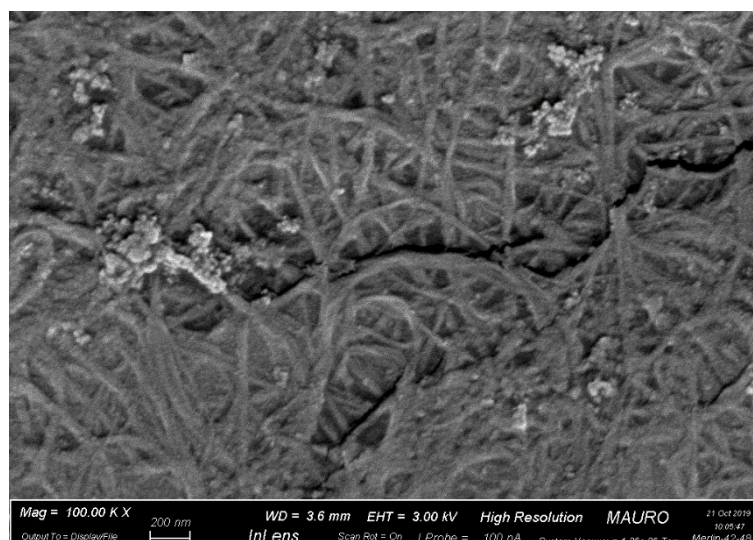


Figure 4.3 SEM analysis of Coll 2 sample. Magnification 100.000.

## 4.2 Scaffold printing

### 4.2.1 Rokit INVIVO

#### 4.2.1.1 Freeform fabrication strategy

Several samples (10x10x5 mm<sup>3</sup>) were printed by using Coll 2 hydrogel solution. The printing temperature was maintained in 4°C (temperature referred to the bioink dispenser), to avoid the collagen gelation. Meanwhile, the temperature of the printing bed was set to 37°C.

Regarding the printing parameters, some of them remained constant based on a previous work [59], while the slicer settings that were varied were: print speed of 4-6 mm s<sup>-1</sup> and the input flow 120-160%.

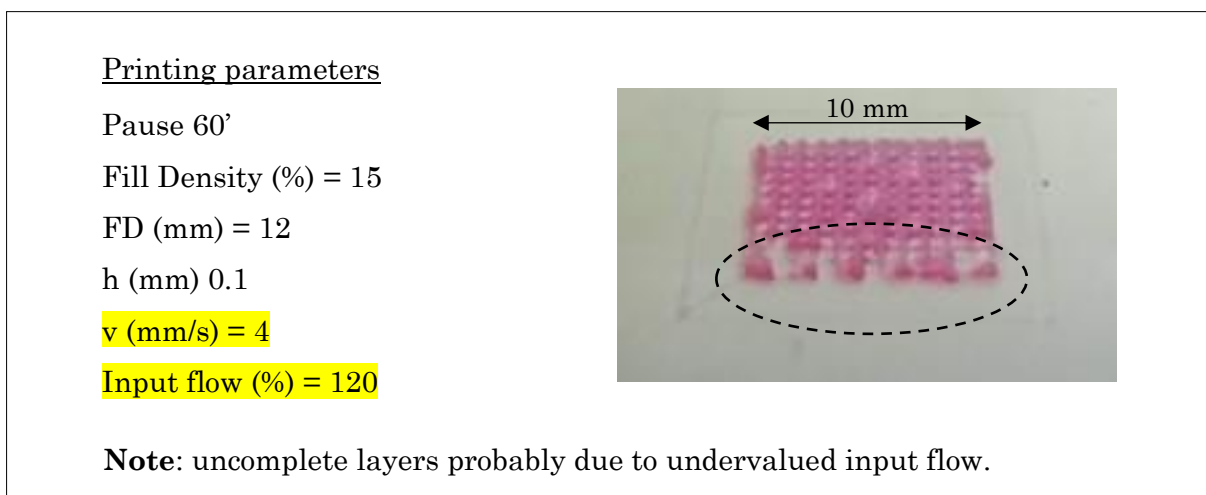


Figure 4.2 ROKIT Invivo, freeform printing strategy, 1<sup>st</sup> trial

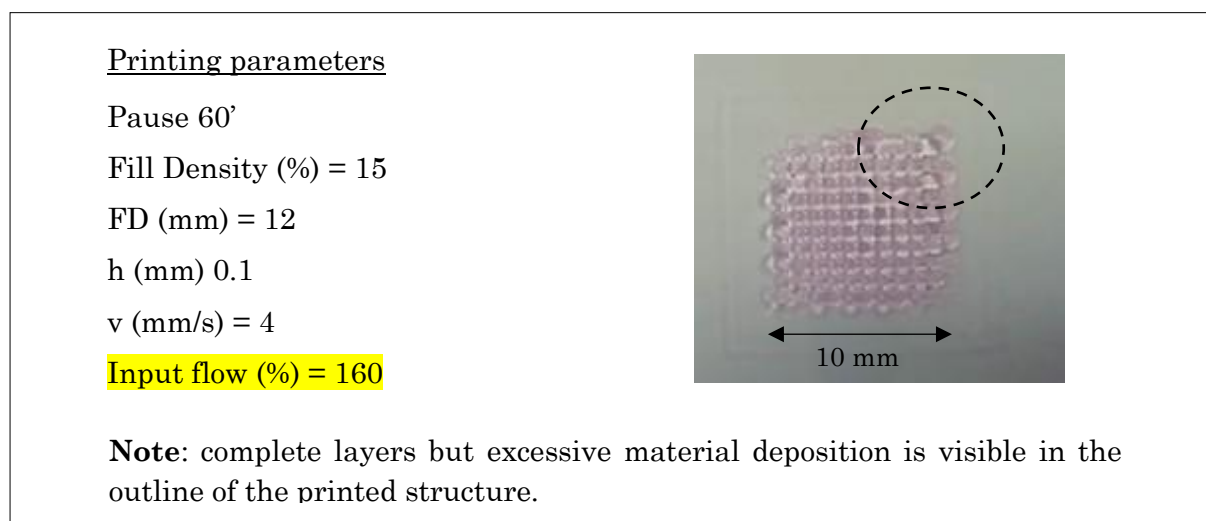


Figure 4.3 ROKIT Invivo, freeform printing strategy, 2<sup>nd</sup> trial

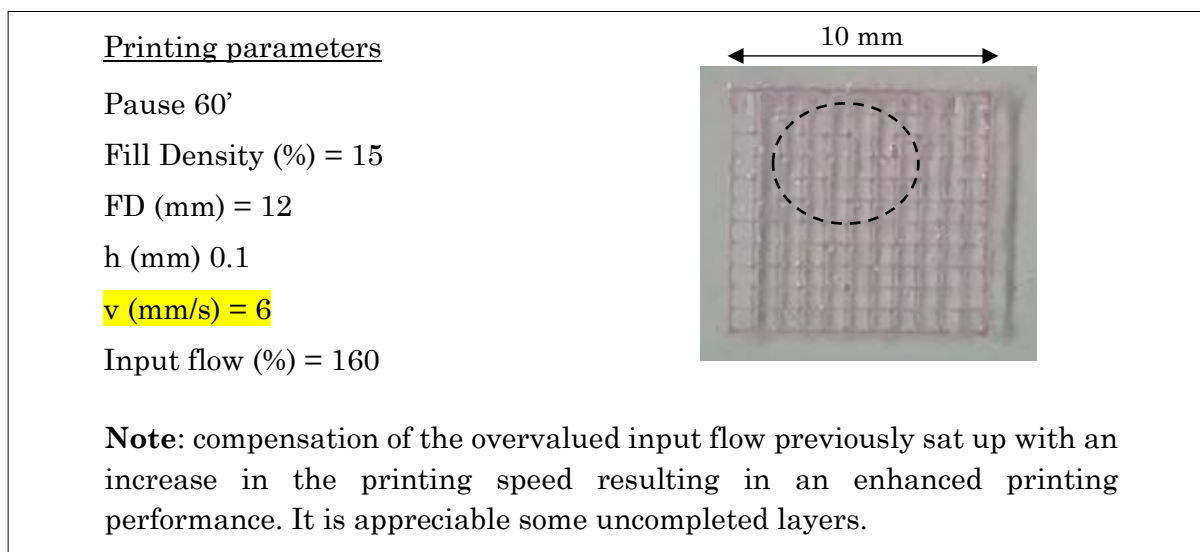


Figure 4.4 ROKIT Invivo, freeform printing strategy, 3<sup>rd</sup> trial

Since there are multiple parameter settings that can be tailored to evaluate their influence in the printing performance, in this instance, the focus was placed on the study of the incidence of the printing speed and the input flow in the scaffold realization. This allowed to evaluate how the two mentioned parameters contribute simultaneously to the result, finding that it is possible to rise the input flow, since Coll 2 is a considerably viscous solution, and compensate the overload of material extruded with a higher printing velocity, resulting in superior printing performance (Figure 4.4). However, further trials must be performed in order to optimize the freeform fabrication strategy to overcome the main problem of the technique: the limitation in high of the printed structures (Figure 4.5).



Figure 4.5 ROKIT Invivo, freeform printing strategy, scaffolds limited thickness.

#### 4.2.1.2 Deposition within a support bath

3D cubic samples (10x10x5 mm<sup>3</sup>) were printed by using Coll 2 hydrogel solution. The bioink dispenser temperature was maintained in 4°C, whereas the temperature of the printing bed was lowered to 22°C, temperature that preserves the slurry rheological properties.

Concerning the printing parameters, all of them remained constant based on the 3<sup>rd</sup> trial with the freeform printing strategy, except for the Fill Density that was raised to 30% (FD=30% instead of 15%).

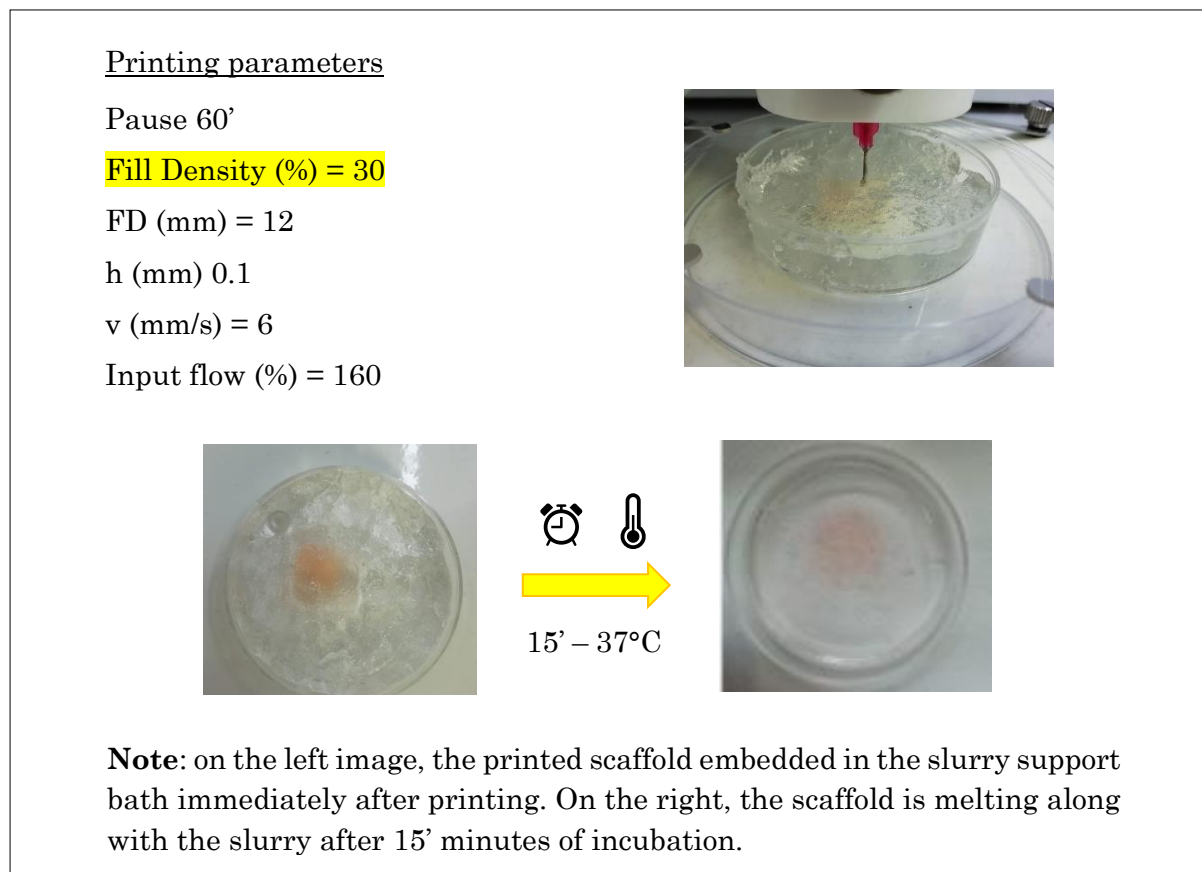


Figure 4.6 ROKIT Invivo, deposition within a support bath.

Even if this technique probably allowed to obtain a robust construct in terms of thickness, it is an assumption made on the basis of the bright pink color of the final printed sample, since as a restriction of the technique, is not possible to clearly evaluate the printability of the construct as it is embedded in the transparent but grainy slurry that hinders the evaluation. Furthermore, after 15 minutes incubation at 37°C, time/temperature that allow the collagen crosslinking and the slurry to melt, both collagen and support bath dissolved losing the scaffold configuration.

### 4.2.2 *BioX Cellink*

3D cubic samples (10x10x5 mm<sup>3</sup>) were printed with CELLINK® START bioink. A polyethylene oxide-based ink used both for evaluation of construct geometry and for education and training purpose. Initially, a collapse structured was printed. After decreasing the print speed from 5 mm/s to 3 mm/s, a second construct was obtained with better structural properties.

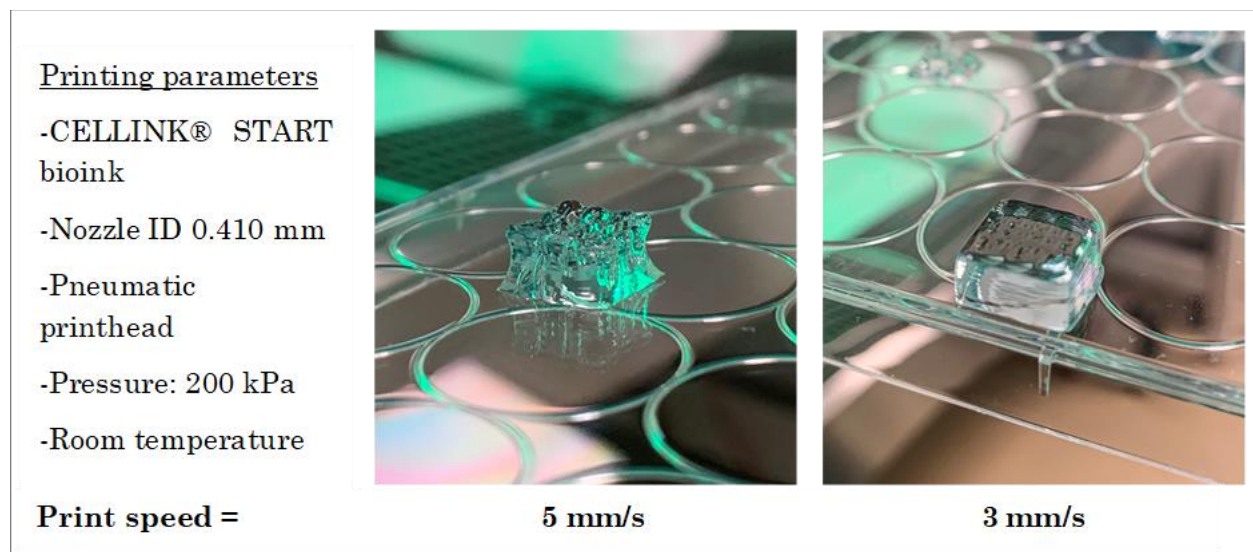


Figure 4.7 BioX Cellink printing parameters.

## 5. Conclusion

Respiratory diseases are leading causes of death and disability in the world. Effective treatments are urgently needed in order to reduce the suffering from lung disease and its high mortality. Preclinical drug development studies are costly and time-consuming and rely on animal testing because existing cell culture models fail to recapitulate complex, organ-level disease processes in humans.

In this context, tissue engineering purpose is the reconstruction of tissue equivalents by the use of a cell source in combination with a biomimetic matrix to support and guide tissue development. Recent advances in nanofabrication techniques have led to 3D tissue constructs capable of mimicking complex tissue physiology and modeling disease pathology being promising technologies for drug screening and reliably predict drug safety and efficacy in humans in preclinical studies.

However, bioengineered 3D models require specific extracellular components or biological materials as scaffold constituent that are often not compatible with the matrix fabrication techniques of high-throughput systems for drug discovery or toxicity testing.

In this project, collagen type I was used as main constituent of the scaffold as it better mimics the stromal component of the alveolar septum. In addition to its exceptional biocompatibility, the collagen-based hydrogel employed is thermosensitive and makes it adequate for the fabrication technique implemented: 3D printing.

The hydrogel characterization demonstrated that the collagen concentration played a critical role in the gelation behavior of the collagen solution. The neutralized (pH= 7,14) 2% wt collagen solution (Coll 2) undergoes complete gelation after 15 minutes of sample incubation at physiological temperature (37°C). The sol-gel transition was assessed by qualitative tests: tube inverting test and FE-SEM images. The images confirmed the fiber network arrangement inherent to collagen. Regarding the GLIM images of the Coll 2 solution, is not possible to define consistent statements from the results due to the lack of analogous studies in the field. Future studies must be performed.

Regarding to the scaffold fabrication technique, 3D printing proved high performance when working with a viscous hydrogel solution. Among the printing methods performed, the freeform fabrication strategy resulted in an easiest bioprinting setup as well as real-time monitoring of the printing process, while the slurry support bath entailed a big limitation in the observation of the printing process because of the turbidity of the gelatin slurry. Between the two printer technologies exploited, the BioX Cellink demonstrate highest performance in terms of velocity, printability and user-friendly setup. However, the printing performance of the BioX Cellink was proved with an industrial ink. Due to Covid-19 pandemic and consequent lab lockdown, practical activity was abruptly interrupted. Hence, future work should concern the implementation of Coll 2 hydrogel ink for the BioX Cellink to print a 3D scaffold along with the optimization of the printing parameters according to the bioink properties.

Regarding the three-dimensional model of the pulmonary acinus depicted in section 3.5, it would be interesting to print a scaled-up version in the BioX Cellink with the parameters previously optimized for a Coll 2 bioink.

## 6. Future work

### 6.1 BioX Cellink: Collagen bioink.

Forthcoming work will concern the implementation of a neutralized collagen-based solution as the ink for the BioX Cellink for printing 3D scaffolds with the aim of optimizing the printing parameters according to the ink properties. By doing so, we will be able to confirm the superior benefits of using the BioX Cellink for printing a 3D collagen-based scaffold and hopefully, overcome the difficulty of obtaining a robust 3D construct. A more complex structure that better mimics the alveoli unit will give raise to the study of cell-scaffold interaction that will implicate cells embedded in the collagen solution ink, what is known as bioink.

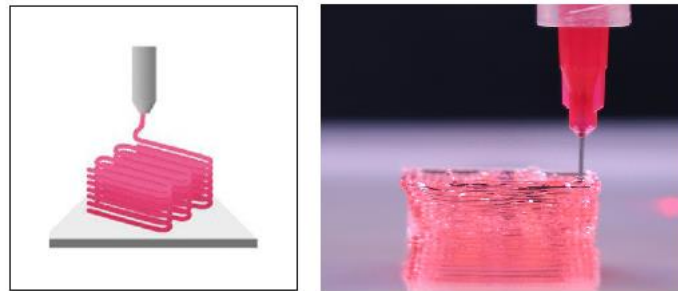


Figure 6.1 Illustrative image of a collagen based scaffold.

Subsequently, the three-dimensional model of the pulmonary acinus (Section 3.5) will be printed with and without the FRESH slurry support bath, ultimately establishing the optimum printing protocol.

## 6.2 Neutralization protocol: NaOH final concentration.

From the FE-SEM images of a lyophilized collagen gel sample (Figure 6.2), two main structures can be identified. On one hand, a homogeneous fibrous network background associated with collagen fibers, and some residual particles most likely associated with NaOH salt debris due to the neutralization process of the collagen solution protocol.

For the neutralization protocol, the collagen solution was supplemented with sodium hydroxide in a concentration of 1M, thus a high volume of buffer was needed to raise the pH collagen solution to  $\sim 7.14$ , usually doubling the initial volume of the solution and consequently, altering the final collagen concentration of the solution.

It is within this framework that future work will consist on rising the buffer concentration to 5M and 10M to assess the effect of the buffer concentration, hypothesizing that less buffer volume will be necessary for the neutralization process thus reducing the presence of salt debris and limiting the variation of the solution final collagen concentration.

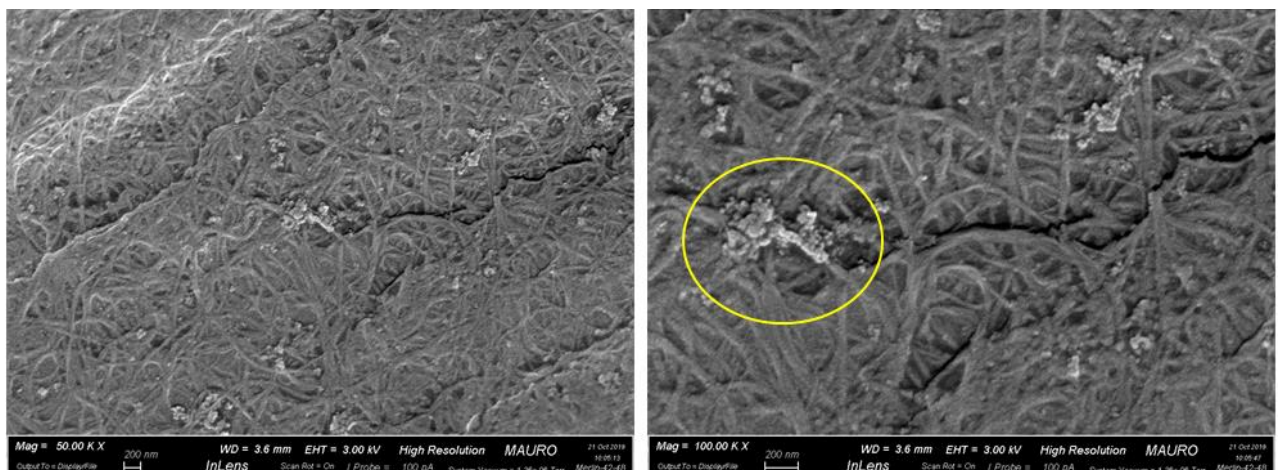


Figure 6.2 SEM images of a lyophilized collagen sample (pH 7.14 and gelled after 30' incubation). NaOH salt debris (yellow circle).

### 6.3 Alternative printing approach: the effect of riboflavin photocrosslinking.

Intending to improve collagen printability we understand that the development of a new collagen bioink formulation is necessary. Studies on collagen hydrogels have shown that gel mechanics can be improved through the addition of blue light-activated riboflavin crosslinking [46]. Riboflavin is a biocompatible vitamin B2 that showed minimal cytotoxicity compared to conventionally utilized photo-initiators, such as glutaraldehyde and formaldehyde. In riboflavin, the crosslinking results from the covalent bond formation between amino acid of collagen fibril induced by singlet oxygen generated from light-excited riboflavin [63].

Diamantides et. al [46] performed a riboflavin crosslinking study and results showed that riboflavin crosslinking increased the storage moduli of collagen bioinks, but the degree of improvement was less pronounced at higher collagen concentrations. Furthermore, dots printed with collagen bioinks with riboflavin crosslinking exhibited smaller dot footprint areas then related to an improvement in collagen printability.

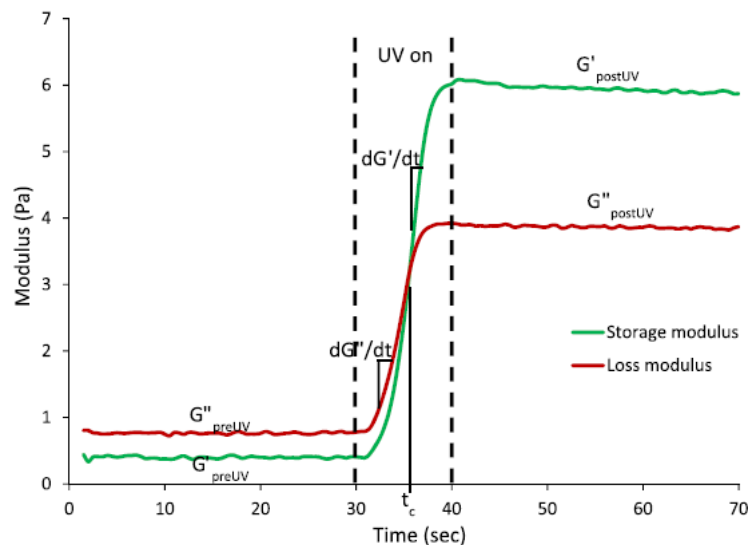


Figure 6.3 Representative results of rheological testing of collagen bioink with riboflavin. Three phases were observed: an initial plateau phase corresponding to the 30s before UV exposure, a growth phase corresponding to the 10 s during UV exposure, and a final plateau phase corresponding to the 30 s after UV exposure. Samples without riboflavin did not experience a growth phase due to UV exposure and the moduli remained constant for the entire test length [46].

In the protocol for collagen hydrogel preparation they used type I collagen extracted from rat tail tendons and 2.0mM riboflavin in 1xPBS was added to the working solution to obtain a final riboflavin concentration of 0.5mM and final collagen concentration of 4, 8, or 12 mg ml<sup>-1</sup>.

Rheological testing showed that after exposure to UV light, samples containing riboflavin experienced a large increase in  $G'$  (Figure 6.2).

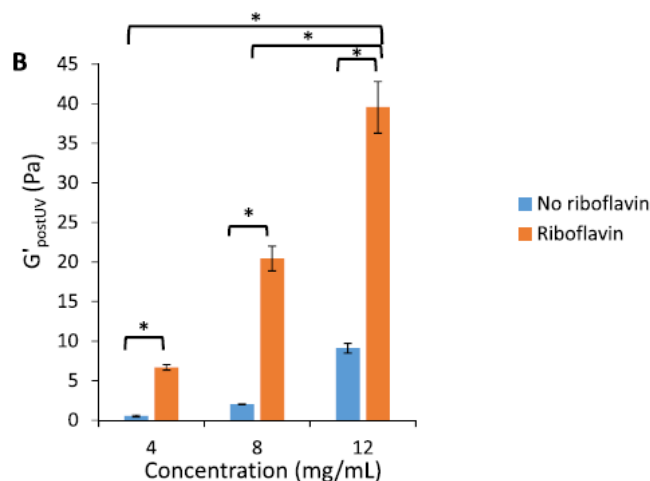


Figure 6.4 Rheological properties of collagen bioinks after 10 s of UV light exposure with and without riboflavin [46].

In another study, Ibusuki et. al [66] used riboflavin as photo-initiator for collagen gel cross-linking using a 458-nm-light wavelength. Short-term viability results showed that 0.25- or 0.5-mM concentrations of riboflavin, and 40 s of illumination permitted more than 90% cell viability. Long-term chondrocyte viability was  $113.1 \pm 11.6\%$  and  $25.4 \pm 2.7\%$ , respectively, at day 7. They proved the feasibility of photochemically cross-link collagen gels using riboflavin and visible light, resulting in stable gel scaffolds with minimal damage to encapsulated cells.

Figure 6.4 let us estimate the range of collagen concentration that must be implemented for a lung application. Mead et al. [64] calculated and estimated the average Young's modulus of a single alveolar wall to be about 5 kPa developing a model of lung parenchyma with a realistic geometry such as a hexagonal network. Sicard et. al [65] applied atomic force microscopy microindentation to characterize human lung tissue. The elastic modulus value represents the mean determined from 39 parenchyma areas taken from across 13 healthy human lung samples and the parenchymal tissue Young's modulus estimated to be  $1.87 \pm 0.95$  kPa. So, according to the Young's modulus of the alveolar wall estimated in previous works and the results showed in Figure 6.4, future works must be performed using a collagen concentration under 4 wt%. Then, the riboflavin concentration must be optimized. Initially, following the protocol of Diamantides et. al and along with rheological testing to set up a final riboflavin concentration and a final collagen concentration that results in a hydrogel with mechanical properties that better mimics lung parenchyma features.

## 6.4 Study of the fibrillogenesis of collagen-riboflavin hydrogels: Thioflavin spectroscopic properties

Thioflavin T is a cationic benzothiazole dye that exhibits enhanced fluorescence upon binding to amyloid fibrils. The specificity of thioflavin T accompanied by the characteristic changes in its spectroscopic properties, gives rise to the wide use of ThT for biochemical studies of the formation of amyloid fibrils *in vitro* [66]. Morimoto et. al [67] founded that the collagen fibril formation could be monitored with Th-T fluorescence.

For this purpose, we suggest that future analysis of the effect of riboflavin in collagen fibrillogenesis can be performed by absorbance measurements of ThT+Riboflavin+Collagen hydrogel, accompanied with GLIM optical images.

ThT absorption spectrum has the shortest (412 nm) and the longest (450 nm) wavelengths in water and water being incorporated into the amyloid fibrils, respectively. The difference absorption spectrum (which is a result of the subtraction of the spectrum of ThT measured in aqueous solution from the dye spectrum measured in the presence of amyloid fibrils) revealed that the fibril bound ThT molecule are characterized by the maximal absorption at 450 nm, Figure 6.5 [66].

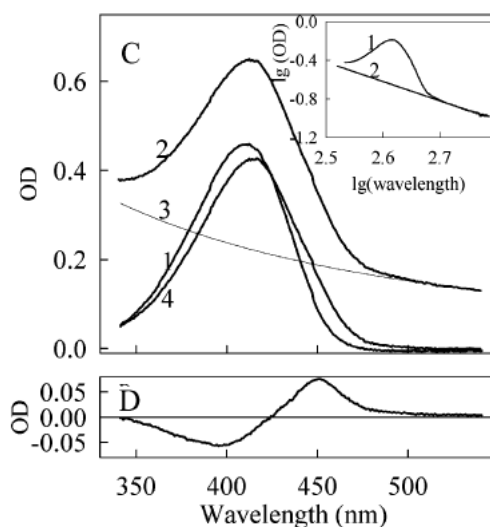


Figure 6.5 Effect of environment on ThT absorption spectra. C) Absorption spectra of ThT solution in water (curve 1) and in water in the presence of amyloid fibrils (curve 2). Curve 3 represents the apparent optical density determined by the light scattering, whereas curve 4 corresponds to the ThT absorption spectrum in the presence of the amyloid fibrils corrected for the light scattering. D) Differential spectrum between the ThT absorption in water (curve 1 in C) and in water in the presence of fibrils (curve 4 in C). The measurements were done for 20  $\mu\text{M}$  ThT in the absence or presence of 0.01 mg/mL amyloid fibrils [66].

## 6.5 Thioflavin-T: groundwork

### 6.5.1 *Materials and methods*

In aqueous solutions, thioflavin T was found to exist as micelles at concentrations commonly used to monitor fibrils by fluorescence assay, ranging from ~10 to 200  $\mu\text{M}$ . Different solutions of Th-T diluted in PBS, starting from 30  $\mu\text{M}$  to 200  $\mu\text{M}$ , were pipetted into a microplate (Figure 6.6). Then, the calibration curve was established using a plate reader (Polito BIO Med Laboratory, Politecnico di Torino).

#### **Thioflavin T**

Thioflavin T is used in the staining of tissue to show primary and secondary amyloid deposits. It was purchased from Sigma – Aldrich.

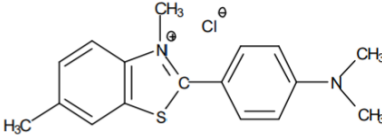
	<b>Supplier</b>	Sigma – Aldrich
	<b>Product name</b>	Thioflavin T
	<b>Form</b>	A yellow to orange-brown powder
	<b>Solubility</b>	Up to 100 mg/mL in H <sub>2</sub> O

Table 16. Thioflavin T product description [68].

#### **Plate reader**

A microplate reader is a laboratory instrument that is used to measure chemical, biological or physical reactions, properties, and analytes within the well of a microplate. A microplate reader detects light signals produced by samples which have been pipetted into a microplate. The optical properties of these samples are the result of a biological, chemical, biochemical, or physical reaction. Absorbance, fluorescence intensity, and luminescence are the most popular and most frequently used detection modes [69].

Particularly, absorbance measures how much light is lost (absorbed) when transmitted through a sample. Molecules often absorb light at a specific wavelength and can be quantified by measuring their absorbance. The principle of absorbance is used to quantify analytes in solution.



Figure 6.6 Microplate reader.

### Protocol for ThT working solutions.

1. Dilution of the ThT powder in PBS (pH 7.4) for a 1 mg/ml stock concentration solution. This stock solution should be stored in the dark and at 4°C.
2. Dilution of the stock solution into the phosphate buffer on the day of analysis to generate the working solutions (30, 50, 80, 100, 130, 150, 180, 200  $\mu$ M).
3. Pipet the working samples into a microplate using a pattern. We suggest the pattern showed in Figure 6.7.

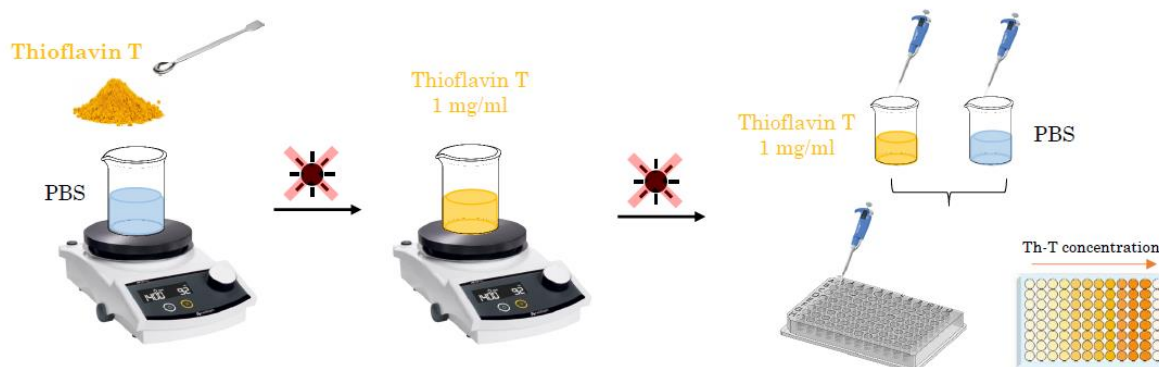


Figure 6.7 Protocol for ThT stock solution (1 mg/ml) and working solutions.

### Considerations:

It is important to work protecting the ThT solutions from light exposure, covering the containers with aluminum foil or working with non-transparent containers, to avoid dye photodegradation.

For the working solutions, the dilution was performed inside an Eppendorf. After pipetting the precise volumes of ThT stock solution and PBS inside the Eppendorf, an up and down motion was repeated several times with the micropipette, until the two solutions look well mixed. If it is correctly performed, this procedure lets avoid the addition of bubbles to the sample. Finally, the samples were pipetted into the microplate.

### 6.5.1 Results

Figure 6.8 represents the ThT absorption spectra measured in PBS solutions. The ThT absorption spectrum reveals that the ThT molecule is characterized by the maximal absorption at 410 nm, results that are congruent with previous reports [66].

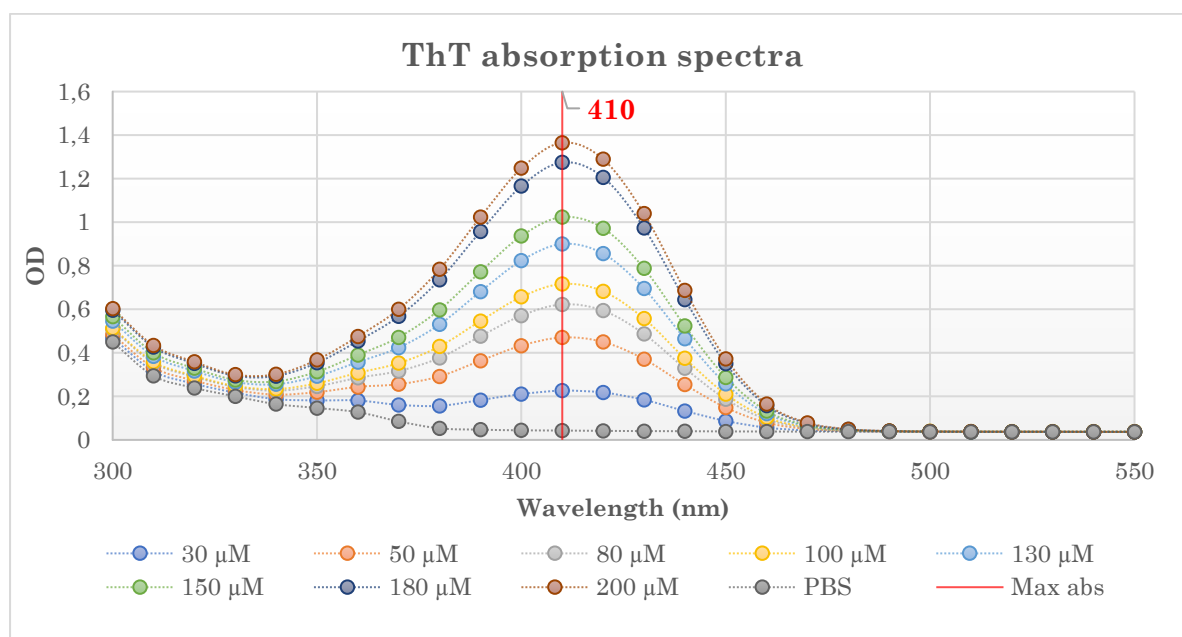


Figure 6.8 Th-T absorption spectra in PBS. Maximal absorption at 410 nm.

In this context, future work will be performed to analyze the effect of riboflavin in collagen fibrillogenesis by absorbance measurements of ThT+Riboflavin+Collagen hydrogels. Starting with ThT-Collagen hydrogels, pre- and post-incubation and studying the difference absorption spectrum caused by fibrils bounding ThT molecules after collagen incubation. Then, the next stage will concern the study of the effect of riboflavin in fibril formation working with ThT+Riboflavin+Collagen hydrogels, pre- and post-UV irradiation. Absorbance measurements will be performed, once again, to observe the difference in the absorption spectrum and finally be able to establish a correlation between riboflavin and fibril formation in a collagen solution.

# Acknowledgments

I would like to thank Prof. Gianluca Ciardelli and Dr. Chiara Tonda Turo who gave me the opportunity to introduce myself in a completely new experience and new environment, giving me the possibility to work in two different laboratories within an amazing team.

My gratitude is dedicated to Michela Licciardello for her great patience, her extremely dedication to work and her precious guidance during my learning process.

I would like to thank to all the student lab's group, that aid me and create a pleasant atmosphere to work.

I want to express my deepest gratitude to my parents because nothing of this would be possible without their unconditional support and love, constantly encouraging me to fulfill my dreams. Thanks to my big brother for his mentoring and friendship, but especially to be a person that I can always trust. I am grateful for my family.

An immense thank to my Italian friends who have become my second family in Turin, in particular I thank Alessandra, Antonio, Alessandro, Victoria and Massimo.

Last but not least, I'm truly grateful to my boyfriend Hernan for his love and support during all these years, and for inspiring me to be the best version of myself.

# List of Abbreviations

2D	Two-Dimensional
3D	Three-Dimensional
ALI	Air-liquid interface
ASCs	Adult stem cells
AS	Acid solubilization
ASP	Alkali-soluble photopolymer
ATII	Alveolar cells type II
BAT	Bovine Achilles tendon
BSE	Bovine Spongiform Encephalopathy
CAD	Computer-aided design
CT	Computed Tomography
cPLA 2	Cytosolic phospholipase A2
DIC	Differential interference contrast
DMEM	Dulbecco's Modified Eagle Medium
DNA	Deoxyribonucleic acid
ECM	Extra-Cellular Matrix
ESCs	Embryonic stem cells
FDA	Food and drug administration
FDM	Fused deposition modeling
G'	Storage modulus
G''	Loss modulus
GLIM	Gradient light interference microscopy

hASCs Human adipose stem cells  
IPF Idiopathic pulmonary fibrosis  
ID/  $\theta_i$  Inner diameter  
LAB Laser assisted bioprinting  
LVE Linear viscoelastic  
MG63 Osteoblast-like cells  
MRI Magnetic resonance imaging  
NSCLC Non-small cell lung cancer  
 $\theta_o$  Outer diameter  
PA Polyacrylamide  
PBS Phosphate buffered saline  
PDMS Polydimethylsiloxane  
PEG Poly-ethylene-glycol  
PLA Polylactide  
PGA Polyglycolide  
PCLT Precision cut lung tissue  
PnP Pneumatic pressure  
PS Pepsin solubilization  
RP Rapid prototyping  
RTT Rat tail tendon  
SEM Scanning Electron Microscopy  
SFF Solid freeform fabrication  
SLM Spatial light modulator  
SLS selective laser sintering  
TCP Tissue culture plastic  
ThT Thioflavin T  
TSE Transmissible Spongiform Encephalopathies

# Bibliography

- [1] J. E. Nichols and J. Cortiella, "Engineering of a complex organ: Progress toward development of a tissue-engineered lung," *Proc. Am. Thorac. Soc.*, vol. 5, no. 6, pp. 723–730, 2008.
- [2] W. Blackwell, *Fundamentals of Anatomy and Physiology For nursing and Healthcare Students*, vol. 53, no. 9. 2016.
- [3] S. Paxton, M. Peckham, A. Knibbs, S. Paxton, A. Knibbs, and M. Peckham, "The Leeds Histology Guide." 2003.
- [4] E. Roan and C. M. Waters, "What do we know about mechanical strain in lung alveoli?," *Am. J. Physiol. - Lung Cell. Mol. Physiol.*, vol. 301, no. 5, pp. 625–635, 2011.
- [5] J. F. Tomashefski, P. T. Cagle, C. F. Farver, and A. E. Fraire, "Anatomy and Histology of the Lung," *Dail Hammar's Pulm. Pathol.*, vol. 1, no. June 2009, 2008.
- [6] "Current Applications of Tissue Engineering in Biomedicine," *J. Biochips Tissue Chips*, vol. s2, 2015.
- [7] C. M. Murphy, F. J. O'Brien, D. G. Little, and A. Schindeler, "Cell-scaffold interactions in the bone tissue engineering triad," *European Cells and Materials*, vol. 26. AO Research Institute Davos, pp. 120–132, 20-Sep-2013.
- [8] L. Moroni, J. Schrooten, R. Truckenmüller, J. Rouwkema, J. Sohier, and C. A. Van Blitterswijk, *Tissue Engineering: An Introduction*, Second Edi. Elsevier Inc., 2014.
- [9] J. Lee, M. J. Cuddihy, and N. A. Kotov, "Three-dimensional cell culture matrices: State of the art," *Tissue Eng. - Part B Rev.*, vol. 14, no. 1, pp. 61–86, 2008.
- [10] A. Moeller, K. Ask, D. Warburton, J. Gauldie, and M. Kolb, "The bleomycin animal model: A useful tool to investigate treatment options for idiopathic pulmonary fibrosis?," *International Journal of Biochemistry and Cell Biology*, vol. 40, no. 3. Pergamon, pp. 362–382, 01-Jan-2008.
- [11] D. Thotala, J. M. Craft, D. J. Ferraro, R. P. Kotipatruni, and S. R. Bhave, "Cytosolic PhospholipaseA2 Inhibition with PLA-695 Radiosensitizes Tumors in Lung Cancer Animal Models," *PLoS One*, vol. 8, no. 7, p. 69688, 2013.
- [12] A. J. Engler, S. Sen, H. L. Sweeney, and D. E. Discher, "Matrix Elasticity Directs Stem Cell Lineage Specification," *Cell*, 2006.
- [13] D. K. Mishra, J. H. Sakamoto, M. J. Thrall, B. N. Baird, and S. H. Blackmon, "Human Lung Cancer Cells Grown in an Ex Vivo 3D Lung Model Produce Matrix Metalloproteinases Not Produced in 2D Culture," *PLoS One*, vol. 7, no. 9, p. 45308, 2012.
- [14] K. Hattar *et al.*, "Interactions between neutrophils and non-small cell lung cancer cells: enhancement of tumor proliferation and inflammatory mediator synthesis," *Cancer Immunol Immunother*, vol. 3, pp. 1297–1306, 2014.

- [15] Z. Tahergorabi and M. Khazaei, "A Review on Angiogenesis and Its Assays."
- [16] N. T. Elliott and F. Yuan, "A review of three-dimensional in vitro tissue models for drug discovery and transport studies," *Journal of Pharmaceutical Sciences*, vol. 100, no. 1. John Wiley and Sons Inc., pp. 59–74, 2011.
- [17] A. V. Rutter, T. W. E. Chippendale, Y. Yang, P. Španěl, D. Smith, and J. Sulé-Suso, "Quantification by SIFT-MS of acetaldehyde released by lung cells in a 3D model," *Analyst*, vol. 138, no. 1, pp. 91–95, Nov. 2013.
- [18] M. Lehmann, L. Buhl, D. Wagner, J. Behr, M. Lindner, and M. Königshoff, "LATE-BREAKING ABSTRACT: Anti-fibrotic effects of nintedanib and pirfenidone in 2D versus 3D lung cultures," in *European Respiratory Journal*, 2016, vol. 48, no. suppl 60, p. OA478.
- [19] J. E. Nichols, J. A. Niles, S. P. Vega, and J. Cortiella, "Novel in vitro respiratory models to study lung development, physiology, pathology and toxicology," *Stem Cell Res. Ther.*, vol. 4, no. SUPPL.1, pp. 4–8, 2013.
- [20] D. C. Wilkinson *et al.*, "Development of a Three-Dimensional Bioengineering Technology to Generate Lung Tissue for Personalized Disease Modeling," *Stem Cells Transl. Med.*, vol. 6, no. 2, pp. 622–633, Feb. 2017.
- [21] W.-H. Xu *et al.*, "Doxorubicin-mediated radiosensitivity in multicellular spheroids from a lung cancer cell line is enhanced by composite micelle encapsulation," *Int. J. Nanomedicine*, vol. 7, pp. 2661–2671, 2012.
- [22] D. Huh, B. D. Matthews, A. Mammoto, M. Montoya-Zavala, H. Yuan Hsin, and D. E. Ingber, "Reconstituting organ-level lung functions on a chip," *Science (80- )*, vol. 328, no. 5986, pp. 1662–1668, 2010.
- [23] K. L. Sellgren, E. J. Butala, B. P. Gilmour, S. H. Randell, and S. Grego, "A biomimetic multicellular model of the airways using primary human cells," *Lab Chip*, vol. 14, no. 17, pp. 3349–3358, Sep. 2014.
- [24] S. Bhatia, "Natural polymer drug delivery systems: Nanoparticles, plants, and algae," *Nat. Polym. Drug Deliv. Syst. Nanoparticles, Plants, Algae*, pp. 1–225, 2016.
- [25] V. M. Weaver *et al.*, "Reversion of the malignant phenotype of human breast cells in three-dimensional culture and in vivo by integrin blocking antibodies," *J. Cell Biol.*, vol. 137, no. 1, pp. 231–245, Apr. 1997.
- [26] "Nano-fibrous scaffolding architecture selectively enhances protein adsorption contributing to cell attachment. - PubMed - NCBI." [Online]. Available: <https://www.ncbi.nlm.nih.gov/pubmed/14566795>. [Accessed: 18-Mar-2020].
- [27] "Effect of scaffold design on bone morphology in vitro. - PubMed - NCBI." [Online]. Available: <https://www.ncbi.nlm.nih.gov/pubmed/17518678>. [Accessed: 18-Mar-2020].
- [28] V. Keriquel *et al.*, "In situ printing of mesenchymal stromal cells, by laser-assisted bioprinting, for in vivo bone regeneration applications," *Sci. Rep.*, vol. 7, no. 1, pp. 1–10, Dec. 2017.
- [29] "3D fiber-deposited scaffolds for tissue engineering: influence of pores geometry and architecture on dynamic mechanical properties. - PubMed - NCBI." [Online].

Available: <https://www.ncbi.nlm.nih.gov/pubmed/16055183>. [Accessed: 18-Mar-2020].

- [30] V. Chiono, “Corso di Ingegneria per la medicina rigenerativa.” Politecnico di Torino.
- [31] T. J. Hinton *et al.*, “Three-dimensional printing of complex biological structures by freeform reversible embedding of suspended hydrogels,” *Sci. Adv.*, vol. 1, no. 9, 2015.
- [32] F. Pati, J. Jang, J. W. Lee, and D. W. Cho, *Extrusion bioprinting*, no. November 2017. 2015.
- [33] J. Zhu and L. J. Kaufman, “Collagen i self-assembly: Revealing the developing structures that generate turbidity,” *Biophys. J.*, vol. 106, no. 8, pp. 1822–1831, 2014.
- [34] B. D. Walters and J. P. Stegemann, “Strategies for directing the structure and function of three-dimensional collagen biomaterials across length scales,” *Acta Biomaterialia*, vol. 10, no. 4. Elsevier BV, pp. 1488–1501, 2014.
- [35] Y. Li, A. Asadi, M. R. Monroe, and E. P. Douglas, “pH effects on collagen fibrillogenesis in vitro: Electrostatic interactions and phosphate binding,” *Mater. Sci. Eng. C*, vol. 29, no. 5, pp. 1643–1649, 2009.
- [36] A. VEIS, “Collagen Fibrillogenesis. Connective Tissue Research, 10(1), 11–24 | 10.3109/03008208209034402.” [Online]. Available: <https://scihub.se/https://doi.org/10.3109/03008208209034402>. [Accessed: 07-Nov-2019].
- [37] K. S. Silvipriya, K. Krishna Kumar, A. R. Bhat, B. Dinesh Kumar, A. John, and P. Lakshmanan, “Collagen: Animal sources and biomedical application,” *J. Appl. Pharm. Sci.*, vol. 5, no. 3, pp. 123–127, 2015.
- [38] “Development of 3D printed fibrillar collagen scaffold for tissue engineering | SpringerLink.” [Online]. Available: <https://link-springer-com.ezproxy.biblio.polito.it/article/10.1007/s10544-018-0270-z>. [Accessed: 19-Mar-2020].
- [39] M. G. Yeo and G. H. Kim, “A cell-printing approach for obtaining hASC-laden scaffolds by using a collagen/polyphenol bioink,” *Biofabrication*, vol. 9, no. 2, 2017.
- [40] V. Lee *et al.*, “Design and fabrication of human skin by three-dimensional bioprinting,” *Tissue Eng. - Part C Methods*, vol. 20, no. 6, pp. 473–484, 2014.
- [41] D. I. Zeugolis, R. G. Paul, and G. Attenburrow, “Factors influencing the properties of reconstituted collagen fibers prior to self-assembly: Animal species and collagen extraction method,” *J. Biomed. Mater. Res. - Part A*, vol. 86, no. 4, pp. 892–904, 2008.
- [42] E. C. Chan *et al.*, “Three Dimensional Collagen Scaffold Promotes Intrinsic Vascularisation for Tissue Engineering Applications,” *PLoS One*, vol. 11, no. 2, p. e0149799, Feb. 2016.
- [43] K. Wolf *et al.*, “Collagen-based cell migration models in vitro and in vivo,” *Semin. Cell Dev. Biol.*, vol. 20, pp. 931–941, 2009.
- [44] Y. B. Kim, H. Lee, and G. H. Kim, “Strategy to Achieve Highly

- Porous/Biocompatible Macroscale Cell Blocks, Using a Collagen/Genipin-bioink and an Optimal 3D Printing Process,” *ACS Appl. Mater. Interfaces*, vol. 8, no. 47, pp. 32230–32240, 2016.
- [45] E. O. Osidak *et al.*, “Viscoll collagen solution as a novel bioink for direct 3D bioprinting,” *J. Mater. Sci. Mater. Med.*, vol. 30, no. 3, 2019.
- [46] N. Diamantides *et al.*, “Correlating rheological properties and printability of collagen bioinks: The effects of riboflavin photocrosslinking and pH,” *Biofabrication*, vol. 9, no. 3, 2017.
- [47] S. A. Ghodbane and M. G. Dunn, “Physical and mechanical properties of cross-linked type I collagen scaffolds derived from bovine, porcine, and ovine tendons,” *J. Biomed. Mater. Res. - Part A*, vol. 104, no. 11, pp. 2685–2692, 2016.
- [48] “3ders.” .
- [49] “Bovine Collagen Type I Powder – Blafar.” [Online]. Available: <http://blafar.com/product/bovine-collagen-type-i-powder/>. [Accessed: 06-Apr-2020].
- [50] “DMEM - Dulbecco’s Modified Eagle Medium | Thermo Fisher Scientific - IT.” [Online]. Available: <https://www.thermofisher.com/it/en/home/life-science/cell-culture/mammalian-cell-culture/classical-media/dmem.html>. [Accessed: 06-Apr-2020].
- [51] “Acetic acid, ACS reagent, ≥99.7% | CH<sub>3</sub>CO<sub>2</sub>H | Sigma-Aldrich.” [Online]. Available: <https://www.sigmaaldrich.com/catalog/product/sigald/695092?lang=it&region=IT>. [Accessed: 06-Apr-2020].
- [52] “Sodium hydroxide, ACS reagent, ≥97.0%, pellets | NaOH | Sigma-Aldrich.” [Online]. Available: <https://www.sigmaaldrich.com/catalog/product/sigald/221465?lang=it&region=IT>. [Accessed: 07-Apr-2020].
- [53] A. Lee *et al.*, “3D bioprinting of collagen to rebuild components of the human heart,” *Science (80-. )*, vol. 365, no. 6452, pp. 482–487, 2019.
- [54] “Gelatin from porcine skin powder, gel strength ~300 g Bloom, Type A, BioReagent, for electrophoresis, suitable for cell culture | Sigma-Aldrich.” [Online]. Available: <https://www.sigmaaldrich.com/catalog/product/SIGMA/G1890?lang=it&region=IT>. [Accessed: 06-Apr-2020].
- [55] “CaCl<sub>2</sub> - Calcium chloride | Sigma-Aldrich.” [Online]. Available: <https://www.sigmaaldrich.com/catalog/product/aldrich/449709?lang=it&region=IT>. [Accessed: 07-Apr-2020].
- [56] “HEPES buffer solution 1 M in H<sub>2</sub>O | 4-(2-Hydroxyethyl)piperazine-1-ethanesulfonic acid | Sigma-Aldrich.” [Online]. Available: [https://www.sigmaaldrich.com/catalog/product/sigma/83264?lang=it&region=IT&c\\_m\\_sp=Insite\\_-\\_prodRecCold\\_xviews\\_-\\_prodRecCold10-4](https://www.sigmaaldrich.com/catalog/product/sigma/83264?lang=it&region=IT&c_m_sp=Insite_-_prodRecCold_xviews_-_prodRecCold10-4). [Accessed: 07-Apr-2020].
- [57] T. H. Nguyen, M. E. Kandel, M. Rubessa, M. B. Wheeler, and G. Popescu, “Gradient light interference microscopy for 3D imaging of unlabeled specimens,” *Nat. Commun.*, vol. 8, no. 1, Dec. 2017.

- [58] “Microscopes – General Microbiology.” [Online]. Available: <https://open.oregonstate.edu/generalmicrobiology/chapter/microscopes/>. [Accessed: 10-Apr-2020].
- [59] F. Ingegneria, “Tesi di Laurea Magistrale Idrogel di collagene biomimetici per la stampa 3D di modelli in vitro del tessuto polmonare,” 2019.
- [60] “BIO X User manual.”
- [61] E. M. Comber, R. N. Palchesko, W. H. NG, X. Ren, and K. E. Cook, “De novo lung biofabrication: clinical need, construction methods, and design strategy,” *Transl. Res.*, vol. 211, pp. 1–18, 2019.
- [62] J. H. Park *et al.*, “A novel tissue-engineered trachea with a mechanical behavior similar to native trachea,” *Biomaterials*, vol. 62, pp. 106–115, 2015.
- [63] J. Heo, R. H. Koh, W. Shim, H. D. Kim, H. G. Yim, and N. S. Hwang, “Riboflavin-induced photo-crosslinking of collagen hydrogel and its application in meniscus tissue engineering,” *Drug Deliv. Transl. Res.*, vol. 6, no. 2, pp. 148–158, 2016.
- [64] B. Suki, D. Stamenović, and R. Hubmayr, “Lung parenchymal mechanics,” *Compr. Physiol.*, vol. 1, no. 3, pp. 1317–1351, 2011.
- [65] D. Sicard, A. J. Haak, K. M. Choi, A. R. Craig, L. E. Fredenburgh, and D. J. Tschumperlin, “Aging and anatomical variations in lung tissue stiffness,” *Am. J. Physiol. - Lung Cell. Mol. Physiol.*, vol. 314, no. 6, pp. L946–L955, 2018.
- [66] A. A. Maskevich *et al.*, “Spectral properties of thioflavin T in solvents with different dielectric properties and in a fibril-incorporated form,” *J. Proteome Res.*, vol. 6, no. 4, pp. 1392–1401, 2007.
- [67] K. Morimoto, K. Kawabata, S. Kunii, K. Hamano, T. Saito, and B. Tonomura, “Characterization of type I collagen fibril formation using thioflavin T fluorescent dye,” *J. Biochem.*, vol. 145, no. 5, pp. 677–684, 2009.
- [68] “THIOFLAVIN T Sigma Prod. No. T3516 Store at room temperature.”
- [69] “Microplate Reader | Plate Reader - BMG LABTECH.” [Online]. Available: <https://www.bmglabtech.com/microplate-reader/>. [Accessed: 20-Apr-2020].